Graphene and functionalised graphene for flexible and optoelectric applications

Submitted by Thomas Hardisty Bointon to the University of Exeter as a thesis for the degree of Doctor of Philosophy in Engineering.

April 2015.

I certify that all material in this thesis which is not my own work has been identified and that no material has previously submitted and approved for the award of a degree by this or any other university.

Thomas Hardisty Bointon

April 2015

Graphene and functionalised graphene for flexible and optoelectric applications

Thomas H. Bointon

CEMPS,

University of Exeter,

Exeter,

UK,

EX4 4QL

June 15, 2015

Abstract

The landscape of consumer electronics has drastically changed over the last decade. Technological advances have led to the development of portable media devices, such as the iPod, smart phones and laptops. This has been achieved primarily through miniaturisation and using materials such as Lithium and Indium Tin Oxide (ITO) to increase energy density in batteries and as transparent electrodes for light emitting displays respectively. However, ten years on there are now new consumer demands, which are dictating the direction of research and new products are under constant development. Graphene is a promising next-generation material that was discovered in 2004. It is composed of a two-dimensional lattice made only from carbon. The atoms are arranged in a two atom basis hexagonal crystal structure which forms a fundamental building block of all sp^2 hybrid forms of carbon. The production of large area graphene has a high cost, due to the long growth times and the high temperatures required. This is relevant as graphene is not viable compared to other transparent conductors which are produced on industrial scales for a fraction of the cost of graphene growth. Furthermore, graphene has a high intrinsic resistivity ($2K\Omega/\square$) which is three orders of magnitude greater than the current industry standard ITO. This limits the size of the electrodes as there is dissipation of energy across the electrode leading to inefficiency. Furthermore a potential drop occurs across the electrode leading to

a non-uniform light emission when the electrode is used in a light emitting display. I investigate alternative methods of large area graphene growth with the aim of reducing the manufacturing costs, while maintaining the quality required for graphene human interface devices. Building on this I develop new fabrication methods for the production of large-area graphene devices which are flexible and transparent and show the first all graphene touch sensor. Focusing on the reducing the high resistivity of graphene using $FeCl_3$ intercalation, while maintaining high optical transmission, I show low resistivity achieved using this process for microscopic graphene flakes, large-area graphene grown on silicon carbide and large-area graphene grown by CVD. Furthermore, I explore the stability of $FeCl_3$ intercalated graphene and a process to transfer a material to arbitrary flexible substrates.

Contents

Abstract **iii**

1 Introduction **1**

2 Theoretical concepts **7**

2.1 Introduction 8

2.2 The structure of graphene and transport properties 8

2.2.1 The effect of changing the Fermi energy 11

2.2.2 Transport in a low magnetic field 13

2.2.3 Transport in high magnetic field 17

2.2.4 Transport for thin film conductors 21

2.3 Methods of large-area graphene production 22

2.3.1 Liquid phase exfoliation 22

2.3.2 Epitaxial graphene grown on SiC 24

2.3.3 Chemical vapour deposition 26

2.4 Functionalising graphene for applications as a transparent electrode material 29

2.4.1 Reduced graphene oxide 30

2.4.2 Graphene combined with silver nanowires 31
2.4.3 Intercalation of graphite and graphene 31
2.5 Raman spectroscopy as a fast tool for assessing the properties of graphene 34
2.5.1 Raman scattering in graphene 35

3 Experimental methodology and fabrication 49
3.1 Introduction 50
3.2 Graphene fabrication 50
3.2.1 Mechanical exfoliation 51
3.2.2 CVD graphene growth on copper 51
3.2.3 CVD graphene transfer 55
3.3 Device fabrication 57
3.4 Intercalation of few layer graphene 59
3.5 Characterisation 59
3.5.1 Optical microscopy 62
3.5.2 Raman spectroscopy 65
3.5.3 Electrical transport 70
3.5.4 Atomic force microscopy 75
3.5.5 Scanning electron microscopy 76

4 Graphene growth in a cold walled furnace 81
4.1 Introduction 82
4.2 Experimental details 87
4.3 Initial stages of the growth of graphene 87
4.3.1 Raman spectroscopy study 87
4.3.2 AFM study of film thickness 94

4.3.3 SEM study of island growth 94
4.4 Growth of continuous graphene film 96
4.5 The electronic quality of graphene films grown by cold wall CVD 99
4.6 Estimation of the cost of graphene production 102
4.7 Conclusion 106

5 All-graphene flexible touch sensor 113
5.1 Introduction 114
5.2 Fabrication process 119
5.3 Device characterisation 122
5.4 Touch sensing 123
5.5 Flexibility measurement 126
5.6 Conclusion 126

6 Functionalising few layer graphene flakes with $FeCl_3$ 133
6.1 Introduction 134
6.2 Fabrication of $FeCl_3$ intercalated few layer graphene flakes 135
6.3 Raman spectroscopy of $FeCl_3$ intercalated few layer graphene 135
6.4 Electrical transport measurements of $FeCl_3$ intercalated few layer graphene 137
6.5 Determining the optical transmission of $FeCl_3$ intercalated few layer graphene 142
6.6 The stability of $FeCl_3$ intercalated graphene 145
6.7 $FeCl_3$ intercalated graphene flakes as a transparent conductor 148
6.8 Conclusion 150

7 Functionalising large area few layer epitaxial graphene for transparent

electrodes **155**

7.1 Introduction 156

7.2 Intercalating few layer epitaxial graphene 156

7.2.1 Raman identification 156

7.2.2 Large area transport measurements of intercalated epitaxial graphene 158

7.3 Characterising the electrical properties of intercalated epitaxial graphene 160

7.4 Magneto-resistance in intercalated graphene 162

7.5 Weak localisation in intercalated graphene 163

7.6 Conclusion 169

8 Functionalising large area few layer graphene grown on nickel substrates for transparent electrodes **173**

8.1 Introduction 174

8.2 Fabrication of $FeCl_3$ intercalated graphene grown on nickel substrates . 175

8.3 Raman spectroscopy 175

8.4 Large area transport measurements 177

8.5 Optical transmission 178

8.6 Intercalated graphene grown on nickel as a transparent conductor . . . 180

8.7 Transfer to of $FeCl_3$ intercalated graphene to arbitrary substrates . . . 180

8.8 Conduction on flexible substrates 181

8.9 Conclusion 182

9 Conclusion **187**

10 Appendix **191**

10.1 Appendix A - Estimating the cost of producing CVD graphene 191

Acknowledgements **195**

List of Publications **197**

List of Figures

2.1 The atomic structure of graphene, where the red and blue atoms represent carbon atoms with a different basis. a_1 and a_2 are unit vectors. . . 9

2.2 The dispersion of monolayer graphene determined using the tight binding model[1]. 10

2.3 a) A schematic showing the parallel plate capacitor model, b) a sketch of the resistivity (ρ_{xx}) plotted against the back gate voltage for monolayer graphene, where the Fermi energy for the hole and electron doped regimes are represented by the filling of the Dirac cones. 11

2.4 A schematic showing the Lorentz force acting on electrons travelling through a conduction channel and being deflected to the sample edges, leading to a Hall voltage 13

2.5 A schematic showing the multiple paths an electron can take around a loop in the system, where each circle represents a scattering site. 14

2.6 A schematic showing the Lorentz force acting on electrons, forming confined orbits in the bulk of the system and edge modes at the edges of the current channel. 17

2.7 A sketch showing the quantisation of the ρ_{xy} (Red) and oscillation of ρ_{xx} (Black) in the quantum Hall regime. The dashed lines represent the classical values of ρ_{xy} and ρ_{xx}. 18

2.8 A sketch showing the density of available states with respect to energy in the quantum Hall regime, where a) represents the ideal case, zero temperature and defects, and b) a realistic case where scattering broadens the energy range for the available states. 20

2.9 The process for producing liquid phase exfoliated graphene solutions. a) Graphite powder is added to water or a solvent such as NMP. There are two shown methods of processing to make the graphite dispersion, b) mechanical agitation where a mechanical blade is used to separate the layers of graphite in the solution or c) ultrasonic exfoliation where the graphite layers are separated using a high powered ultrasonic bath. d) The product is centrifuged to separate the different thicknesses of the graphite flakes in dispersion, where the thicker flakes sink to the bottom and the thinner flakes, including graphene, rise to the top of the solution. e) The solution is filtered to remove any remaining thick flakes leaving a suspension of monolayer and few layer graphene in water or a solvent. 23

2.10 a) The structure of 4H-SiC, where the carbon and silicon atoms and planes are identified, b) the process of graphene growth on SiC, where temperatures range from 1200 to 1600°C under argon gas flow, c) monolayer growth on a Si terminated face and multilayer growth on a C terminated face. 25

2.11 a) The annealing of a copper substrate to prepare the surface for CVD graphene growth at high temperatures of 1035°C, b) the process of the formation of graphene on the copper surface, where CH_4 is adsorped at the copper surface to form carbon species, which can form a nucleation site, attach to an already formed nucleation site or desorb from the surface, c) the final formed film shown on both sides of the copper foil, d) the annealing of a nickel substrate to prepare the surface for CVD graphene growth at high temperatures, e) the CH_4 gas adsorption is catalysed at the surface of the nickel and the resulting carbon species absorbed into the nickel substrate, f) the precipitation of few layer graphene after cooling the substrate to room temperature. 27

2.12 a) A distribution of silver nanowires on a substrate, b) a distribution of liquid phase exfoliated graphene on a substrate, c) the combination of silver nanowires and liquid phase exfoliated graphene on a substrate. . 32

2.13 A sketch showing the photo excitation of an electron and the relaxation via a) Rayleigh scattering, b) Raman Stokes scattering via a phonon to a virtual state and c) Resonant Raman Stokes scattering via a phonon to an allowed state. 34

2.14 The Raman spectra of monolayer graphene measured at 532nm wavelength. The D, G and 2D peaks are highlighted. 36

2.15 a) A schematic showing the phonon and defect scattering responsible for the D peak, b) a schematic showing the second order phonon scattering responsible for the 2D peak. 38

2.16 A schematic showing the phonon scattering responsible for the G peak. 39

2.17 A schematic showing the four possible excitation and relaxation processes responsible for the multipeak 2D band of graphene. 39

2.18 A sketch showing the effect of increasing disorder on the G peak position and I(D)/I(G) adapted from ref.[41] 41

3.1 The process of mechanical exfoliation of graphite: a) graphite placed on adhesive tape, b) repeated peeling to create an array of graphitic flakes, c) a substrate placed on the surface of the adhesive tape, d) and e) examples of photographs showing monolayer and few-layer graphene and bulk graphite on a SiO_2/Si substrate under 564nm illumination (scale bar:25μm). 52

3.2 a) A schematic of the hot walled furnace used for CVD growth on copper; MFC indicated a mass flow controller for controlling the mixture of growth gases b) a schematic of a resistively heated cold walled furnace used for CVD growth on copper, c) a graph demonstrating parameters for growing graphene on copper in a cold walled furnace, d) a diagram showing the interactions of carbon adatoms during the nucleation and growth stages. 53

3.3 a) Copper foil is spin coated with PMMA, b) the graphene on the underside of the copper is etched using an argon plasma, c) the copper is etched in a dilute solution of nitric acid in ultrapure deionised water, d) the film is spoon transferred in ultrapure deionised water, e) the film is lifted from solution using a substrate, f) the film is left to dry prior to removal of the PMMA support. 56

3.4 a) The substrate is spin coated with PMMA, b) the PMMA is exposed with the inverse of the mask pattern using electron beam lithography, c) the PMMA and exposed regions are etched using an Ar/O_2 plasma, d) the PMMA mask is removed to leave the patterned graphene, e) a photograph showing a monolayer graphene flake, f) a photograph showing the PMMA mask before the etching process, g) a photograph showing the PMMA mask after the etching process, h) a photograph showing the finished etched monolayer graphene flake. (scale bar:25 μ m) 58

3.5 a) The substrate is coated with a bilayer of 'soft' 495K and 'hard' 950K PMMA, b) the contact pattern is exposed in the PMMA using electron beam lithography, c) the sample is developed, giving an undercut and then metallised using Cr/Au 10nm/50nm, d) the PMMA and excess metal are removed using acetone, e) an image of an etched graphene flake, f) an image that shows the pattern exposed in the PMMA, g) the remaining contacts after the metallisation and 'liftoff' process.(scale bar:25μm) 60

3.6 a) A schematic of the two zone vapour transport intercalation setup, b) a graph showing the temperature of each zone with respect to time from the beginning of the experiment. (c) and (d) Images showing a multilayer graphene flake at t = 0 and t = 9.6 Hours 61

3.7 a) A schematic showing the different optical conditions for the substrate and sample intensity measurements, b) an image of monolayer graphene where the areas for substrate and sample intensity measurement are highlighted, c) a histogram showing the distribution of contrasts for 50 few layer flakes, where the monolayer graphene is coloured pink, bilayer graphene is yellow and the trilayer graphene is coloured cyan. 63

3.8 a) A diagram showing the measurement of the reference transmission intensity ($I_{reference}$) and the sample transmission intensity ($I_{measured}$), b) an image showing few layer graphene on a glass substrate; the highlighted regions are the areas where the reference transmission intensity and the sample transmission intensity where measured. 64

3.9 a)A Raman spectrum of monolayer graphene showing the G- and 2D-bands, b)a plot of the ratio between the intensities of the G- and 2D-bands with respect to the number of graphene layers. Raman spectra were measured under x100 magnification. 65

3.10 The Raman spectrum in the region of the 2D-band for: a)monolayer graphene with one fitted peak, b)bilayer graphene with four fitted peaks, c)trilayer graphene with six fitted peaks and d)greater than four layer graphene fitted with three bands. 67

3.11 a)Evolution of the G-band with increasing number of layers of graphene; the intensity is normalised to the Si-band intensity for each sample, b)a plot showing the I(G)/I(Si) ratio against the number of layers of graphene. 68

3.12 A representative Raman spectrum of $FeCl_3$ intercalated few layer graphene; a) the upshifted G-band to the G_1- and G_2-band positions; insets: the graphene/$FeCl_3$ structure for the G_1 and G_2-bands, b) the single peak structure of the 2D-bands $FeCl_3$ intercalated few layer graphene. 69

3.13 a)A schematic of a two terminal device, where yellow regions represent gold contacts, grey are graphene regions and red are the interface resistance regions, b) a diagram showing the two equivalent circuits; **Top**: the measured resistance ($R_{measured}$), **Bottom**: the series resistance of the contacts ($R_{contact}$), the interface ($R_{interface}$) and the graphene ($R_{graphene}$). 70

3.14 a) A schematic of the four terminal contact configuration, where R_{xx} is measured using V_1 and V_2 voltage probes and R_{xy} is measured using V_1 and V_3, b) a schematic showing the lines of equivalent voltage potential that occurs across the graphene current channel when a current is driver between the source-drain contacts. 73

3.15 a)The two terminal configuration of the constant current measurement, b)the four terminal configuration of the constant current measurement where voltage probes are on the edge of the current channel. 74

3.16 a)A schematic of a graphene device separated from the backgate electrode with a SiO_2 dielectric; the electric field generated between the two plates is indicated by the charge symbols in the dielectric, b)a diagram of the circuit used to change the backgate voltage. 75

3.17 a)AFM topographic image of carbon film on a SiO_2 substrate; the highlighted region shows the sampled region for the statistical study, b) a histogram showing the distribution of measured heights from within the sampled area. Substrate and film distributions are fitted and the difference between the average heights gives the total thickness 76

3.18 a)An scanning electron micrograph showing graphene islands (Black) on a SiO_2 substrate, b) processed micrograph with inverted intensities and applied black and white threshold, c) a single identified island extracted from the micrograph shown in false colour, d) all identified islands in the micrograph after applying a noise filter. 77

4.1 A waterfall plot showing Raman spectra for films grown at 950°C, transferred to SiO_2/Si with an excitation wavelength of 532nm. Raman spectra are normalised to the intensity of the Si Raman peak at 521cm^{-1} and are presented with ascending time, from 1 to 6 minutes. The peaks are identified from left to right as the D peak, the G peak, the D' peak, and the 2D peak. 89

4.2 Fitted parameters plotted with respect to time for a growth temperature $T_G = 950°C$; each point is representative of a typical carbon film for each time. a) The intensity of the G and 2D peaks (I_G and I_{2D}), b) the peak maximum of the D peak divided by the G peak (I_D/I_G), left, and the estimated domain size from the Tuinstra-Koenig relation, right, c) the position of the G $\widetilde{\nu_G}$ and 2D peaks $\widetilde{\nu_{2D}}$, d) the FWHM of the D, G and 2D peaks, FWHM(D,G,2D). The highlighted regions show the relevant fitted parameters from a continuous graphene film produced using the two stage growth process. The dashed lines are a guide for the eye and the experimental errors are smaller than the data points used on the plot 90

4.3 A waterfall plot showing Raman spectra of graphene transferred to SiO_2/Si, and with an excitation wavelength of 532nm. Raman spectra at 521cm^{-1} are normalised to the intensity of the Si Raman peak and are presented for a growth temperature T_G of a) 1000°C and growth time t_G ranged from 5 to 40 seconds, b) 1035°C and growth time t_G ranged from 1 to 60 seconds. 92

4.4 Illlustration of a carbon film as it converts from a disordered structure into graphene islands at $T_G = 950°C$. The inset, left, shows the AFM topography of a thick carbon film after 1 minute of growth, with the disordered structure highlighted. The inset, right, shows the AFM topography of a graphene island, with the structure highlighted, after 6 minutes. 93

4.5 CVD film thickness plotted against the growth time t_G for transferred films grown at $T_G = 950°C$. The dashed line is a guide for the eye and the experimental error bars are smaller than the data points. 95

4.6 Scanning electron micrographs of transferred films, grown at T_G = 950°C, for growth times t_G of a) 1 minute, b) 3 minutes, c) 4 minutes, d) 5 minutes, e) 6 minutes, and f) 8 minutes. All images are in scale. 97

4.7 The average island size of grown graphene islands, determined from SEM, with respect to growth time t_G for growth temperatures T_G of a) 950°C, b) 1000°C and c) 1035°C. 98

4.8 The average island separation of grown graphene islands, determined from SEM, with respect to growth time t_G for growth temperatures T_G of a) 950°C, b) 1000°C and c) 1035°C. 98

4.9 The four terminal resistivity (ρ_{xx}) plotted against applied backgate voltage and measured at a temperature of 4.2K. The red curve is obtained before the annealing procedure and the black curve is obtained after the annealing procedure. 100

4.10 a) The measured four terminal longitudinal resistivity (ρ_{xx}) plotted with respect to the charge carrier concentration (n) at a temperature of 4.2K. The inset shows the dimensions of the measured device on a false colour image, b) the longitudinal conductivity (σ_{xx}) plotted with respect to the charge carrier concentration (n). The linear gradient (red) shows the region where the charge carrier mobility is estimated. 101

4.11 The Hall conductance (σ_{xy}), normalised to ($4e^2/h$), plotted against the applied gate voltage (V_g) at a temperature of 250mK with a perpendicular magnetic field of 13T. The dashed lines represent the half integer steps corresponding to the relationship $\sigma_{xy} = (n + 1/2) \times 4e^2/h$. 103

4.12 The four terminal longitudinal resistivity (ρ_{xx}) plotted against the applied gate voltage (V_g), measured at a temperature of 250mK with a perpendicular magnetic field of 13T. 104

4.13 A colour map showing the differential Hall conductance at a temperature of 250mK for a range of applied magnetic fields from 5 to 13T and charge carrier concentration (n) ranging from -6×10^{12} to 4.1×10^{12} cm^{-2}. The dashed lines indicate the Landau levels. 105

4.14 A plot comparing the electronic quality factor (Q) to the cost of graphene production, where our work has been included. 107

5.1 a) A schematic of a four wire resistive touch sensor, where 1 and 2 are electrical connections to the bottom resistive layer and 3 and 4 are electrical connections to the top resistive layer. Note: protective polymer layer not shown. b) A side slice across the area where both top and bottom resistors overlap, where insulating spacers are shown to separate the two resistive layers. A stylus is shown in contact with one area to demonstrate the action of pressing the two resistive layers together. . . 115

5.2 a) A schematic of a capacitive touch sensor, where two sets of conducting strips are separated by a dielectric layer, b) a side slice of a region where the top and bottom electrodes intersect, c) a schematic of self capacitance, where an insulating stylus elastically deforms the dielectric layer bringing the two electrodes closer together, d) a schematic of mutual capacitance where a human finger causes stray electric field and hence a parasitic capacitance, e) and f) are equivalent circuits showing the effect of the parasitic capacitance on the measured capacitance. . . 116

5.3 A schematic of the construction of a smart phone screen illustrating the need for the touch sensor to be transparent. 117

5.4 A schematic of the process for fabricating the touch sensor devices. a) Graphene is grown on a copper substrate, b) the foil is coated with PMMA and contacts are exposed using electron beam lithography, c) exposed regions are developed and metallised with 50nm of gold, d) the foil is coated with PMMA and an etch mask is defined between the gold contacts with electron beam lithography, e) exposed graphene is etched using an argon/oxygen plasma, f) the foil is coated with PMMA and the copper is etched using 1 molar $FeCl_3$, g) the film is washed in ultrapure water, and h) the film is transferred to a PEN substrate. 120

5.5 a) Window in PMMA after electron beam exposure and development on copper foil coated in CVD graphene, b) a gold square after the metallisation gold on top of a copper foil coated with CVD graphene, c) gold contacts connected by graphene strips on the surface of the copper foil, d) the gold contacts and graphene strips supported by a PMMA film floating on $FeCl_3$ etchant solution, e) the transferred structure onto a PEN substrate, and f) an example of a finished device where two sets of graphene strips have been orthogonally transferred on the PEN substrate 121

5.6 a) Schematic of a set of gold contacts on a single graphene strip, where L is the length between gold contacts and W is the width of the graphene strip, b) a photograph showing a measurement probe in electrical contact with a gold pad, c) a circuit diagram showing the two terminal measurement of the graphene strip using a Keithly 2400 source meter, and d) the measured two terminal resistance plotted against the number of squares (L/W). The error bars as smaller than the size of the data points. 124

5.7 a) Schematic of a single element of the all-graphene touch sensor, where the dashed red lines indicate the connections to the measurement circuit, and b) the circuit diagram showing a variant of the Wheatstone bridge used for measuring an unknown capacitance C_x of the element; inset: the element connected by red dashed lines. 125

5.8 a) Schematic of all of the elements on the device, the colour plot represents the change in the capacitance when a 36g load is placed on one element and the white arrow indicates the element where the load was applied, b) change in capacitance with respect to time for a human finger repeatedly touching an element, c) change in resistance of the graphene strips after uniaxially bending the sensor around a 2cm bending radius, parallel (black) and perpendicular (red) to bending radius 127

5.9 An example of a touch sensor similar to the device tested. 128

6.1 The Raman spectra of pristine bilayer graphene to five layer graphene, in the region on the G and 2D peaks. 136

6.2 The configuration of the $FeCl_3$ and graphene layers that give rise to a) the G_1 peak, where each graphene layer has one adjacent layer of $FeCl_3$ and b) the G_2 peak, where each graphene layer has two adjacent $FeCl_3$ layers. 136

6.3 The Raman spectra for $FeCl_3$ intercalated graphene ranging from bilayer graphene to 5-layer graphene, with a focus on the $G_{1,2}$ and 2D peaks. . 138

6.4 The measured sheet resistance with respect to sample temperature for pristine bilayer, trilayer, 4-layer and 5-layer graphene. 139

6.5 The measured sheet resistance with respect to temperature for $FeCl_3$ intercalated bilayer, trilayer, 4-layer and 5-layer graphene. 140

6.6 a) The measured Hall resistance plotted against perpendicular applied magnetic field, b) a zoomed plot of the measured Hall resistance for $FeCl_3$ intercalated bilayer graphene. All measurements were performed at 4.2K. 141

6.7 a) The measured charge carrier concentration, of $FeCl_3$ intercalated graphene plotted against the number of graphene layers, b) the estimated charge carrier mobility of $FeCl_3$ intercalated graphene plotted against the number of graphene layers. 142

6.8 The optical transmission of pristine few layer graphene ranging from monolayer graphene to 5 layer graphene. The transmission indicated is for a wavelength of 550nm. 143

6.9 The optical transmission of $FeCl_3$ intercalated few layer graphene, ranging from bilayer graphene to 5 layer graphene. The transmission indicated is for a wavelength of 550nm. 144

6.10 Several Raman spectra taken across the area of an $FeCl_3$ intercalated sample a) just after the intercalation process and b) after 3 month exposure to atmosphere. 145

6.11 The Raman maps showing the G_1 and G_2 peaks before and after heating to 150°C (scale bar : 10μm), b) the sheet resistance measured at room temperature after exposure to heating detailed in c). All sample heating was performed in atmosphere. 146

6.12 The sheet resistance of a $FeCl_3$ intercalated graphene flake measured after exposure to $>$ 95% humidity from 0 to 24 days. The inset shows the measured device. 147

6.13 The Raman spectra of a $FeCl_3$ intercalated sample after exposure to humidity (>95%) for 0 to 25 days. 149

6.14 A plot comparing the 550nm transmission and sheet resistance of ITO to those of a range of carbon based conductors. 151

7.1 The top spectrum shows the pristine trilayer graphene G and 2D peaks, where fitting the 2D peak gives the number of layers of the graphene film. The bottom spectra shows the spectra after the intercalation process including an upshifted G peak to the G_1 and G_2 peak positions and a single peaked 2D peak. 157

7.2 Longitudinal resistance plotted against the aspect ratio of the device, where L is the sample length and W is the width of the current channel (0.7cm). The blue points are for pristine trilayer graphene, the red points are for intercalated trilayer graphene, where the fitted linear gradients represents the large area resistivity. The inset describes the device geometry and measurement circuit. Error bars are smaller than the size of the data points 159

7.3 a) Distribution of the measured large area resisitvities for pristine trilayer graphene, b) distribution of the measured large area resistivities for intercalated trilayer graphene. 160

7.4 The Hall resistance plotted against the applied perpendicular magnetic field, at a temperature of 1K, for $FeCl_3$ intercalated trilayer graphene. The inset shows the device geometry. 161

7.5 The measured temperature dependence with respect to longitudinal resistivity for the $FeCl_3$ intercalated graphene device shown in the inset of Figure 7.4. 161

7.6 The measured longitudinal resistivity at 1K with respect to applied perpendicular magnetic field for $FeCl_3$ intercalated graphene. 163

7.7 The measured longitudinal resistivity with respect to perpendicular magnetic field for a temperature range between 280mK and 80K. The black lines indicate a parabolic fit of the data under the condition $|B| > 250$mT. 164

7.8 A plot of the change in longitudinal conductance due to weak localisation plotted against perpendicular magnetic field from 280mK to 80K. The black lines are the fit of the data to Equation 7.1. 165

7.9 A plot showing the estimated τ_ϕ with respect to temperature for two different samples. 167

7.10 A plot showing the estimated dephasing length (L_ϕ) with respect to temperature for two different samples. For comparison, there are four other studies included which use CVD graphene[13], epitaxial graphene[10, 11] and natural graphene[9]. 168

8.1 a) Raman spectrum for a thin region of graphene before (Top) and after (Bottom) the intercalation process, b) Raman spectrum for a few layer island of graphene before (Top) and after (Bottom) the intercalation process. 176

8.2 a) An illustration of the $FeCl_3$ intercalated graphene islands on a thin film of not intercalated graphene, b) a schematic of the cross section through the film showing the parallel conduction and c) the equivalent circuit diagram of b) where R_G is the resistance of the graphene under layer and R_{FeCl3} is the resistance through the intercalated multilayer graphene. 177

8.3 A graph showing the measured resistance (R) of an $FeCl_3$ intercalated few layer graphene film plotted against the aspect ratio (L/W), where the dashed gradient is representative of the resistivity. The inset shows the measurement circuit. 178

8.4 The optical transmission of the $FeCl_3$ intercalated few layer graphene film from 450 to 850nm. The inset shows the $FeCl_3$ intercalated graphene on glass. 179

8.5 A schematic showing the transfer of $FeCl_3$ intercalated graphene onto arbitrary substrates. a) $FeCl_3$ intercalated graphene on a glass substrate, b) PMMA spun coated on the substrate, c) thermal release tape is applied and the PMMA and $FeCl_3$ intercalated graphene were pealed off the glass substrate, d) the thermal release tape was applied to a PEN substrate, e) the thermal release tape was heated and removed, then the PMMA was removed using acetone and IPA. 181

8.6 a) A photograph showing the series circuit of a 9V battery, an LED, the transferred intercalated film and a resistor, b) the same circuit with the resistor removed. 182

8.7 A photograph showing the film conducting while the substrate is flexed. 183

List of Tables

4.1 Literature data required to make an estimation of the electronic quality factor (Q) for each growth procedure of CVD graphene. The mobility is the field effect mobility ($cm^2/(V.S)$), L is the device length (μm), W is the device width (μm) and the electronic quality factor (Q) ($\mu m^2 \times cm^2/(V.S)$)). The electronic quality factor is rounded to the nearest two significant figures to account for uncertainty in device size. 84

4.2 Energy consumption of each CVD graphene growth procedure, broken down into the heating of the foils and the annealing and growth process. Total cost is rounded to the nearest two significant figures to account for uncertainty in growth times and fluctuating costs. 84

4.3 Gas consumption for several CVD graphene growth studies, for the estimation of the total cost of graphene growth gases. *The cost for methane has been replaced with that of argon, as argon diluted methane was used. The total cost is rounded to the nearest two significant figures to account for uncertainty in gas flow times. 85

4.4 The estimation of cost of each price component and the total cost of the growth for each procedure in GBP (£). The total cost is rounded to the nearest two significant figures. 86

10.1 The estimation for cost of each different growth gas in £per cubic meter (m^3). 192

Chapter 1

Introduction

The landscape of consumer electronics has drastically changed over the last decade. Technological advances have led to the development of portable media devices, such as the iPod, smart phones and laptops. This has been achieved primarily through miniaturisation and use of materials such as Lithium and Indium Tin Oxide (ITO) to increase energy density in batteries and as transparent electrodes for light emitting displays respectively. There is also the development of high-efficiency solar cells, which could enable a viable alternative method of producing energy to fossil fuels. In households, the development of solid-state lighting has also significantly reduced energy consumption with respect to traditional filament light bulbs. Furthermore, there has been the development of printable electronics, which allow for the production of circuits on fabrics. Wearable electronics, such as heart rate monitors and near field communication can be incorporated into clothes to collect and transmit data for use to monitor patients in hospitals and many other purposes ranging from communication to personal security.

However, ten years on there are now new consumer demands, which are dictating the

direction of research and new products are under constant development. For example, flexible and more durable mobile phone screens are required as there is the chronic issue of broken displays due to dropping. The current technology uses ITO on rigid glass as flexing and bending of ITO causes a significant degradation in the conductive properties. The answer to this issue is to explore new materials that do not shatter on impact and have comparable properties to ITO.

Graphene is a promising next-generation material that was discovered in 2004. It is composed of a two-dimensional lattice made only from carbon. The atoms are arranged in a two atom basis hexagonal crystal structure which forms a fundamental building block of all sp^2 hybrid forms of carbon, such as carbon nano tubes, Buckminsterfullerenes and graphite[1].

Graphene has cone-shaped valence and conduction bands that meet at the K points of the Brillouin zone. Graphene is a semi-metal with no bandgap, therefore devices made from graphene cannot be switched off, hence are not suitable for logic applications. However, through chemical functionalisation, by applying strain or constraining the sample dimensions, the properties of graphene can be modified to open a band gap.

Monolayer graphene was first isolated in 2004[2], using micro mechanical exfoliation. The material was attractive due to the simplicity of production, however the process was limited to the production of microscopic graphene flakes. Significant improvements in the methods of production have lead to the generation of large-area (up to 30 inches squared) high-quality graphene[3], which is set to revolutionise the electronics industry, like the first silicon transistor.

Although the thickness of monolayer graphene is only 0.34nm, it is stronger than any other material[4] and an effective oxygen barrier[5], while remaining flexible[6]. By utilising these properties Ti et al. have demonstrated graphene as a protective coating

to materials that are susceptible to oxidation such as iron and copper[7]. Furthermore, graphene is very stable and remains inert over a wide range of temperatures[8] and exposure to many solvents[9]. However, there are observable changes to the electronic transport properties through charge transfer from doping. By measuring the changes in electrical resistivity it has been shown that graphene can be used as a substrate to detect a wide range of dopants and organic molecules[10].

Finally, monolayer graphene has a high optical transmission of 97%[11] while being conductive with a typical resistivity of 2KΩ/□[2]. The combination of all of these remarkable properties has lead to the greatest interest of the scientific community for the use of graphene as a transparent conductor[13, 12]. However, graphene still has some fundamental limitations before it can become a viable transparent conductor.

The production of large area graphene has a high cost, due to the long growth times and the high temperatures required. This is relevant as graphene is not viable compared to other transparent conductors which are produced on industrial scales for a fraction of the cost of graphene growth. Furthermore, graphene has a high intrinsic resistance (2KΩ/□) which is three orders of magnitude greater than the current industry standard ITO. This limits the size of the electrodes as there is dissipation of energy across the electrode leading to inefficiency. Furthermore a potential drop occurs across the electrode leading to a non uniform light emission when the electrode is used in a light emitting display. This alludes to the four main objectives I aim to complete in this thesis in a bid to tackle these fundamental issues:

First, to investigate alternative methods of large area graphene growth with the aim of reducing the manufacturing costs, while maintaining the quality required for graphene human interface devices. Typical chemical vapour deposition (CVD) graphene growth uses hot walled tube furnaces to achieve the high growth temperatures required

($\approx 1000°C$). My aim is to investigate graphene growth in an energy efficient cold walled furnace and take advantage of the rapid heating and cooling times to optimise the growth procedure. This is the primary objective of Chapter 4.

Second, to develop new fabrication methods for the production of large-area graphene devices which are flexible and transparent. Not all processing techniques are compatible with graphene and often lead to the destruction of the graphene film. My aim is to develop a method of fabrication that allows for the construction of an all-graphene touch sensor by reevaluating the current methods used to create flexible touch sensors for portable devices, which is the aim of Chapter 5.

Third, to demonstrate, through functionalisation of graphene that the electrical resistivity can be significantly reduced, while maintaining the high stability and optical transmission of graphene. There are many methods of functionalisation involving the doping of mono and few-layer graphene with charged molecules[14]; however, they are often unstable and degrade with exposure to humidity and temperature[15]. My aim is to functionalise exfoliated few-layer graphene flakes using $FeCl_3$ intercalation and characterise the optical and electrical properties, then to demonstrate the inherent stability of this new material. This is the primary focus for Chapter 6.

Finally, to investigate upscaling the $FeCl_3$ intercalation process of multilayer graphene over a large-area for the development of transparent, flexible and low resistance electrodes. There are several methods of producing large-area few-layer graphene; within the scope of this thesis I focus on the functionalisation of graphene grown by the thermal decomposition of 4H-SiC (Chapter 7) and graphene grown by CVD on a nickel substrate (Chapter 8). Furthermore, I aim to develop a method of producing large-area $FeCl_3$-intercalated graphene on arbitrary substrates.

Bibliography

[1] Geim, A. K. *et al.* The rise of graphene. *Nature Mater.* **6**, 183-191 (2007).

[2] Novoselov, K. S. *et al.* Electric Field Effect in Atomically Thin Carbon Films. *Science* **22**, 666-669 (2004).

[3] Bae, S. *et al.* Roll-to-roll production of 30-inch graphene films for transparent electrodes. *Nature Nanotech.* **5**, 574-578 (2010).

[4] C. Lee, *et al.* Measurement of the Elastic Properties and Intrinsic Strength of Monolayer Graphene. *Science* **321**, 385 (2008).

[5] Yankg, Y. H. *et al.* Graphene: Super Gas Barrier and Selectivity of Graphene Oxide-Polymer Multilayer Thin Films. *Adv. Mater.* **25**, 493 (2013).

[6] Park, H. *et al.* Flexible Graphene Electrode-Based Organic Photovoltaics with Record-High Efficiency. *Nano Lett.* **14**, 5148-5154 (2014).

[7] Ti, L. *et al.* A long-term oxidation barrier for copper nanowires: graphene says yes. *Phys. Chem. Chem. Phys.* **17**, 4231-4236 (2015).

[8] Nan, H. Y. *et al.* The thermal stability of graphene in air investigated by Raman spectroscopy. *J. Raman Spectrosc.* **44**, 1018-1021 (2013).

[9] Taha-Tijerina, J. *et al.* Quantification of the Particle Size and Stability of Graphene Oxide in a Variety of Solvents. *Part. and Part. Sys. Charact.* **32** 334-339 (2014).

[10] Kaverzin, A. A. *et al.* Electrochemical doping of graphene with toluene. *Carbon* **49**, 3829-3834 (2011).

[11] Blake, P. *et al.* Making graphene visible. *Appl. Phys. Lett.* **91**, 063124 (2007).

[12] Wassei, J. K. *et al.* Graphene, a promising transparent conductor. *Mater. Today* **13**, 52-59 (2010).

[13] Elmer, K. Past achievements and future challenges in the development of optically transparent electrodes. *Nat. Photonics* **6**, 809-817 (2012)

[14] Zhan, D. *et al.* FeCl3-Based Few-Layer Graphene Intercalation Compounds: Single Linear Dispersion Electronic Band Structure and Strong Charge Transfer Doping. *Adv. Funct. Mater.* **20**, 3504-2509 (2010).

[15] Wang, X. *et al.* N-Doping of Graphene Through Electrothermal Reactions with Ammonia. *Science* **324**, 5928 (2009).

Chapter 2

Theoretical concepts

2.1 Introduction

Graphene, in the form of monolayer or few-layer material has remarkable properties. The structure gives rise to the unique band dispersion responsible for the exotic electrical transport properties and optical characteristics. Furthermore, there are many methods of producing graphene with advantages and disadvantages for the mass production and application of graphene. In this chapter, I will give an overview of the fundamental properties of graphene; the different methods of mass production required for industrial applications; the range of functionalisation procedures that have been used to modify the properties of graphene as a transparent conductor.

2.2 The structure of graphene and transport properties

The structure of graphene consists of a two atom basis triangular Bravais lattice which forms a honey comb structure, shown in Figure 2.1. The electronic band structure of graphene is different to that of typical two-dimensional electron gases such as gallium arsenide (GaAs) which have a density of states (DOS) independent of the Fermi energy (E_F). Instead, the DOS of graphene increases linearly with energy and has no gap in states between the conduction and the valence band.

The electronic band structure can be estimated using the tight binding model which shows that each unit cell has 6 points where the valence bands and conduction bands meet, as shown in Figure 2.2. This is called the Dirac point or the charge neutrality point (CNP), where there is no population of dominant charge carriers. Furthermore, at these points there is a linear dispersion, meaning that the charge carriers behave

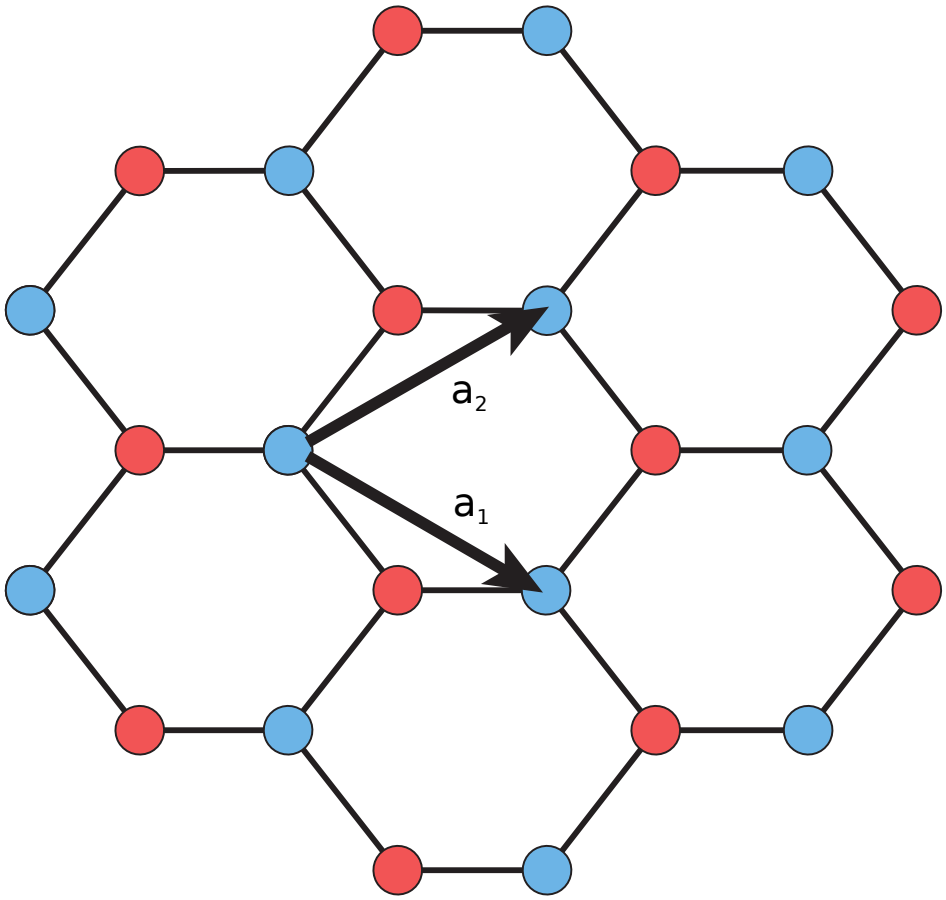

Figure 2.1: The atomic structure of graphene, where the red and blue atoms represent carbon atoms with a different basis. a_1 and a_2 are unit vectors.

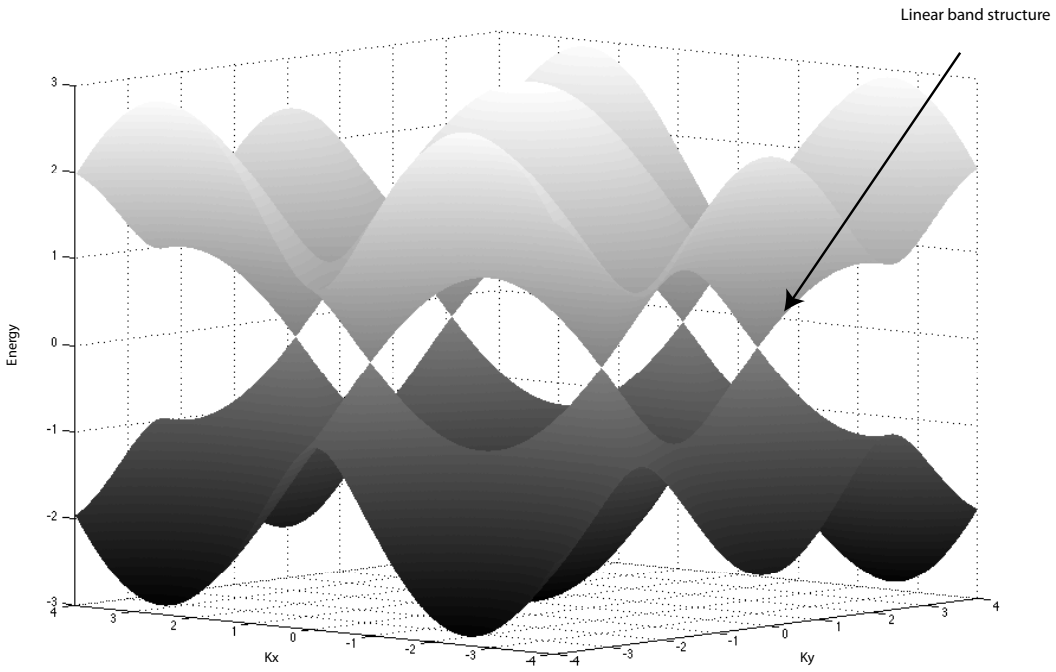

Figure 2.2: The dispersion of monolayer graphene determined using the tight binding model[1].

like massless Dirac fermions[1].

The Fermi energy with respect to the CNP determines the dominant charge carrier; below the CNP the dominant carriers are holes, while above the CNP the dominant carriers are electrons.

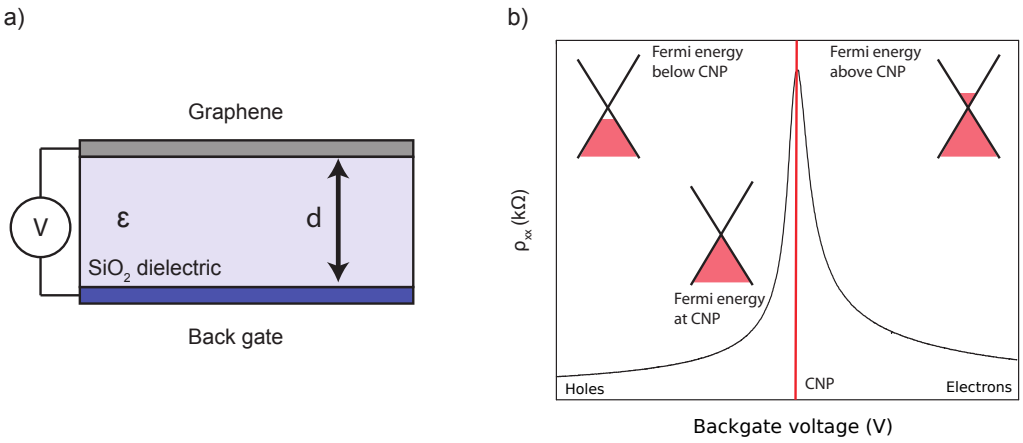

Figure 2.3: a) A schematic showing the parallel plate capacitor model, b) a sketch of the resistivity (ρ_{xx}) plotted against the back gate voltage for monolayer graphene, where the Fermi energy for the hole and electron doped regimes are represented by the filling of the Dirac cones.

2.2.1 The effect of changing the Fermi energy

The Fermi energy is the energy of the highest occupied state relative to the lowest occupied state in the system. This can be modified by doping, temperature and the electric field applied through a top gate or a back gate electrode[2]. Raising the Fermi energy increases the total occupied DOS and therefore increases the charge carrier concentration.

The effect of the electric field on the charge carrier concentration can be modelled using a system with two separated plates held at different potentials, as shown in Figure 2.3a. The two plate system is modelled as a parallel plate capacitor with a separation of d, a dielectric constant of ϵ, a potential difference of V_g and a charge carrier concentration n with units of m^{-2}. The electric field between the two plates is given as:

$$E = \frac{n}{\epsilon} = \frac{V_g}{d} \tag{2.1}$$

Rearranging the equation enables to link the gate voltage V_g to the charge carrier concentration:

$$V_g = \frac{nd}{\epsilon} \tag{2.2}$$

Figure 2.3b shows a sketch of the resistivity plotted against the back gate voltage. At high back gate voltage the resistivity is low, because the Fermi energy is raised to a region where there are many hole or electron charge carriers, whereas with no applied back gate voltage the Fermi energy is held at the Dirac point and there are few available states for conduction, leading to high resistivity.

From measuring the resistivity of a graphene sample with respect to the back gate voltage the charge carrier mobility can be determined. The charge carrier mobility μ is a parameter that is useful to describe the effect of an in plane electric field on the charge carriers. The value of μ is influenced by the rate at which the charge carriers scatter through the material $(1/\tau)$, where τ is the average time between scattering and is given by the following equation, where e is the electronic charge and m is the mass of the charge carriers[3]:

$$\mu = \frac{e\tau}{m} \tag{2.3}$$

The lower the scattering rate the higher the mobility, which is often used as a measure of the quality of the graphene. The conductivity of the film is related to the charge carrier mobility and concentration by the equation[4]:

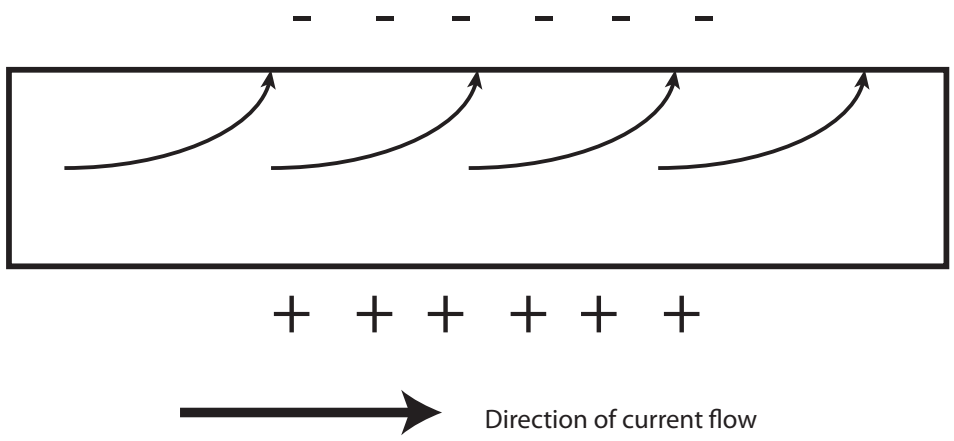

Figure 2.4: A schematic showing the Lorentz force acting on electrons travelling through a conduction channel and being deflected to the sample edges, leading to a Hall voltage

$$\sigma = ne\mu \tag{2.4}$$

By plotting the sample conductivity against the charge carrier concentration, the gradient of the linear regime enables to derive the charge carrier mobility and the effective sample quality can be estimated.

2.2.2 Transport in a low magnetic field

Applying a perpendicular magnetic field to the direction of current flow in a material causes the deflection of the charge carriers through the Lorentz force, known as the Hall effect. This leads to the accumulation of charge at the edge of the current channel, shown in Figure 2.4, and a measurable potential difference between the edges of the sample known as the Hall voltage. From this the Hall resistance is calculated by

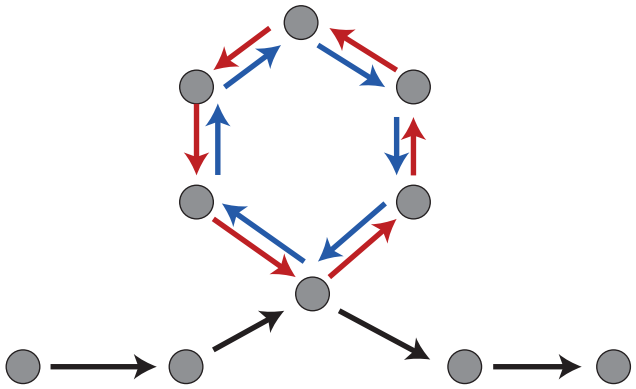

Figure 2.5: A schematic showing the multiple paths an electron can take around a loop in the system, where each circle represents a scattering site.

dividing the Hall voltage by the current through the channel[4]:

$$R_{xy} = \frac{V_{xy}}{I} = -\frac{1}{ne}B \tag{2.5}$$

The Hall resistance depends linearly on the applied perpendicular magnetic field B, and the gradient is dependent on the charge carrier density n and the electronic charge carriers e. By plotting R_{xy} versus B the charge carrier concentration can be estimated.

Furthermore, the charge carrier type affects the sign of the gradient as the Lorentz force is opposite for electrons and holes. This allows for the determination of the type of the dominant charge carrier concentration in the system.

At low temperature, in graphene, in the diffusive regime weak localisation is observed. Weak localisation is a quantum correction to the resistivity of a disordered material that occurs at low temperatures. As electrons scatter through a system they take many different paths from one side of a sample to the other. The random paths

that the electrons can take can be such that the electrons travel in a loop, shown in Figure 2.5. There is also an equal probability that the electron travels in the same loop but in the opposite direction. If the dephasing length is longer than the loop length, the electrons traveling around the loop in opposite directions are phase coherent. As both paths have identical lengths and they are phase coherent, then the electrons interfere and cancel each other making the probability of an electron traveling around the loop zero. This effect is observed when measuring the temperature dependence of the resistivity. At higher temperatures, the dephasing length is shorter than the loop length due to thermal fluctuations; this allows the electrons to travel around the loop without interfering and leaves the sample resistance unaffected. Lowering the temperature increases the dephasing length up to a point when it becomes longer than the loop length and the quantum interference effects reduce the number of available paths that the electrons can propagate through and therefore increase the sample resistivity.

Applying a perpendicular magnetic field to the system modifies the phase of both of the electrons propagating around the loop. This reduces the effect of the localisation and eventually destroys the quantum interference reducing the resistance to the classical value[5].

By measuring the resistivity of a sample at low temperature with respect to a perpendicular magnetic field allows for the estimation of several parameters such as the dephasing length L_ϕ, the intervalley dephasing length L_i and the intravalley dephasing length $L_\star$. To analyse the quantum correction due to the weak localisation in graphene I use the following expression[6]:

$$\Delta\sigma(B) = \frac{e^2}{\pi h}\left[F\left(\frac{B}{B_\phi}\right) - F\left(\frac{B}{B_\phi + 2B_i}\right) - 2F\left(\frac{B}{B_\phi + B_i + B_\star}\right)\right] \tag{2.6}$$

Where $\Delta\sigma$ is the correction to the conductivity due to weak localisation and $B_{\phi,i,\star}$ are fitting parameters related to scattering rates. The function F is given as:

$$F(z) = ln(z) + \psi\left(\frac{1}{2} + \frac{1}{z}\right) \tag{2.7}$$

Where ψ represents the digamma function which is defined as the logarithmic derivative of the gamma function. The elastic, intervalley and intravalley scattering rates $\tau^{-1}_{\phi,i,\star}$ can be estimated from the corresponding fitting parameters $B_{\phi,i,\star}$:

$$B_{\phi,i,\star} = \frac{\hbar}{4De}\tau^{-1}_{\phi,i,\star} \tag{2.8}$$

The diffusion coefficient D is a parameter that describes how easily a charge carrier can classically diffuse through a sample. This parameter is dependent on the sample conductivity σ, the effective charge carrier mass $m\star$, which is the mass of the charge carrier within to graphene due to the bands, and the electronic charge of the carriers e.

$$D = \frac{\sigma\pi\hbar^2}{2m^\star e^2} \tag{2.9}$$

Furthermore, the dephasing length L_ϕ can be estimated:

$$L_\phi = (D\tau_\phi)^{\frac{1}{2}} \tag{2.10}$$

Analysis of the fitted weak localisation peak in low magnetic fields enables to obtain various parameters that can be used to assess the quality of a systems, as described in Section 7.5.

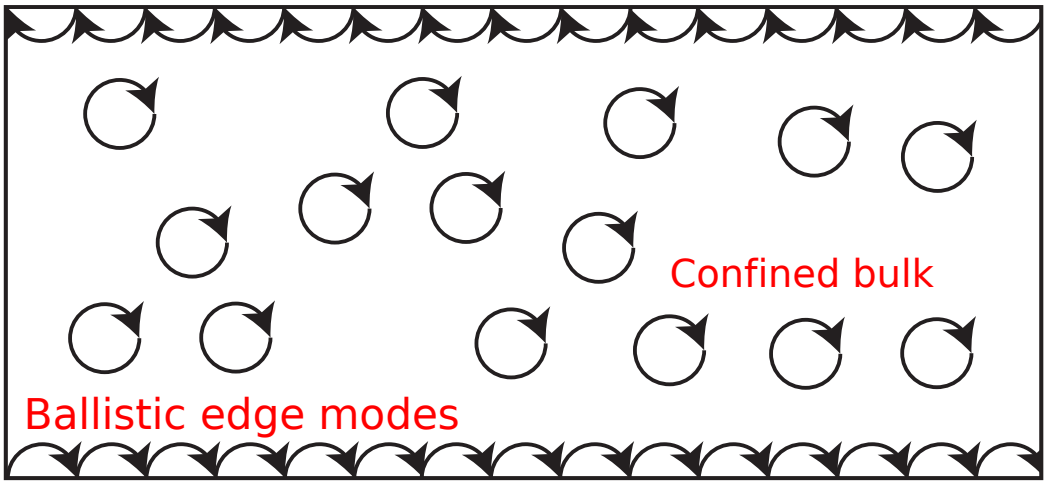

Figure 2.6: A schematic showing the Lorentz force acting on electrons, forming confined orbits in the bulk of the system and edge modes at the edges of the current channel.

2.2.3 Transport in high magnetic field

The Hall effect is a classical phenomenon in which the trajectories of charge carriers are deflected through the Lorentz force. As the magnetic field strength is increased the Lorentz force is found to have a greater effect on the trajectory. If the magnetic field is increased, the paths of the charge carriers form closed loops which are the onset of the quantum Hall regime. With these trajectories, charge carriers in the system are localised and not free to propagate. However, the charge carriers at the edges of the current channel are elastically reflected. The Lorentz force acting on the charge carrier causes another loop to start, as shown in Figure 2.6. The electron skips ballistically along the sample edge, giving rise to an edge conduction channel. This phenomenon also occurs on the opposite edge, however the current flow is in the opposite direction[7].

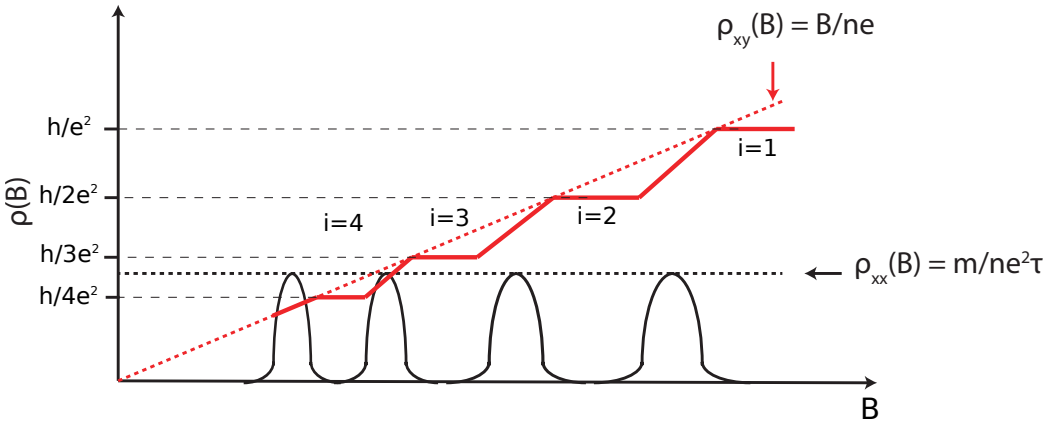

Figure 2.7: A sketch showing the quantisation of the ρ_{xy} (Red) and oscillation of ρ_{xx} (Black) in the quantum Hall regime. The dashed lines represent the classical values of ρ_{xy} and ρ_{xx}.

This regime in a real sample is dominated by the balance between charge carriers scattering off defects and impurities interrupting the enclosed orbits represented by the mobility, and the strength of the applied magnetic field causing the orbits. The onset of the quantum Hall effect (QHE) is described by the simple relation[4]:

$$1 \approx \frac{1}{\mu B} \tag{2.11}$$

Taking the measured field strength where the quantum Hall effect is observed can be used as an alternative measure for the charge carrier mobility.

The observed transport properties associated with the QHE in a two dimensional electron gas is sketched in Figure 2.7. The dashed lines represent the expected classical values of ρ_{xx} and ρ_{xy} versus B. The observed phenomena are two fold, first the $\rho_{xy}(B)$ ascends in resistivity as a series of plateau and second the longitudinal resistivity $\rho_{xx}(B)$ oscillates between 0 and the classical value $\rho_{xx} = m/(ne^2\tau)$[8].

The high magnetic field dominates the Hamiltonian of the electrons in the system,

within the quantum harmonic oscillator model, where the energy levels of the allowed degenerate edge states are[4]:

$$E_i = (i + 1/2)\hbar w \tag{2.12}$$

Where i is the quantum number of the Landau level, $\hbar$ is reduced Planck constant and w is the cyclotron frequency which is defined as the frequency of a charged particle moving through a magnetic field perpendicularly. The energy levels, or Landau levels are separated by $\hbar w$, as shown in Figure 2.8a. However, the energy levels are broadened by thermal scattering and disorder, leading to broader peaks shown in Figure 2.8b. There are two regions shown in each peak and, if the Fermi energy is within either of these regions, there are different transport properties. When there is no ballistic transport in the edge states $\rho_{xx} \neq 0$ the resistivity is defined by the classical resistivity, these are known as localised states. Then there are the extended states which allow for the ballistic transport and non dissipative transport leading to $\rho_{xx} = 0$.

Increasing the charge carrier concentration and hence the Fermi energy through these peaks in DOS accounts for the changes in the observed value of ρ_{xx}. This phenomenon can also be observed by pinning the Fermi energy to a constant value and changing the magnetic field, which changes the distance between the Landau levels.

The steps in the Hall conductance replace the classical linear description which follows $\sigma_{xy} = ne/B$. The gap in the available states between the Landau levels prevents the accumulation of charge at the edges of the channels. This means that partially filled Landau levels (within the mobility gap) do not contribute to the available charge carriers effectively quantising the Hall conductivity to $\sigma_{xy} = ie^2/h$ [4].

As the Fermi energy passes out of the mobility gap and fills the next Landau level

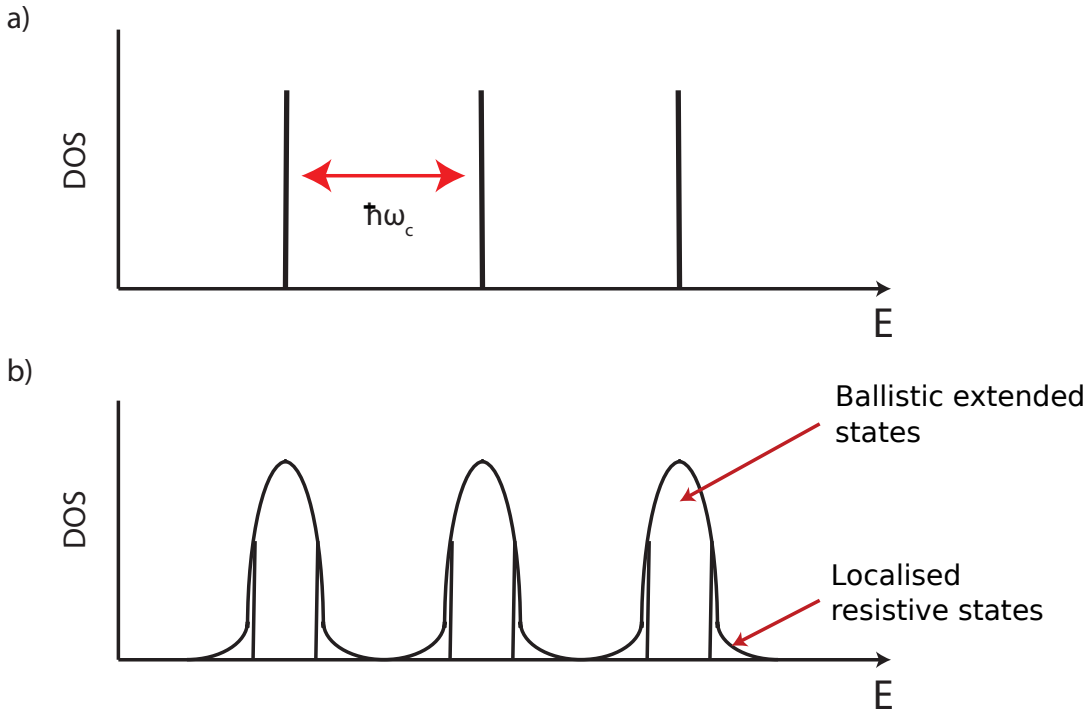

Figure 2.8: A sketch showing the density of available states with respect to energy in the quantum Hall regime, where a) represents the ideal case, zero temperature and defects, and b) a realistic case where scattering broadens the energy range for the available states.

we observe another step in the Hall resistivity.

QHE in monolayer graphene

Monolayer graphene has a unique QHE transport. Due to the different dispersion from the traditional two-dimensional electron gas systems, the energy distribution of the Landau levels is[1]:

$$E_i = v_F \sqrt{(|eh\pi Bi|)} \tag{2.13}$$

Where v_F is the Fermi velocity, and i is the Landau level number. The different Landau level energy distribution also manifests in the quantised Hall conductivity where, instead of the expected plateau occurring in steps of $\sigma_{xy} = ie^2/h$, the steps occur at values of $\sigma_{xy} = (i + 1/2)4e^2/h$[1]. These phenomena are unique to monolayer graphene, therefore measuring these QHE features in a device is truly proof that a sample is monolayer.

2.2.4 Transport for thin film conductors

For a three-dimensional material, the sheet resistance R_s is the material resistivity divided by its thickness. However for a two-dimensional material, the sheet resistance is equivalent to the resistivity used in three-dimensions. In a regular three-dimensional conductor, the resistance can be written as:

$$R = \rho \frac{l}{wt} \tag{2.14}$$

Where l is the film length, w is the film width, ρ is the film resistivity and t is the film thickness. By grouping the resistivity with the thickness, the resistance can then be written as:

$$R = \frac{\rho}{t}\frac{l}{w} = R_s\frac{l}{w} \tag{2.15}$$

$$R_s = R\frac{w}{l} \tag{2.16}$$

R_s is then the sheet resistance and resistivity in two-dimensions. The units for R_s are Ohms because it is multiplied by a dimensionless quantity. The term Ohms/square ($\Omega/\square$) is used because in Equation 2.15 it gives the resistance in Ohms of current passing from a side of a square region to the opposite side, regardless of the size of the square.

2.3 Methods of large-area graphene production

Since the first isolation of micrometer size graphene flakes in 2004[2], there has been a race to find a cost-effective method of mass producing large-area graphene[9]. Ten years on there is a wide range of methods that have been developed, each having different associated advantages and disadvantages which affect the applications that they are suitable for.

2.3.1 Liquid phase exfoliation

Large area films of monolayer and few layer graphene flakes can be produced by liquid phase exfoliation. Graphite powder is reduced to small few-layer and monolayer flakes by ultrasonication[10] or mechanical agitation[11] for long periods of time in either water with surfactants such as sodium cholate or a range of suitable solvents like N-Methyl-2-pyrrolidone (NMP)[10]. The process is outlined in Figure 2.9. As the

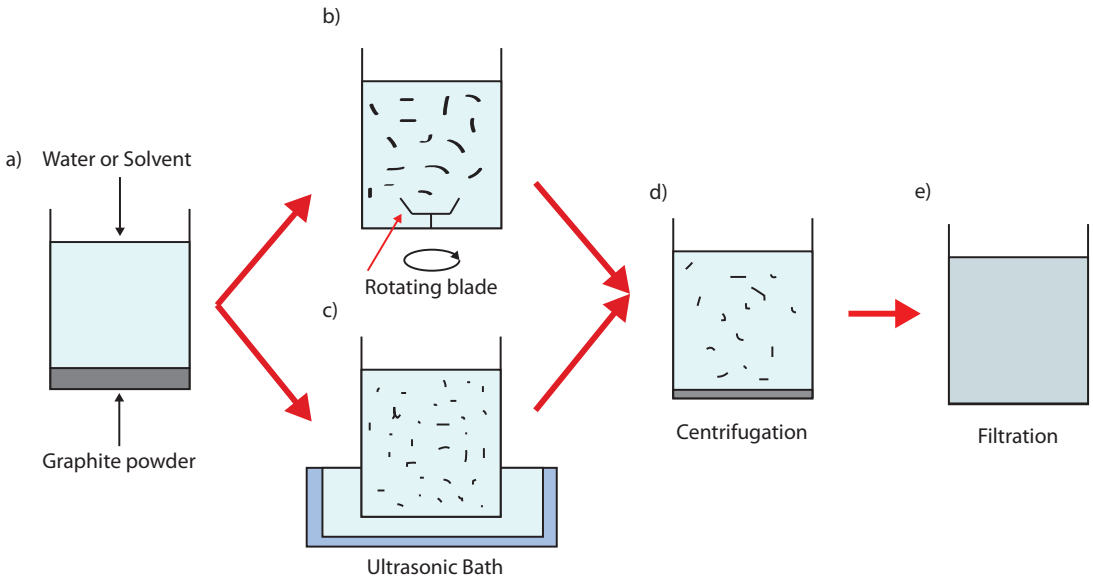

Figure 2.9: The process for producing liquid phase exfoliated graphene solutions. a) Graphite powder is added to water or a solvent such as NMP. There are two shown methods of processing to make the graphite dispersion, b) mechanical agitation where a mechanical blade is used to separate the layers of graphite in the solution or c) ultrasonic exfoliation where the graphite layers are separated using a high powered ultrasonic bath. d) The product is centrifuged to separate the different thicknesses of the graphite flakes in dispersion, where the thicker flakes sink to the bottom and the thinner flakes, including graphene, rise to the top of the solution. e) The solution is filtered to remove any remaining thick flakes leaving a suspension of monolayer and few layer graphene in water or a solvent.

exfoliation process is relatively simple and the chemicals used for the process are readily available, the total cost of production is very low.

The graphene suspension can be used to coat substrates with a continuous graphene film by drop casting, spray coating, Mayer bar coating or printing with an ink jet printer[12]. Although the produced films are continuous, they consist of many sub micrometer loosely stacked few-large and monolayer flakes. To be continuous, the film must be many times thicker than monolayer graphene, which drastically reduces the

optical transparency of the film. Furthermore, the electrical properties of the film are affected by the poor interfaces between the stacked flakes, leading to a high film resistivity.

Liquid phase exfoliated graphene films have been used as electrodes in solar cells[13] and light emitting devices (LED)[14], where the poor conductivity and optical transmission reduce the device efficiency. However, as the film is made from many stacked flakes there is a high surface roughness, which increases the surface area of the film. When used as an electrode in a battery the increase in surface area increases the storage capacity[15]. Furthermore, the inherent chemical stability of graphene improves the cycling stability of produced batteries when compared to the standard electrodes[15].

2.3.2 Epitaxial graphene grown on SiC

Graphene can be grown through the thermal decomposition of a Si or C terminated face of a silicon carbide (SiC) substrate. There are many crystalline structures of SiC that can be produced; however, for the growth of graphene, 6H- and 4H-SiC are used due to their hexagonal structure and alternating layered carbon and silicon structure illustrated for 4H-SiC in Figure 2.10a.

The process, shown in Figure 2.10b-c, uses high temperatures which are reported to range between 1200 and 1600°C. At the C terminated face of the SiC grows multilayer graphene with little control of the resulting number of layers or film uniformity[16]. On the other hand, it has been demonstrated that monolayer and few layer graphene can be grown in a controlled manner on a Si terminated face[17].

This process is scalable to produce large area graphene on an insulating SiC substrate. However, the quality and doping of the produced film are dominated by inter-

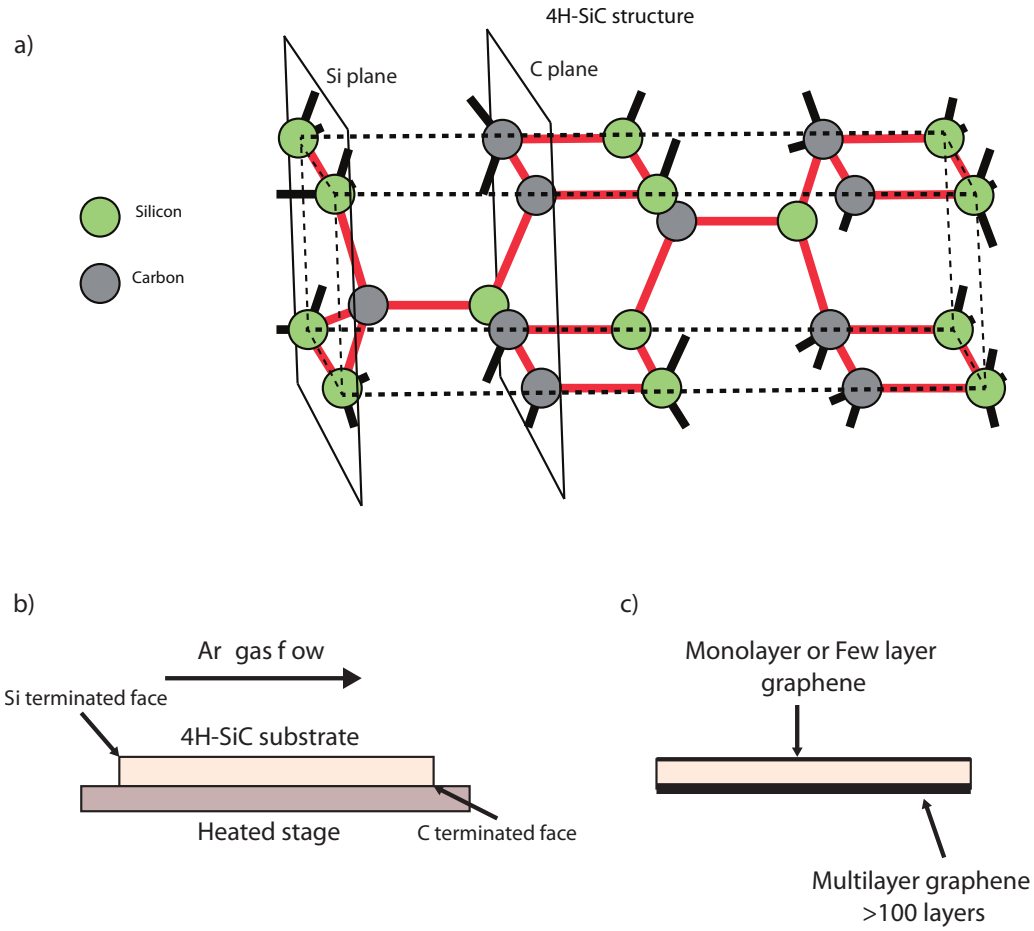

Figure 2.10: a) The structure of 4H-SiC, where the carbon and silicon atoms and planes are identified, b) the process of graphene growth on SiC, where temperatures range from 1200 to 1600°C under argon gas flow, c) monolayer growth on a Si terminated face and multilayer growth on a C terminated face.

action with the substrate. The solution commonly used is to decouple the graphene and the substrate through hydrogen passivation[18]. The electronic quality of graphene grown on SiC has been shown to be as high as 11000 $cm^2/(V.s)$[18] meaning that it could be used for high quality transistors[18] and metrology[19]. However, as the whole substrate is insulating, it is difficult to modify the charge carrier concentration, discussed in Section 2.2.1, and the Fermi energy which are required to access some of the interesting properties of graphene.

Although the quality of the graphene grown on SiC is high, there is a large cost of production of the large SiC crystals required as the growth substrate. Furthermore, as the grown graphene film cannot be reliably removed from the SiC substrate, this method of producing large area graphene is limited to laboratory applications.

2.3.3 Chemical vapour deposition

In 2009, it was shown that graphene can be grown on the surface of some catalytic metals using a high temperature chemical vapour deposition (CVD) process[20]. This allows for the production of large area monolayer or few layer graphene films. There are two common types of CVD graphene growth. These processes require similar growth conditions, however, the underlying mechanism governing the growth of graphene is different.

Monolayer graphene can be produced on a copper substrate[20], either a thin foil or an evaporated film, as shown in Figure 2.11 a-c. The substrates are annealed at high temperatures in a hydrogen atmosphere to clean the surface from oxides of copper. The graphene is then grown by introducing methane gas. The methane gas is cracked by the copper surface which creates carbon species that can either adsorb to the surface of the

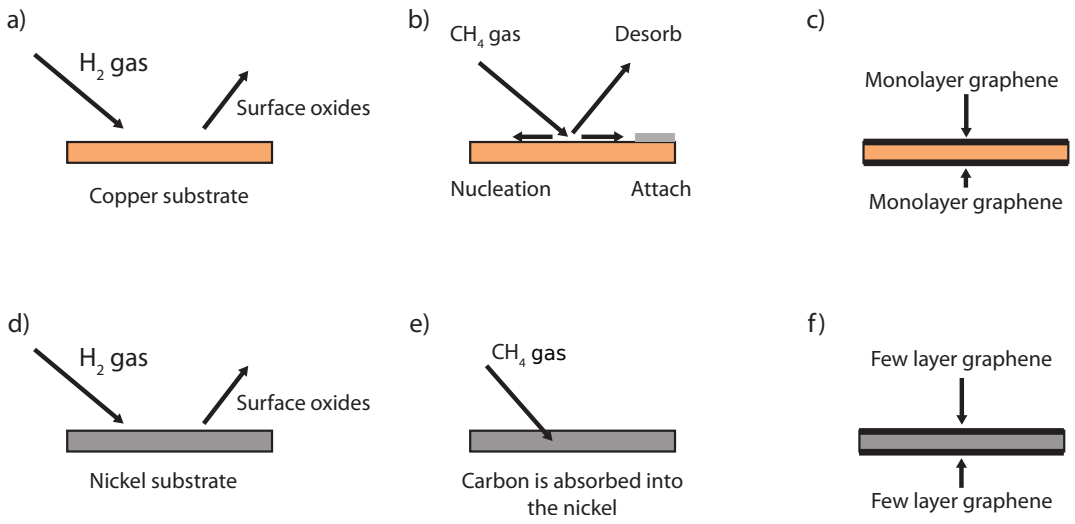

Figure 2.11: a) The annealing of a copper substrate to prepare the surface for CVD graphene growth at high temperatures of 1035°C, b) the process of the formation of graphene on the copper surface, where CH_4 is adsorped at the copper surface to form carbon species, which can form a nucleation site, attach to an already formed nucleation site or desorb from the surface, c) the final formed film shown on both sides of the copper foil, d) the annealing of a nickel substrate to prepare the surface for CVD graphene growth at high temperatures, e) the CH_4 gas adsorption is catalysed at the surface of the nickel and the resulting carbon species absorbed into the nickel substrate, f) the precipitation of few layer graphene after cooling the substrate to room temperature.

copper to seed a graphene island (a nucleation site), attach to an existing nucleation site or desorb from the copper surface. From successive attaching, the graphene islands grow in size, therefore reducing the area of the exposed copper surface. This in turn reduces the rate of catalysis of the methane adsorption and reduces the graphene growth rate. Once a continuous layer is formed there is no exposed copper to catalyse the methane adsorption, hence stopping any further growth. The resulting film is therefore limited to monolayer graphene; however impurities and defects in the copper foil can cause multilayer patches to form[21].

Few layer graphene can be grown on a nickel substrate, either on an evaporated film or on a thin nickel foil[22, 23]. The nickel substrates are annealed, as with copper, which cleans the surface of the nickel and modifies the crystalline structure of the film. This is performed by heating the substrate in a hydrogen atmosphere. When methane is introduced carbon adsorption is catalysed on the nickel surface. When the nickel substrate is cooled down to room temperature the carbon is precipitated on the surface in the form of mono and few layer graphene. It has been shown that the rate of cooling directly affects the thickness and uniformity of the produced films[24].

The grown graphene films are removed from the metal substrates using a wet etching technique, described in Section 3.2.3. The graphene films, using this technique, can be transferred onto arbitrary substrates.

2.4 Functionalising graphene for applications as a transparent electrode material

For a transparent conductor it is vital that the sheet resistance is low. High resistance electrodes have three major issues. First, the resistance of the electrode limits the size of the producible electrode. When using the electrode in a display or solar cell the electrode should have a uniform potential; however, with high-resistance electrodes there is a voltage drop as the distance from the contacts connecting the electrode to the rest of the circuit is increased. This leads to a non-uniform voltage potential across the electrode giving non uniform light emission. To minimise this effect the size of the electrode must be limited. Secondly, as there is a voltage drop across the electrode, energy is dissipated as heat. Heating of the electrode can cause components such as LED pixels to emit more or less light and can reduce the lifetime of the pixels leading to an increase in device failure rates. Finally, screens are becoming more portable and battery is operated as part of high-tech electronics. The dissipation of energy across the electrode increases energy consumption and reduces the battery lifetime of the device. This reduction in the device efficiency limits the range of products that the electrodes can be used in. Similarly for photovoltaics, high resistance electrodes reduce the efficiency of the cells and cause unnecessary thermal heating which also acts to reduce the device lifetime.

The current standard material used for transparent electrodes in displays, touch screens and solar cells is indium tin oxide (ITO) which has low resistivity (10 Ω / $\square$) while having a high optical transmission (85%) with no optical hazing[26, 27]. For graphene to fulfil the requirements of a transparent conductor it must have similar performance as ITO films. Currently monolayer graphene has been shown to have high

optical transmission (>97%), however, the resistivity is typically in excess of 1KΩ/□ and the cost of production of CVD graphene far eclipses that of ITO, as discussed in Section 4.5 and 6.5. To make graphene viable as a transparent conductor it must be functionalised to reduce the resistivity and the production costs while maintaining the high optical transmission.

2.4.1 Reduced graphene oxide

Graphene films produced through liquid phase exfoliation have to be thick to ensure full continuity; this in turn reduces the optical transmission making these films unsuitable as transparent electrodes.

Reduced graphene oxide is a cost-effective alternative material derived from liquid phase exfoliation, as discussed in Section 2.3.1, used for making thin transparent graphene films on arbitrary substrates. Graphene is insoluble in water, although can exist in a suspension. This leads to issues with the production of uniform liquid phase exfoliated films when the carrier water evaporates leaving a coffee ring distribution. A solution is to increase the solubility of graphene through oxidation, allowing for a uniform film to be produced. However, graphene oxide is insulating. To recover the conductive properties of graphene, the produced films must be reduced to form pristine graphene. This is achieved by heating the film in a reducing atmosphere or through electrochemical reduction[28, 29].

Increasing the uniformity allows for thinner films to be produced, when compared to liquid phase exfoliated graphene, which increases the optical transmission. The total cost of production of graphene films in this manner is low, while the process is also scalable to industrial quantities. Although reduced graphene oxide is a promising

material for producing large area transparent electrodes the graphene produced has a high resistivity (>30KΩ/□).

2.4.2 Graphene combined with silver nanowires

Another approach for producing high quality transparent graphene conductors is to combine silver nanowires with liquid phase exfoliated graphene. A solution of silver nanowires is sprayed onto a substrate and then coated, by spraying, in a thin layer of liquid phase exfoliated graphene, as shown in Figure 2.12. When thin films of silver nanowires or graphene through liquid phase exfoliated graphene are produced on their own they lack the continuity leading to high resistivities and nonuniformity across the substrate, as shown in Figure 2.12a and b. When combining both materials the silver nanowires help connect the graphene flakes on the substrate allowing for the thickness of graphene required for a continuous film to be reduced. This in turn increases the optical transparency of the film to 93%, while having low resistivity (30Ω/□) [30]. However, there is a degradation of the quality of the film when exposed to oxygen in the air. The solution is to encapsulate the film to prevent exposure, which reduces the optical transmission. Furthermore, the width and separation of the silver nanowires is similar to the wavelength of visible light, leading to diffraction of light passing through the film giving rise to optical hazing.

2.4.3 Intercalation of graphite and graphene

Intercalation is a process where charged molecules can enter at the edges of domains of graphite or few-layer graphene structures and then diffuse to form a continuous layer between the graphene sheets[31, 32]. The intercalation is achieved using the

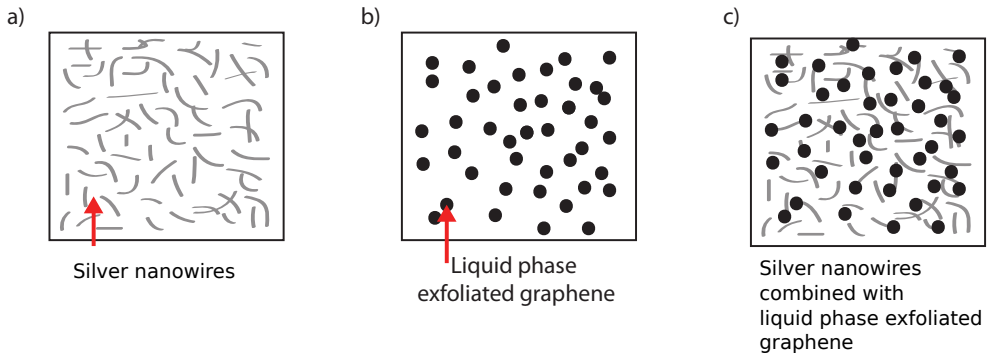

Figure 2.12: a) A distribution of silver nanowires on a substrate, b) a distribution of liquid phase exfoliated graphene on a substrate, c) the combination of silver nanowires and liquid phase exfoliated graphene on a substrate.

two zone vapour transport method described in Section 3.4. The addition of molecules changes the electrical properties of the graphite or few-layer graphene. Moreover, there are many other properties that have been reported to change for intercalated graphite samples. Through the intercalation $FeCl_3$ molecules into graphite, inter and intra plane magnetism has been achieved[32], where the magnetic layers in the structure are as thin as 0.5nm, many times thinner than magnetic films producible by thin film deposition techniques[33]. Furthermore, with the intercalation of metals like lithium and calcium in graphite, there has been an observed super conducting phase transition[34, 35].

The intercalation of charged molecules into the graphene structure increases the charge carrier concentration and hence the Fermi energy. This populates higher energy states with charge carriers leading to a higher total number of conducting states; hence there is a higher observed conduction[31], which is discussed in Section 2.2.1.

For example, lithium intercalation has been shown to reduce the resistivity of few layer graphene flakes down to 3 $\Omega/\square$ [36]. Furthermore, a similar behaviour has been

observed with $FeCl_3$ intercalated few layer graphene, reducing the resistivity to 8 $\Omega/\square$. While the conductivity of the graphene is significantly changed, there are only small reported changes in the optical transmission[31, 36], an indication that intercalation may be a possible route to tailoring the properties of graphene for application in transparent conductive electrodes.

However, the stability of intercalated compounds in air, specifically in the presence of moisture and oxygen, is generally poor. It has been reported that lithium intercalated graphene is not stable in air and rapidly deintercalates, removing the improvements to the conductive properties of graphene[36]. On the other hand, there are studies demonstrating the stability of $FeCl_3$ doped graphene to a range of solvent environments[37] and, as shown in Chapter 6, is also very stable in high humidity and high temperature in air.

Previous studies by other groups have only shown the intercalation of small exfoliated flakes. Although there have been studies that have shown the doping of large area monolayer graphene with $FeCl_3$ molecules, there has been no evidence for the intercalation of stacked CVD monolayer sheets[37]. The latter part of this thesis focuses on the development and characterisation of small few layer $FeCl_3$ intercalated samples and extending the process to create $FeCl_3$ intercalated films of large area using CVD grown graphene and epitaxial graphene.

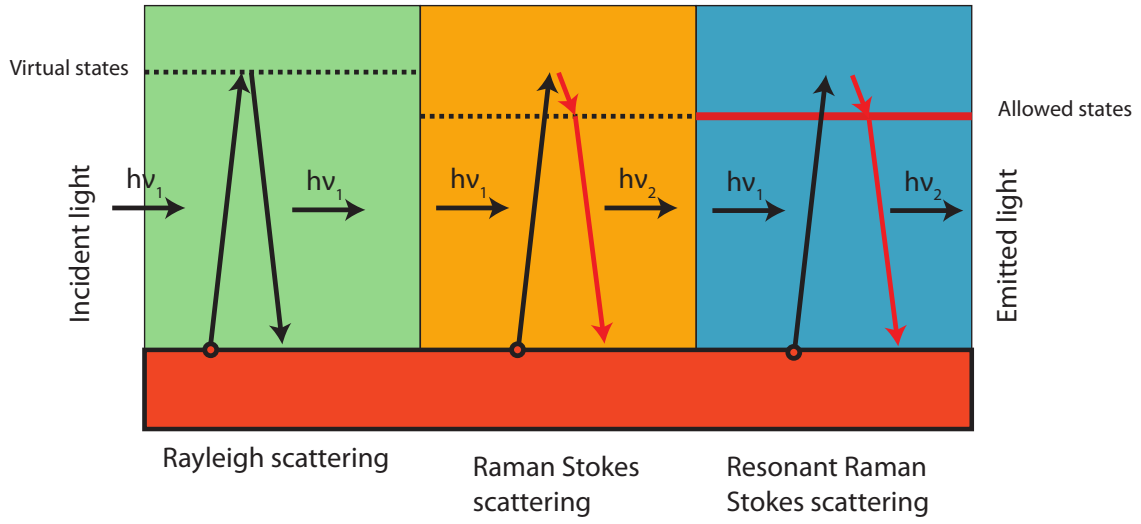

Figure 2.13: A sketch showing the photo excitation of an electron and the relaxation via a) Rayleigh scattering, b) Raman Stokes scattering via a phonon to a virtual state and c) Resonant Raman Stokes scattering via a phonon to an allowed state.

2.5 Raman spectroscopy as a fast tool for assessing the properties of graphene

Raman spectroscopy is a fundamental part of graphene research. It is a tool capable of giving the number of layers and orientation of sheets of graphene. Furthermore it yields information about the type of edge and the quality of a graphene film. Raman spectroscopy also allows for the observation of strain, doping and disorder in a non-destructive way[38].

Illuminating a material with a coherent light source excites electrons to high energy virtual and unstable states, as shown in Figure 2.13. The majority of the photo excited electrons relax to their original state emitting a photon with the same wavelength as the source of incident light. The process is known as Rayleigh scattering. However,

a direct transition is not the only route for the electron to relax to its original state. While the electron is in an excited state it can lose energy by scattering off a phonon and then relax through the emission of a lower energy photon. The emitted photon has a reduced energy, therefore a reduced frequency compared to the incident light. The difference, called the Stokes shift, in the frequency and energy is indicative of the energy of the phonon. This process is known as Stokes Raman scattering. If the electron is excited to an unoccupied energy state, as opposed to a virtual state, the process is resonant.

2.5.1 Raman scattering in graphene

Due to the continuous nature of graphene's linear band dispersion there are resonant transitions for all excitation energies. There are characteristic resonant phonon modes in graphene, indicated as D, G and the 2D modes[39], of which the representative peaks are shown in Figure 2.14. The D and 2D peak are due to the transitions shown in Figure 2.15. The excited electron scatters off the D mode phonon to an adjacent Dirac cone. However, in doing so the electron has gained momentum. In order to relax the momentum must be conserved either through the first order D mode or by the second order D mode, the D and 2D peak respectively[40]. The D peak is due to the scattering off a lattice defect, shown in Figure 2.15a, and relaxing to the initial state. On the other hand, the 2D peak is due to the electron scattering via two D mode phonons, before relaxing to the initial state where the emitted photon has lost twice as much energy as the photon emitted for the D peak. The D peak is facilitated by the presence of defects, so in a perfect graphene sample there is no D peak. As the 2D peak is independent of the defects, the peak is always present. The D peak typically

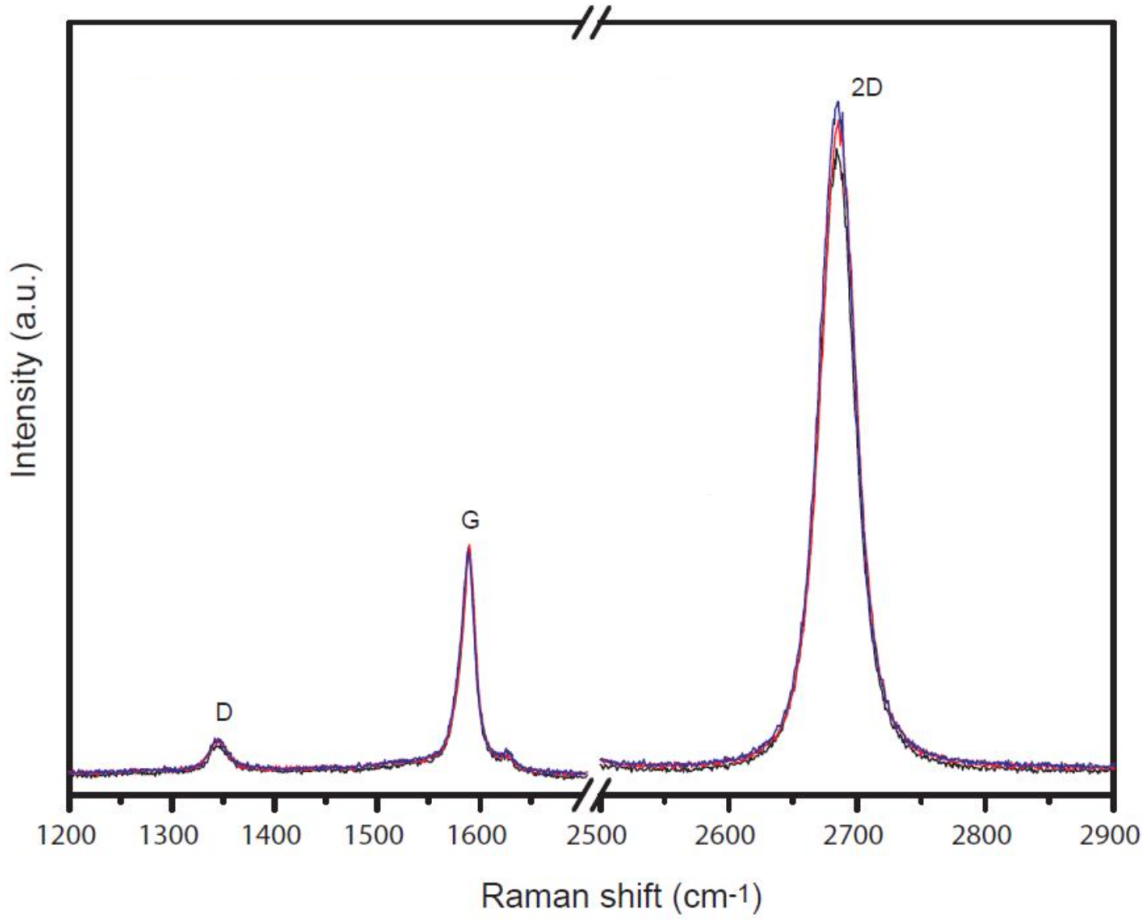

Figure 2.14: The Raman spectra of monolayer graphene measured at 532nm wavelength. The D, G and 2D peaks are highlighted.

occurs at $\approx$1350cm^{-1} and the 2D peak typically occurs at $\approx$2700cm^{-1}[39].

The G peak transition is shown in Figure 2.16. The G peak is due to the bond stretching of all pairs of sp^2 bonded carbons, however the single peaked value of 1580cm^{-1} is attributed to the fact that in an ordered graphene lattice, all of the bond angles and bond lengths are the same[41]. This peak is present for all excitation energies due to the linear band dispersion.

For monolayer graphene, the G peak intensity is roughly half the intensity of the 2D peak. The 2D peak is also a single sharp peak[39]. Increasing the number of layers modifies the measured Raman spectra. For bilayer graphene, the intensity of the G peak increases as there are more excited and relaxing electrons with increasing the number of graphene layers. The more complex band structure of bilayer graphene also changes the shape and structure of the 2D band[40]. There are four different transitions allowed each with a define energy resulting in a multipeak structure, shown in Figure 2.17. As the number of layers increases so does the complexity of the 2D peak.

The Raman spectrum of graphene is sensitive to the level of disorder in the graphene. Starting with pristine graphene adding defects to the structure causes the appearance of the D peak[40]. As the number of defects increases, the intensity of the D peak increases and the process becomes more favourable than the second order 2D transition. This simultaneously reduces the intensity of the 2D peak. As the number of defects increases, to the point where there are many six-membered rings of carbon however, they are not directly connected, the D peak is at its maximum. Further disorder starts to destroy the band structure preventing the D phonon transition from occurring. As the disorder is increased further to the point of amorphous carbon and the majority of the six-membered rings are destroyed there, is no D peak associated with graphene[41]. The disorder of the carbon film is quantified as a reduction in the ordering trajectory,

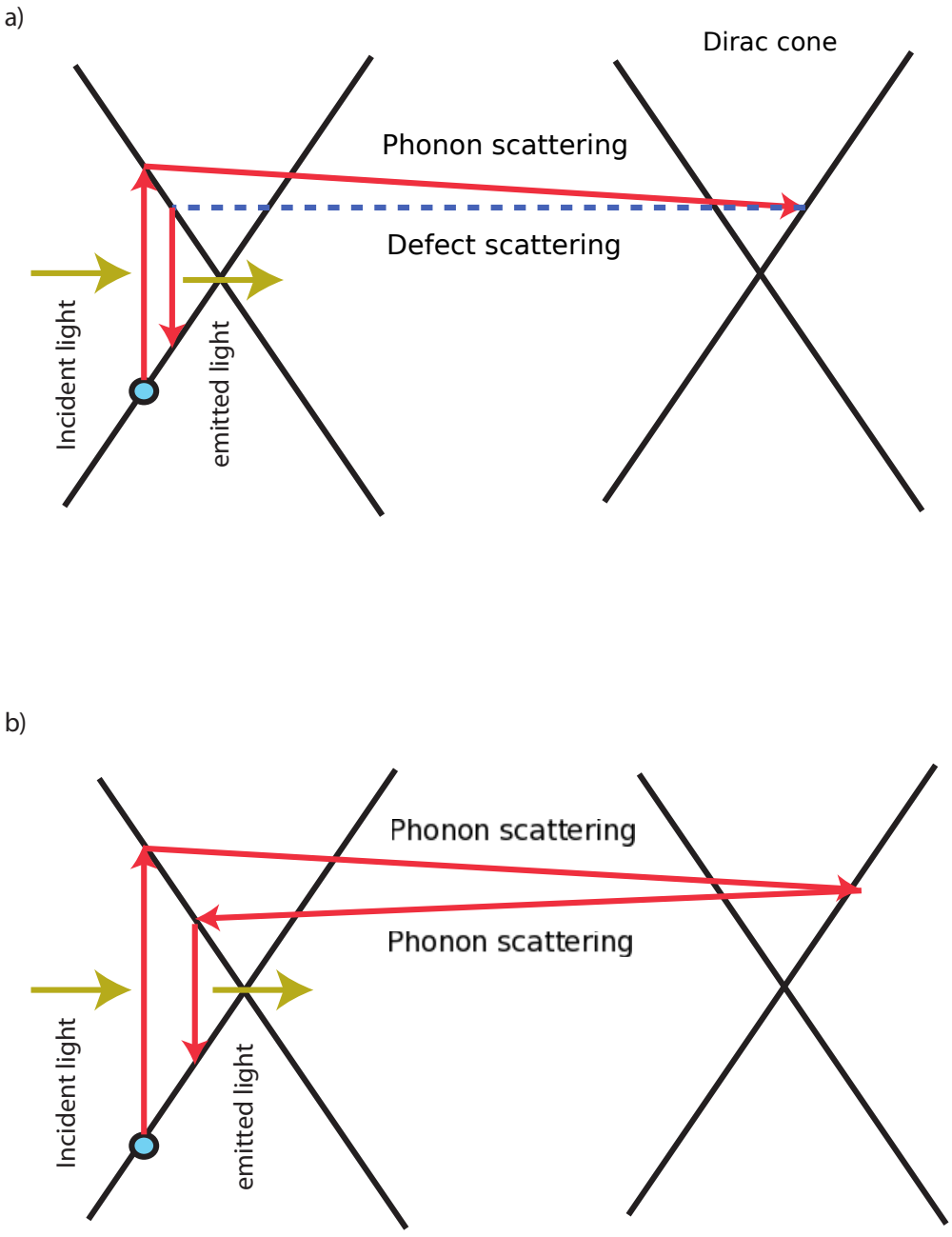

Figure 2.15: a) A schematic showing the phonon and defect scattering responsible for the D peak, b) a schematic showing the second order phonon scattering responsible for the 2D peak.

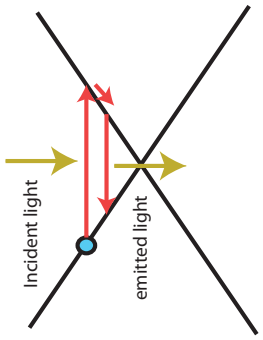

Figure 2.16: A schematic showing the phonon scattering responsible for the G peak.

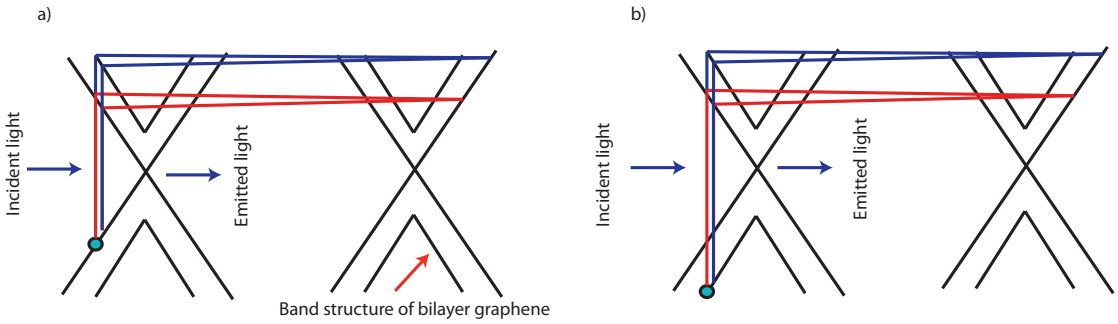

Figure 2.17: A schematic showing the four possible excitation and relaxation processes responsible for the multipeak 2D band of graphene.

as shown in Figure 2.18. Reducing the ordering, the film transitions from graphene, to nanocrystaline graphene and then to amorphous carbon.

Conversely, for disordered carbon becoming more ordered, the opposite can be said. Increasing the ordering causes the formation of six-membered ring carbon structure leading to the appearance of the D peak. As the density of the six-membered ring carbon structure increases, the D peak increases to a maximum where the six-membered ring carbon start to merge into graphene domains. Finally, as the number of defect is

reduced through ordering, the intensity of the D peak reduces. Increasing the ordering, the film transitions from amorphous carbon to nanocrystaline graphene and then finally graphene.

The G peak is also indicative of the presence of disorder. The frequency (wavenumber) of the G peak for pristine graphene is 1580cm^{-1}. As the lattice is distorted by the addition of defects the peak shifts at first up to 1620cm^{-1}, due to the formation of five- and severn-membered ring carbons. Further distortion leaves sp^2 bonded disordered carbon chains which have a G peak frequency as low as 1300cm^{-1}

Combining the information from the position and intensity of the D, G and 2D peaks gives a clear idea about the degree of order present within an sp^2 bonded thin carbon film, summarised in Figure 2.18.

Furthermore, the position of the G peak is also sensitive to the degree to which the graphene is doped. Adding dopants to the graphene increases the number of charge carriers through charge transfer which stiffens the phonon mode. This results in a shift in the frequency of the G peak. The increase in the charge carrier concentration increases the Fermi energy of the system and changes the Raman shift relative to undoped graphene. The Raman spectrum of $FeCl_3$ doped graphene has an upshifted G peak at 624cm^{-1} compared to the undoped value of 1580cm^{-1}[31].

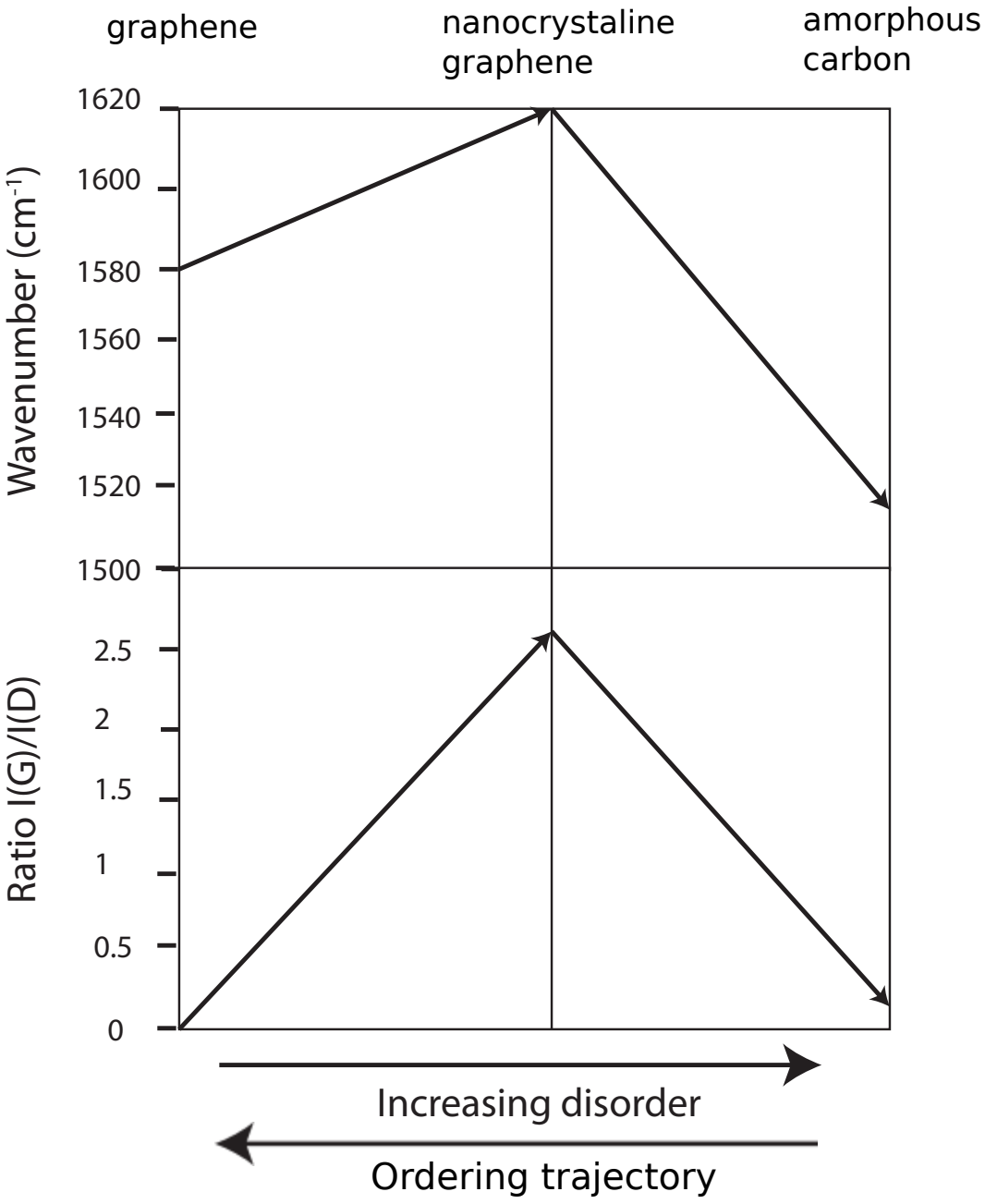

Figure 2.18: A sketch showing the effect of increasing disorder on the G peak position and I(D)/I(G) adapted from ref.[41]

.

Bibliography

[1] Katsnelson, M. I., Graphene, Ch. 1 (Cambridge university press, 2012).

[2] Novoselov, K. S., et al. Electric Field Effect in Atomically Thin Carbon Films. *Science* **22**, 666-669 (2004).

[3] Ashcroft, N. W., et al. Solid State Physics, Ch. 29 (Brooks/Cole, 1976).

[4] Datta, S., Electronic Transport in Mesoscopic Systems, Ch. 1 (Cambridge university press, 1995).

[5] Datta, S., Electronic Transport in Mesoscopic Systems, Ch. 5 (Cambridge university press, 1995).

[6] Fal'ko, V. I., et al. Weak localization in graphene. *Solid State Commun.* **143**, 33-38 (2007).

[7] Klitzing, K., The quantized Hall effect. *Rev. Mod. Phys.* **58**, 519-531 (1986).

[8] Ashcroft, N. W., et al. Solid State Physics, Ch. 1 (Brooks/Cole, 1976).

[9] Novoselov, K. S., et al. A roadmap for graphene. *Nature* **490**, 192-200 (2012).

[10] Du, W., et al. From graphite to graphene: direct liquid-phase exfoliation of graphite to produce single- and few-layered pristine graphene. *J. Mater. Chem. A* **1**, 10592-10606 (2013).

[11] Paton, K. P., et al. Scalable production of large quantities of defect-free few-layer graphene by shear exfoliation in liquids. *Nature Mat.* **13**, 624-630 (2014).

[12] Bonaccorso, F., et al. Production and processing of graphene and 2d crystals. *Mater. Today* **15**, 564-589 (2012).

[13] Bonaccorso, F., et al. Graphene photonics and optoelectronics. *Nat. Photonics* **4**, 611-622 (2010).

[14] Wu, J., et al. Organic Light-Emitting Diodes on Solution-Processed Graphene Transparent Electrodes. *ACS Nano* **4**, 43-48 (2010).

[15] Xiang, H., et al. Graphene/nanosized silicon composites for lithium battery anodes with improved cycling stability. *Carbon* **49**, 1787-1796 (2011).

[16] Rollings, E., et al. Synthesis and characterization of atomically thin graphite films on a silicon carbide substrate. *J. Phys. Chem. Solids* **67**, 2172-2177 (2006).

[17] de Heer, W. A., et al. Epitaxial graphene. *Solid State Commun.* **143**, 92-100 (2007).

[18] Pallecchi, E., et al. High Electron Mobility in Epitaxial Graphene on 4H-SiC(0001) via post-growth annealing under hydrogen. *Sci. Rep.* **4**, 4558 (2014).

[19] Janssen, T. J. B. M., et al. Quantum resistance metrology using graphene. *Rep. Prog. Phys.* **76**, 104501 (2013).

[20] Li, X., et al. Large-area synthesis of high-quailty and uniform graphene films on copper foils. *Science* **324**, 1312-1314 (2009).

[21] Wood, J. D., et al. Effects of polycrystalline substrate on graphene growth by chemical vapour deposition. *Nano Lett.* **11**, 4547-4554 (2011).

[22] Reina, A., et al. Growth of large-area single- and bi-layer graphene by controlled carbon precipitation on polycrystalline Ni surfaces. *Nano Res* **2**, 509-516 (2009).

[23] Park, H. J., et al. Growth and properties of few-layer graphene prepared by chemical vapor deposition. *Carbon* **4**, 1088-1094 (2010).

[24] Yen, W. C., et al. Direct growth of self-crystallized graphene and graphite nanoballs with Ni vapor-assisted growth: From controllable growth to material characterization. *Sci. Rep.* **4**, 4739 (2014).

[25] Bae, S., et al. Roll-to-roll production of 30-inch graphene films for transparent electrodes. *Nature Nanotech.* **5**, 574-578 (2010).

[26] Kumar, A., et al. The race to replace tin-doped indium oxide: which material will win? *ACS Nano* **4**, 11-14 (2010).

[27] Hecht, D. S., et al. Emerging transparent electrodes based on thin films of carbon nanotubes, graphene, and metallic nanostructures. *Adv. Mater.* **23**, 1482 (2011).

[28] Eda, G., et al. Large-area ultrathin films of reduced graphene oxide as a transparent and flexible electronic material. *Nature Nanotech.* **3**, 270-274 (2008).

[29] Gomez, C., et al. Electronic Transport Properties of Individual Chemically Reduced Graphene Oxide Sheets. *Nano Lett.* **7**, 3499-3503 (2007).

[30] Jurwicz, I., et al. Insulator-Conductor Type Transitions in Graphene-Modified Silver Nanowire Networks: A Route to Inexpensive Transparent Conductors. *Adv. Func. Matter.* **24**, 7580-7587 (2014).

[31] Khrapach, I., et al. Novel Highly Conductive and Transparent Graphene-Based Conductors. *Adv. Matter.* **24**, 2844-2849 (2012).

[32] Bointon, T. H., et al. Approaching Magnetic Ordering in Graphene Materials by FeCl3 Intercalation. *Nano Lett.* **14**, 1751-1755 (2014).

[33] Bader, S. D., et al. Thin film magnetism. *Proc. IEEE* **78**, 909-922 (1990).

[34] Weller, T. E., et al. Superconductivity in the intercalated graphite compounds C_6Yb and C_6Ca. *Nat. Phys.* **1**, 39-41 (2005).

[35] Pan, Z. H., et al. Electronic Structure of Superconducting KC_8 and Nonsuperconducting LiC_6 Graphite Intercalation Compounds: Evidence for a Graphene-Sheet-Driven Superconducting State. *PRL* **106**, 187002 (2011).

[36] Boa, W., et al. Approaching the limits of transparency and conductivity in graphitic materials through lithium intercalation.*Nat.Comm.* **5**, 4224 (2014).

[37] Song, Y., et al. Iron (III) Chloride doping of CVD graphene. *Nanotechnology* **25**, 395701 (2014).

[38] Ferrari, A. C., et al. Raman spectroscopy as a versatile tool for studying the properties of graphene. *Nat. Nanotech.* **8**, 235-246 (2013).

[39] Ferrari, A. C., et al. Raman spectrum of graphene and graphene layers. *Phys. Rev. Lett.* **97**, 187401 (2006).

[40] Ferrari, A. C., Raman spectroscopy of graphene an graphite: Disorder, electron-phonon coupling, doping and non adiabatic effects. *Solid State Comm.* **143**, 47-57 (2007).

[41] Ferrari, A. C., et al. Interpretation of Raman spectra of disordered and amorphous carbon, *Phys. Rev. B* **61**, 14095 (2000).

Chapter 3

Experimental methodology and fabrication

3.1 Introduction

Methods of graphene fabrication have advanced from the micro mechanical exfoliation of graphite for micrometer size graphene flakes for fundamental research in condensed matter physics[1], to being able to viably produce up to 30 inch continuous films for use as transparent electrodes in displays[2]. Progress towards commercially viable graphene electronics depends on the improvements of the graphene growth techniques and the methods and materials used for graphene functionalisation and device fabrication. Furthermore, the development of traditional and new characterisation techniques provides constructive feedback for growth and manufacturing processes. In this chapter, I cover the fabrication techniques used in this work for producing graphene and doped graphene by $FeCl_3$ intercalation, the methods used to fabricate graphene microscopic devices and the characterisation techniques used for determining quality, doping and structure of graphene studied in this work.

3.2 Graphene fabrication

There are many methods of producing graphene as described in Section 2.3. In this thesis, I have fabricated graphene by mechanical exfoliation and chemical vapour deposition (CVD) on copper (Cu); furthermore I also used graphene on SiC which was provided by my collaborator, Prof R. Yakimova (Linkoping University) and few-layer graphene grown on nickel (Ni) which was purchased from graphene supermarket. Firstly, I will describe the mechanical exfoliation of graphite onto glass or silicon (Si) substrate covered with 285nm thick SiO_2 to produce flakes of monolayer and few-layer graphene. Secondly, I will describe the growth of graphene on the surface of copper

using a cold walled (CVD) technique to produce large continuous films of monolayer graphene which can be transferred on to flexible or rigid substrates.

3.2.1 Mechanical exfoliation

To produce monolayer and few-layer graphene flakes I used mechanical exfoliation of natural graphite [1]. For this process, graphite is placed on adhesive tape, as shown in Figure 3.1a, and peeled multiple times to create an area of thin graphitic material spread on the surface of the tape, illustrated in Figure 3.1b. A cleaned SiO_2/Si or glass substrate is placed on the surface of the tape and pressed firmly, as shown in Figure 3.1c. The substrate is peeled from the tape giving a random array of graphitic flakes deposited on the substrate surface with a wide range of thicknesses. The substrate is examined under an optical microscope, where optical contrast measurements (discussed in Section 3.5.1) are used to find the thinnest flakes which are monolayer and few-layer graphene with a size up to 200 μm^2. Some examples of the obtained images are shown in Figure 3.1d and e.

3.2.2 CVD graphene growth on copper

Large area monolayer graphene is produced by chemical vapour deposition at high temperatures under a controlled hydrogen (H_2) and methane (CH_4) atmosphere on copper foils [2, 3]. The high temperatures required for growth can be achieved with either a hot walled tube furnace or a cold walled furnace. In a hot walled, furnace a quartz tube and substrates within are heated radiatively. In a cold walled reactor, a stage is heated by a resistive element [4]. The two furnaces are shown in Figure 3.2a and b respectively. There are also alternative cold walled techniques including

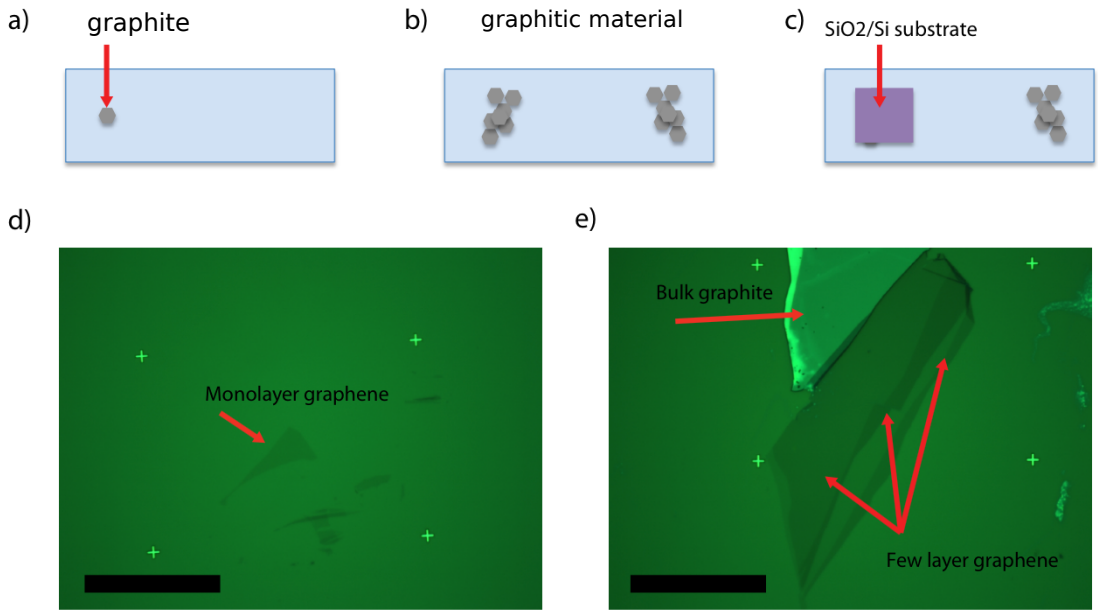

Figure 3.1: The process of mechanical exfoliation of graphite: a) graphite placed on adhesive tape, b) repeated peeling to create an array of graphitic flakes, c) a substrate placed on the surface of the adhesive tape, d) and e) examples of photographs showing monolayer and few-layer graphene and bulk graphite on a SiO_2/Si substrate under 564nm illumination (scale bar:25μm).

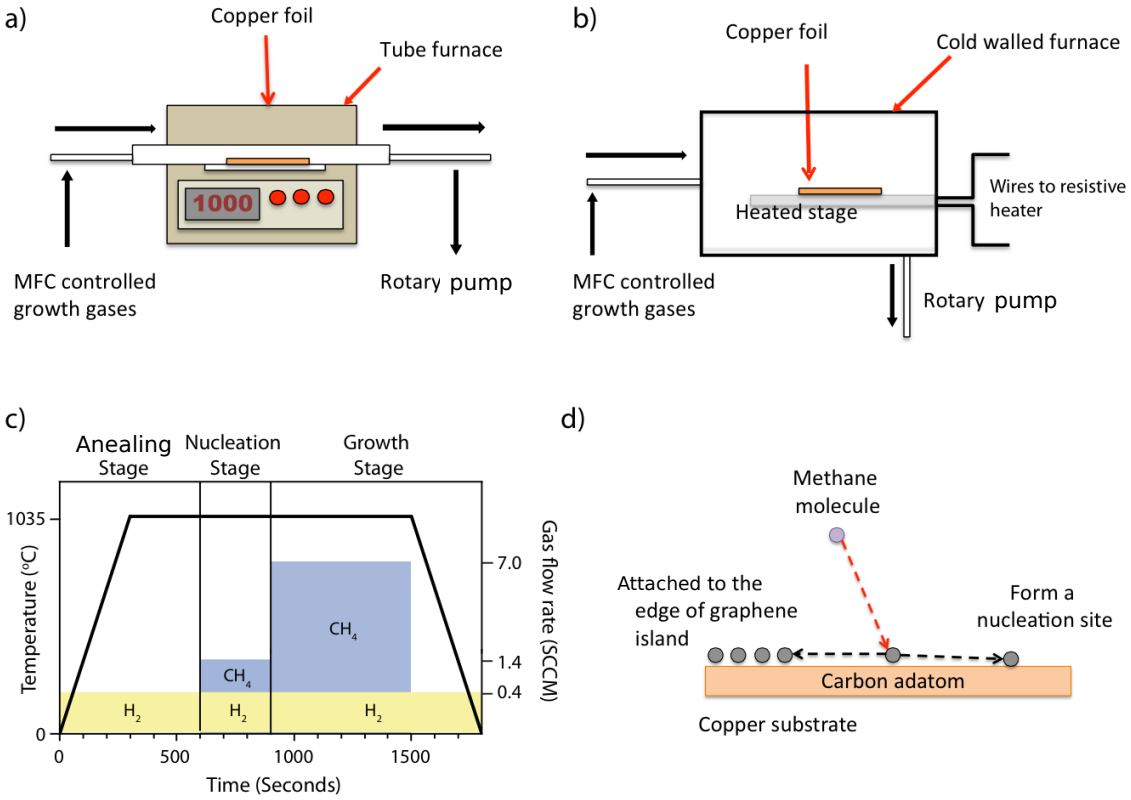

Figure 3.2: a) A schematic of the hot walled furnace used for CVD growth on copper; MFC indicated a mass flow controller for controlling the mixture of growth gases b) a schematic of a resistively heated cold walled furnace used for CVD growth on copper, c) a graph demonstrating parameters for growing graphene on copper in a cold walled furnace, d) a diagram showing the interactions of carbon adatoms during the nucleation and growth stages.

inductive heating [5], halogen bulbs [6] and high energy plasma [7]; however they are not covered in this thesis.

Copper foils (25 μm thick; Alfa Aesar; 99.999% pure) are placed within the chamber before this is sealed. Air is removed from the chamber through successive evacuations and purging with argon gas. There are three stages to the CVD growth process: copper annealing, graphene nucleation and graphene growth, as outlined in Figure 3.2c.

The annealing stage of the copper foil has the role of reducing surface oxides and defects; this is performed at 1035°C in a H_2 atmosphere at a pressure of 0.1 mbar for 10 minutes. In the nucleation stage, graphene islands are grown onto the copper surface using a mixture of H_2 and CH_4 gases which are flowed into the chamber with a ratio of 2:7, at 1035°C and 0.27 mbar . The decomposition of CH_4 is catalysed at the surface of the copper and releases carbon adatoms which form nucleation sites on the copper surface or attach to the edges of existing nucleation sites, as illustrated in Figure 3.2d. As more adatoms attach to the edges of the nucleation sites, they grow to form graphene islands. In the final growth stage, the graphene islands grow to form a continuous film, in this stage the flow rate of CH_4 and the chamber pressure are increased to boost the rate at which carbon adatoms attach to the graphene islands. The islands continue to grow until they coalesce into larger clusters and finally form a continuous film. Further growth is suppressed as the impermeable graphene film masks the copper substrate stopping any further catalysis of CH_4 decomposition for carbon adatom production.

The three stage process is used to achieve a high quality film as described in detail in Chapter 4. The size of the graphene islands, which can be considered defect free domains, must be maximised therefore reducing the overall number of domain boundaries in the completed film. By choosing low gas flow rates and pressures I minimised

the density of nucleation sites and hence increased the separation between the islands. However, low gas flow rates and pressures have been empirically shown to limit the maximum area that graphene islands can grow to. The solution is to have the growth stage where higher flow rates and pressures are used to increase the size of graphene islands to the point of coalescence [8].

3.2.3 CVD graphene transfer

The graphene grown on copper is transferred onto arbitrary substrates using the supported wet transfer process [3, 9]. PMMA [Poly(methyl methacrylate)] in an anisole solvent is spin coated onto the surface of the copper, as shown in Figure 3.3a, and cured in a vacuum. The graphene coating the underside of the foil is then removed using an argon plasma in a reactive ion etcher shown in Figure 3.3b. The foil is floated on the surface of an etchant solution (Figure 3.3c) where the etchant is nitric acid diluted 1:7 with ultrapure deionised water. In this thesis, 1M $FeCl_3$ solution is also used as an alternative etchant of the transfer process for graphene grown on nickel and copper. Once the copper is fully etched, the PMMA support and graphene are transferred in to ultrapure deionised water using a spoon, as shown in Figure 3.3d. The film is repeatedly transferred to water to clean the graphene surface from the residuals of the etchant solution. The film is lifted out of the ultrapure deionised water by a substrate and left to dry shown in Figure 3.3e and f. Finally, the PMMA support layer is removed using acetone, followed by an isopropyl alcohol (IPA) rinse and drying with nitrogen.

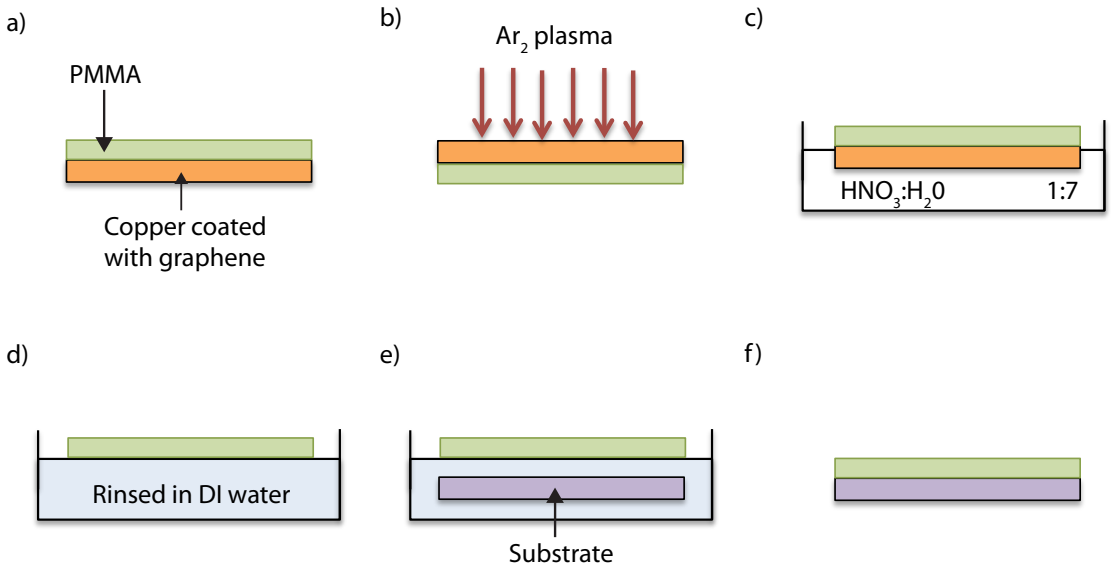

Figure 3.3: a) Copper foil is spin coated with PMMA, b) the graphene on the underside of the copper is etched using an argon plasma, c) the copper is etched in a dilute solution of nitric acid in ultrapure deionised water, d) the film is spoon transferred in ultrapure deionised water, e) the film is lifted from solution using a substrate, f) the film is left to dry prior to removal of the PMMA support.

3.3 Device fabrication

To perform electrical measurements on our samples, I must first shape the graphene flakes or film into a suitable geometry using a combination of reactive ion etching and electron beam lithography. The graphene can then be electrically contacted using electron beam lithography and thermal coating.

To pattern a graphene flake (Figure 3.4e), I spin coat a top layer of PMMA shown in Figure 3.4a. Electron beam lithography is used to expose the inverse mask pattern illustrated in Figure 3.4b and the exposed PMMA is removed using a developer solution shown in Figure 3.4f. When the sample is etched in an Ar/O_2 plasma the regions of graphene not covered by the PMMA mask are etched away, while the regions of graphene under the mask are protected, as shown in Figure 3.4c and g. Finally the PMMA mask is removed using acetone, isopropyl alcohol and nitrogen drying, giving the final etched flake shown in Figure 3.4d and h.

To electrically contact a graphene flake (Figure 3.5), I spin a bilayer of PMMA as shown in Figure 3.5a. The first layer is a 495K PMMA, where the number indicates the chain length, and the second layer is a 950K PMMA; both are baked at 180°C for 3 minutes. The pattern for the contacts is written using electron beam lithography, as shown in Figure 3.5b and f. The shorter chain length PMMA is more sensitive to electron beam exposure, furthermore backscattered electrons from the substrate expose the 495K PMMA layer more than the 950K PMMA layer giving an undercut when the PMMA is developed, as shown in Figure 3.5c. I metallise the substrate in a thermal evaporator with a 10nm-thick sticking layer of chromium and then 50nm-thick of gold also shown in Figure 3.5c. The PMMA and excess metal are 'lifted off' using heated acetone to leave just the metal contacts on the flake shown in Figure 3.5d and g. The

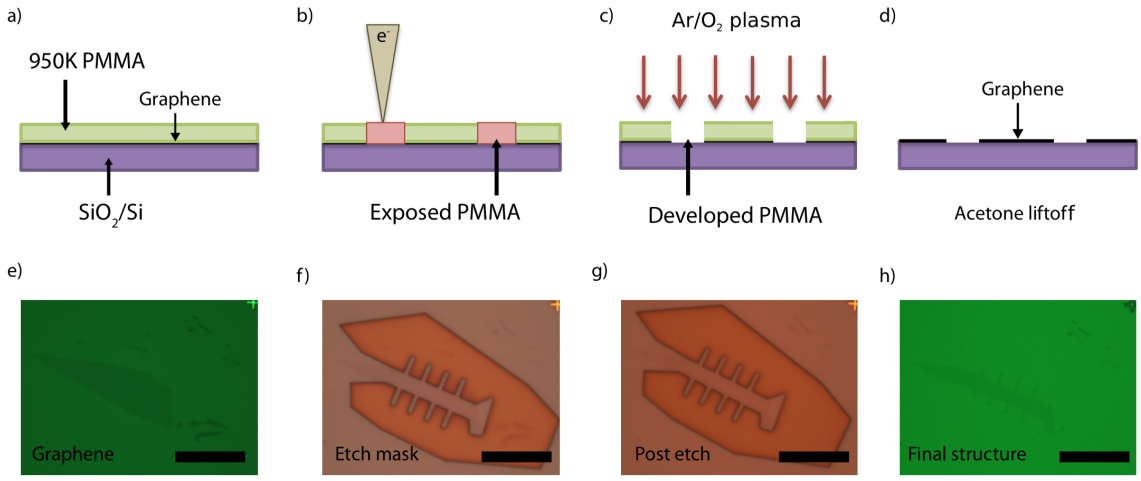

Figure 3.4: a) The substrate is spin coated with PMMA, b) the PMMA is exposed with the inverse of the mask pattern using electron beam lithography, c) the PMMA and exposed regions are etched using an Ar/O_2 plasma, d) the PMMA mask is removed to leave the patterned graphene, e) a photograph showing a monolayer graphene flake, f) a photograph showing the PMMA mask before the etching process, g) a photograph showing the PMMA mask after the etching process, h) a photograph showing the finished etched monolayer graphene flake. (scale bar:25 μ m)

finished device is then loaded into a chip carrier and wire bonded to allow for electrical measurements to be performed.

3.4 Intercalation of few layer graphene

The $FeCl_3$ intercalation of few layer graphene is performed using the two zone vapour transport method [10, 11, 12]. I load the sample into a glass tube with anhydrous $FeCl_3$ powder, as shown in Figure 3.6a. The tube is evacuated to 1×10^{-5} mBar using a turbo molecular pump and sealed using an isolation valve. The two zones are T_{Sample} and T_{Powder} which are heated to 360°C and 315°C, respectively, and are shown in Figure 3.6b. The $FeCl_3$ powder sublimes while it is heated, releasing $FeCl_3$ vapour along with a small amount of Cl_2 gas and solid $FeCl_2$. The vapour travels over the sample to the edge of the furnace and condenses in the cooler ends of the tube, shown in Figure 3.6a. As the $FeCl_3$ vapour passes over the sample, it intercalates the few layer graphene. In the final stage of the process, the temperature of the powder (T_{Powder}) is reduced first to stop the sublimation of $FeCl_3$ allowing the remaining $FeCl_3$ vapour to condense away from the sample, as highlighted in Figure 3.6b. The rest of the system is cooled and the samples are unloaded. Images in Figure 3.6c and d show the unchanged optical appearance of the few layer graphene flake before and after the intercalation process.

3.5 Characterisation

In this section I cover the methods used to characterise the number of layers of produced graphene, the degree of functionalisation of $FeCl_3$ intercalated few layer graphene to determine the suitability of $FeCl_3$ intercalated graphene as a transparent conductor

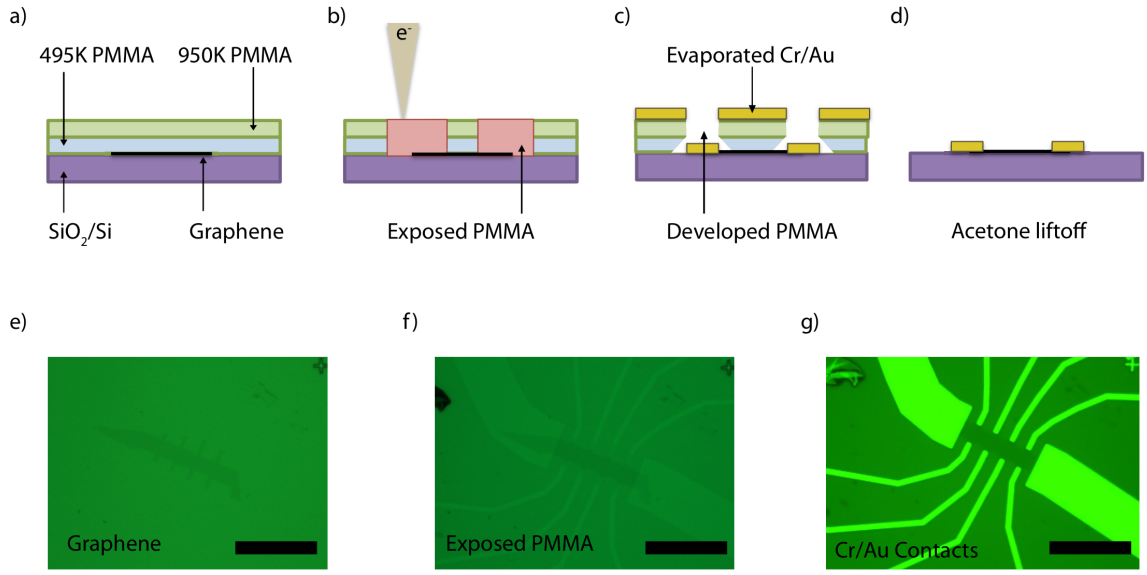

Figure 3.5: a) The substrate is coated with a bilayer of 'soft' 495K and 'hard' 950K PMMA, b) the contact pattern is exposed in the PMMA using electron beam lithography, c) the sample is developed, giving an undercut and then metallised using Cr/Au 10nm/50nm, d) the PMMA and excess metal are removed using acetone, e) an image of an etched graphene flake, f) an image that shows the pattern exposed in the PMMA, g) the remaining contacts after the metallisation and 'liftoff' process.(scale bar:25μm)

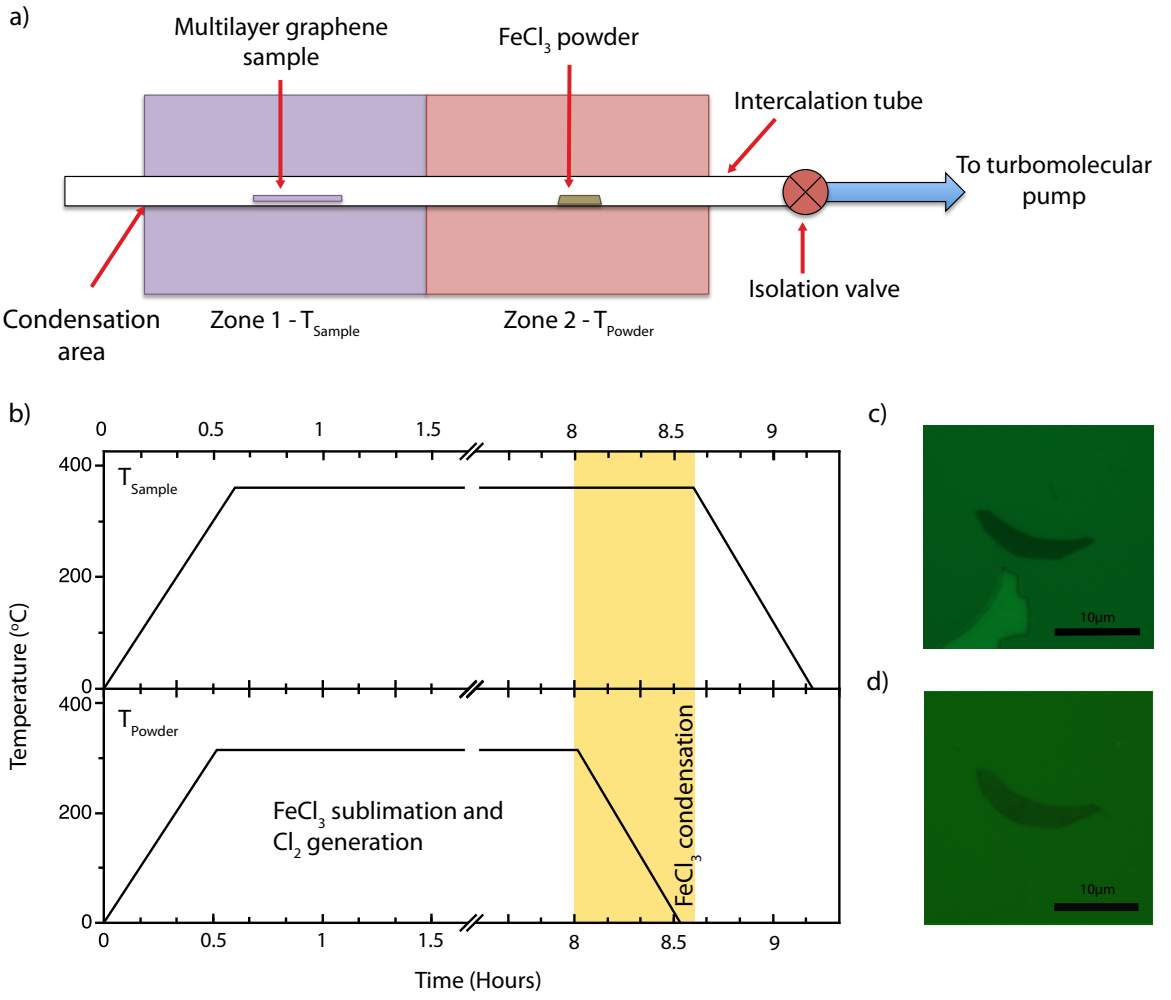

Figure 3.6: a) A schematic of the two zone vapour transport intercalation setup, b) a graph showing the temperature of each zone with respect to time from the beginning of the experiment. (c) and (d) Images showing a multilayer graphene flake at t = 0 and t = 9.6 Hours .

and characterise the growth and quality of graphene produced in cold walled CVD on a copper substrate.

3.5.1 Optical microscopy

Optical microscopy is used to non invasively determine the thickness of graphene flakes and to measure the optical transmittance of few layer graphene flakes and films. The optical contrast expressed b the Weber contrast (C) is defined in Equation 3.1, where I_{Sample} and $I_{Substrate}$ are the light intensity reflected from the sample and substrate, respectively. For graphene flakes on a SiO_2/Si substrate, there is an enhancement in the optical contrast which increases the accuracy of flake thickness identification.

$$C = \frac{I_{Sample} - I_{Substrate}}{I_{Substrate}} \tag{3.1}$$

On the bare SiO_2/Si substrate, a Fabry-Pérot etalon is formed between the Air/SiO_2 and SiO_2/Si interfaces shown in Figure 3.7a. Adding graphene on top of the SiO_2 changes the interface and hence the optical contrast depending on SiO_2 thickness and light wavelength. The maximum optical contrast for few layer graphene flakes is on a SiO_2/Si substrate of 285nm thickness, when illuminated under green light (564nm), where the contrast is directly correlated to the thickness of the film [13].

I photograph graphene flakes at x100 magnification under an optical microscope, as shown in Figure 3.7b. The measured light intensity from the image is sampled for both the graphene and the substrate and the optical contrast is calculated. To calibrate the measured contrast with respect to flake thickness, the contrast of 50 samples is measured and plotted in a histogram, as shown in Figure 3.7c. The data show discrete groups of contrasts, where monolayer and few layer graphene thicknesses

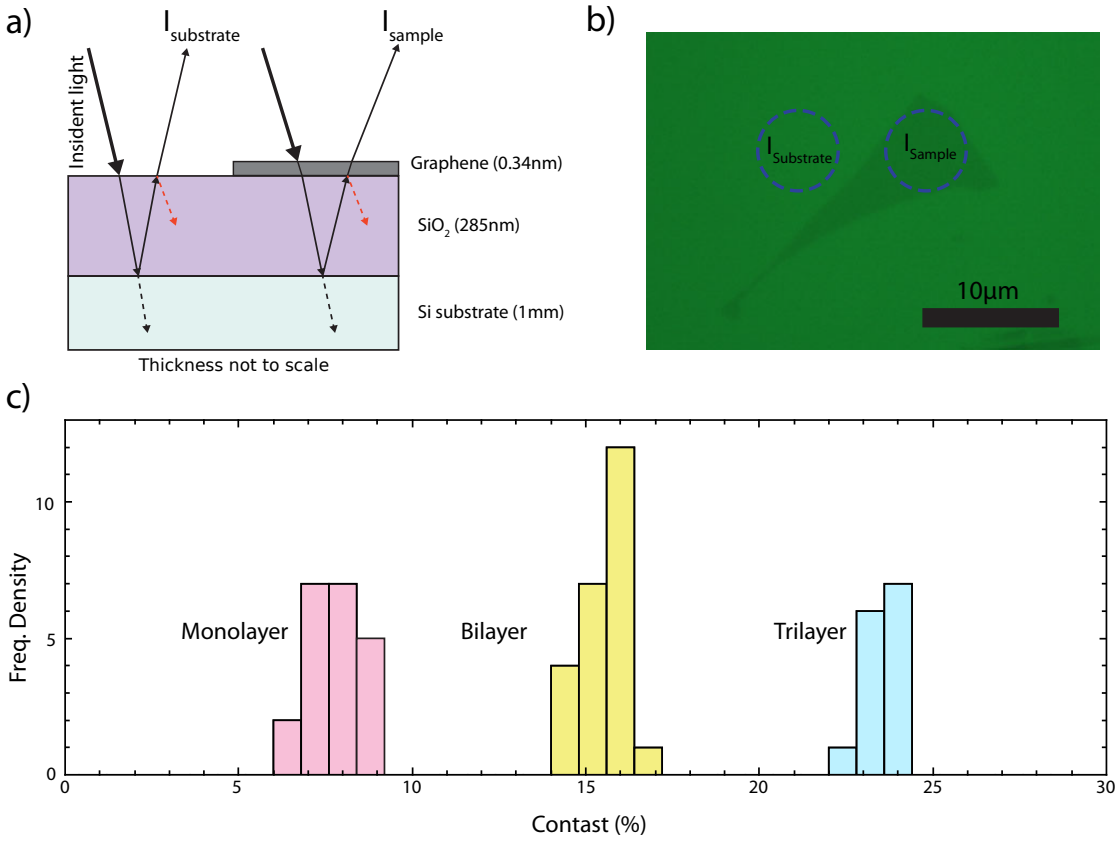

Figure 3.7: a) A schematic showing the different optical conditions for the substrate and sample intensity measurements, b) an image of monolayer graphene where the areas for substrate and sample intensity measurement are highlighted, c) a histogram showing the distribution of contrasts for 50 few layer flakes, where the monolayer graphene is coloured pink, bilayer graphene is yellow and the trilayer graphene is coloured cyan.

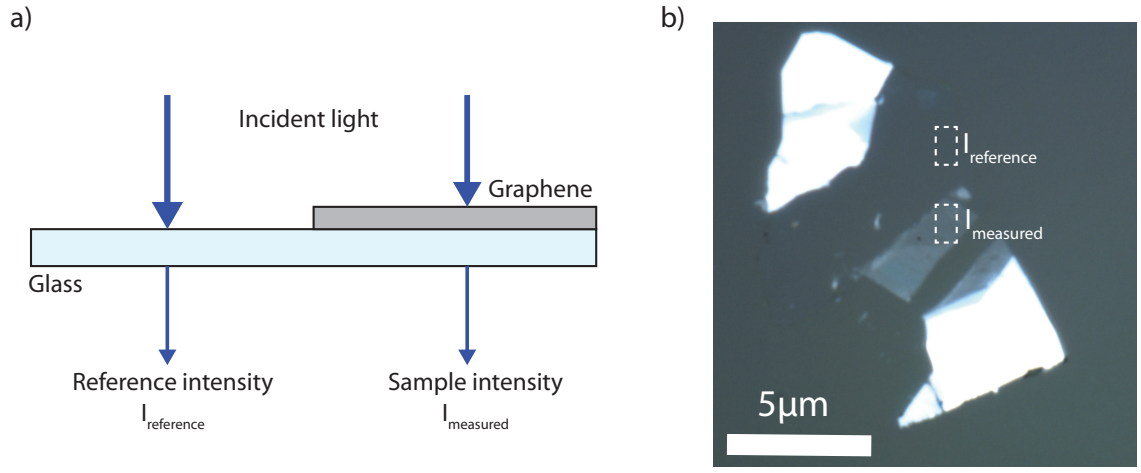

Figure 3.8: a) A diagram showing the measurement of the reference transmission intensity ($I_{reference}$) and the sample transmission intensity ($I_{measured}$), b) an image showing few layer graphene on a glass substrate; the highlighted regions are the areas where the reference transmission intensity and the sample transmission intensity where measured.

are identifiable.

The optical transmittance (T) is the fraction of light that passes through an object ($I_{measured}$) with respect to the total intensity of light passing though a reference medium ($I_{reference}$). This is given in Equation 3.2 and illustrated in Figure 3.8a.

$$T(\lambda) = \frac{I_{measured}(\lambda)}{I_{reference}(\lambda)} \tag{3.2}$$

To measure the optical transmittance, a glass substrate is used for both graphene flakes and films in a transmission microscope under x40 magnification. A reference measurement is taken through the glass substrate away from any graphene flakes or films. The reference intensity is measured for wavelengths between 350-800 nm on the bare glass substrate shown in Figure 3.8b. The sample intensity is then measured and the sample transmittance as a function of wavelength is estimated. When comparing

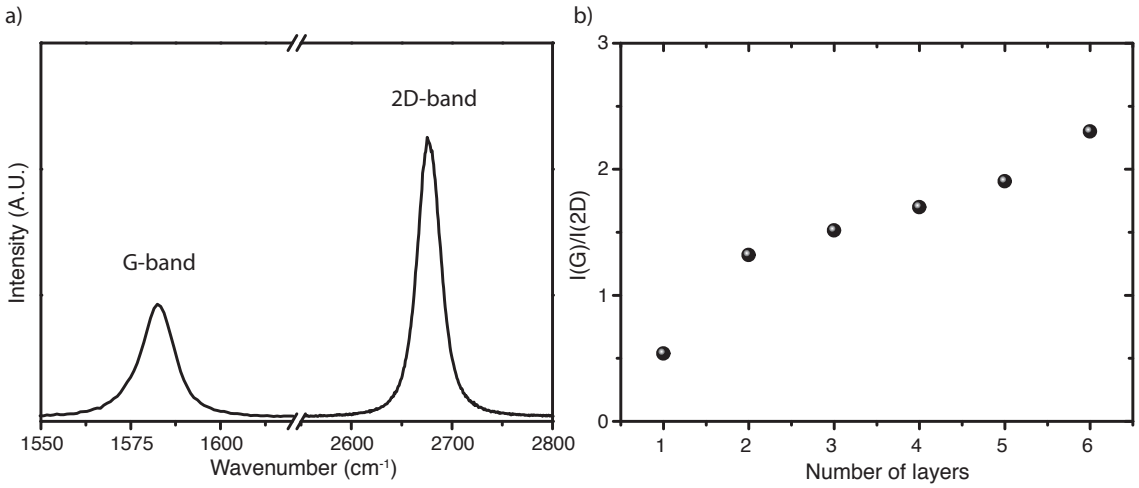

Figure 3.9: a)A Raman spectrum of monolayer graphene showing the G- and 2D-bands, b)a plot of the ratio between the intensities of the G- and 2D-bands with respect to the number of graphene layers. Raman spectra were measured under x100 magnification.

the optical contrast of materials, the industry standard approach is to take the optical transmission at 550nm.

3.5.2 Raman spectroscopy

The Raman spectrum of graphene can be used to determine the number of layers, the order/disorder present in a carbon film including graphene and the doping in few layer graphene due to $FeCl_3$ functionalisation.

Number of layers

Using Raman spectroscopy there are three methods of determining the number of layers present in a graphene film or flake. These methods refer to graphene on a substrate which does not interact with graphene.

The first method,, is to compare the ratio of the intensity of the G band (I(G)) to

that of the 2D band (I(2D)) for A-B stacked graphene. Figure 3.9a shows that as the number of layers of graphene increases, so does the ratio I(G)/I(2D) from ≈ 0.5 for monolayer graphene, to ≈ 1.2 for bilayer graphene and ≈ 1.5 for trilayer graphene and so forth, as shown in Figure 3.9b. As the number of layers increases beyond three the change in I(G)/I(2D) becomes more subtle and hence, it becomes increasingly difficult to accurately determine the number of layers using this method[14].

The second method, is to analyse the structure of the 2D-band. For monolayer graphene the 2D-band can be fitted using a single lorentzian function, as shown in Figure 3.10a. As the number of layers increases, the 2D-band shows a multipeak structure. Bilayer graphene 2D-band can be fitted with four peaks and trilayer graphene with six, shown in Figure 3.10b and c respectively. For graphene thicker than three layers, the peaks merge, as shown in Figure 3.10d, preventing the accurate determination of the structure; however the 2D-band structure is distinctive from that of bulk graphite, which shows a broad two peaked 2D-band citeferrari2006.

The final method refers to graphene on a Si/SiO_2 substrate, and compares the intensity of the Si-band (I(Si)) of the substrate to that of the G-band of graphene. As the number of layers is increased, the intensity of the G-band relative to the intensity of the Si-band increases; the intensity if the fitted peak height with respect to the background. this is highlighted in Figure 3.11a where the Raman spectrum in the G-band region shows the relative increase in intensity as the number of layers increases. Furthermore Figure 3.11b emphasises the relationship between I(G)/I(Si) and the number of layers of graphene[15]. This method is limited to identifying up to $\approx$ seven layers of graphene, and when used in combination with the other two methods and optical contrast spectroscopy it can accurately be used to identify the number of layers of graphene for few layer graphene.

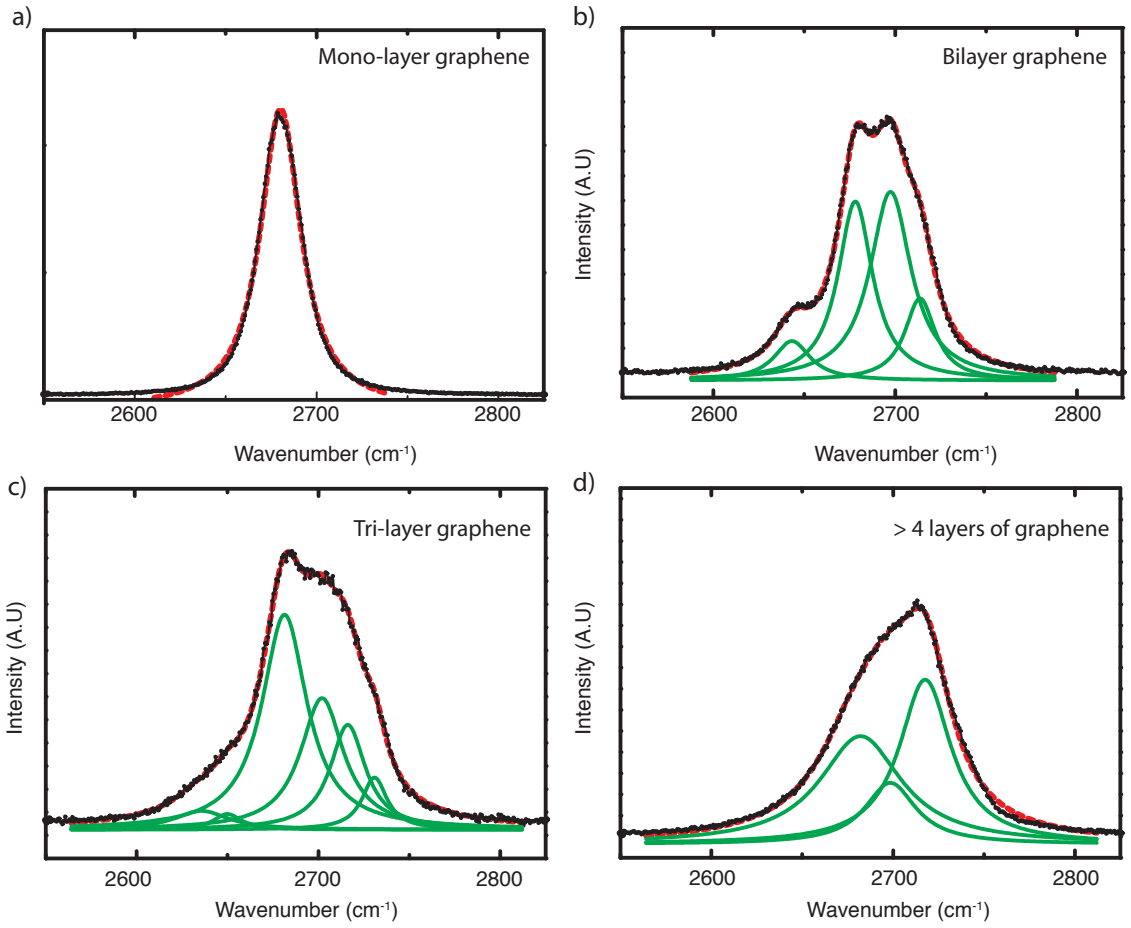

Figure 3.10: The Raman spectrum in the region of the 2D-band for: a)monolayer graphene with one fitted peak, b)bilayer graphene with four fitted peaks, c)trilayer graphene with six fitted peaks and d)greater than four layer graphene fitted with three bands.

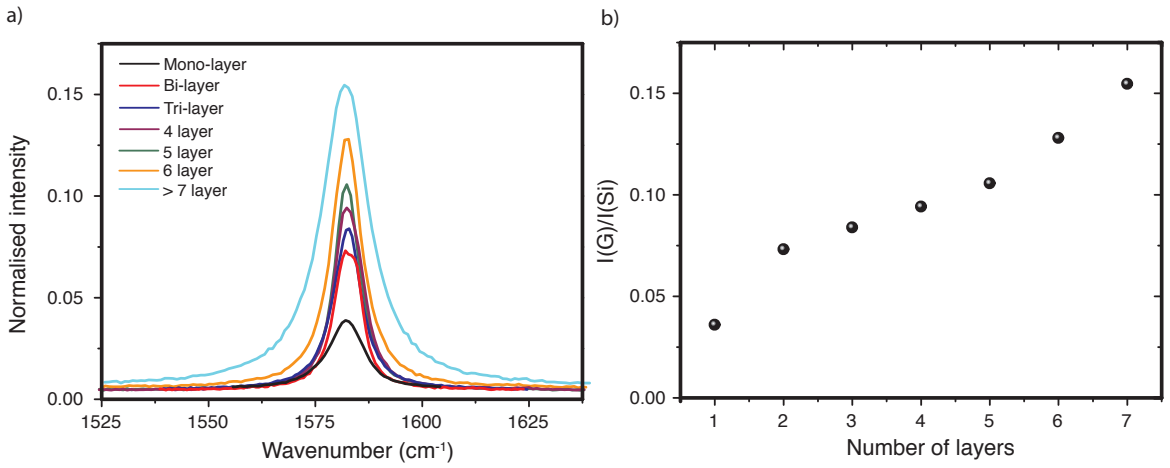

Figure 3.11: a)Evolution of the G-band with increasing number of layers of graphene; the intensity is normalised to the Si-band intensity for each sample, b)a plot showing the I(G)/I(Si) ratio against the number of layers of graphene.

Furthermore, the thickness of graphene grown on SiC substrate which interacts with the graphene can be determined from the full width half maximum (FWHM) of the 2D peak. It has been shown that there is a liner relationship between the parameter and the inverse number of layers (N) by Lee *et al.*[16]. The empirical relationship is: FWHM(2D) = (-45(1/N) + 88)[cm^{-1}].

Ordering and disorder

As discussed in Section 2.5.1, the ordering/disorder of a carbon film can be determined by Raman spectroscopy. By fitting the D-, G- and 2D-bands to extract the band intensity, full width half maximum and position, I can estimate the degree of sp^2 ordering within the sample.

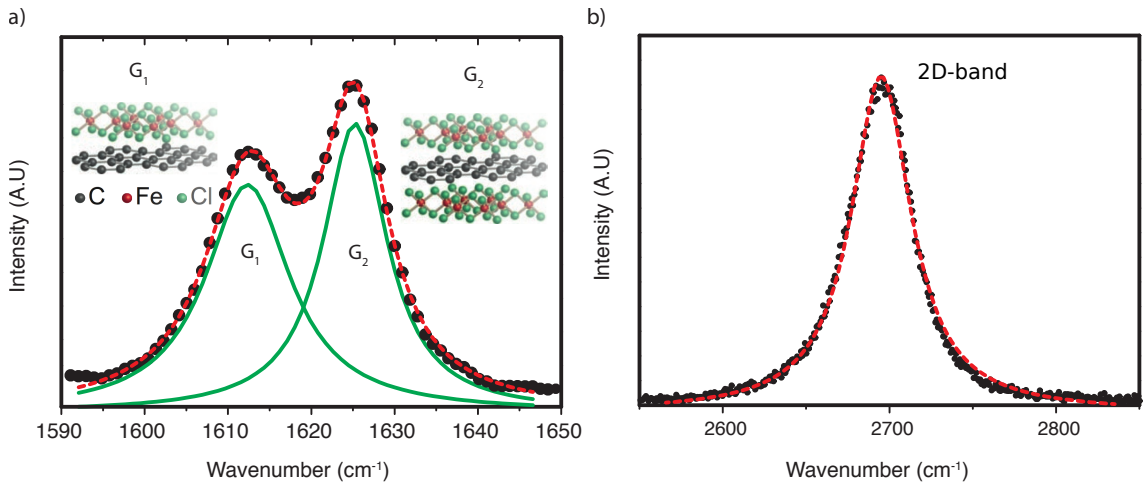

Figure 3.12: A representative Raman spectrum of $FeCl_3$ intercalated few layer graphene; a) the upshifted G-band to the G_1- and G_2-band positions; insets: the graphene/$FeCl_3$ structure for the G_1 and G_2-bands, b) the single peak structure of the 2D-bands $FeCl_3$ intercalated few layer graphene.

Doping

When few layer graphene is intercalated with $FeCl_3$ there is an upshift of the G-band due to charge transfer [11]. There are two possible bands that are formed, the G_1 and G_2 bands, as shown in Figure 3.12a. The G_1-band (1612 cm^{-1}) occurs when each layer of graphene has one adjacent layer of $FeCl_3$. The G_2-band (1625 cm^{-1}) occurs when each layer of graphene has two adjacent layers of $FeCl_3$; due to the different charge transfer from the adjacent $FeCl_3$ layers. Furthermore for intercalated few layer graphene, the structure of the 2D-band changes from a multipeak structure shown in Figure 3.10 to that of a single peak shown in Figure 3.12; due to a electrical decoupling of the graphene layers..

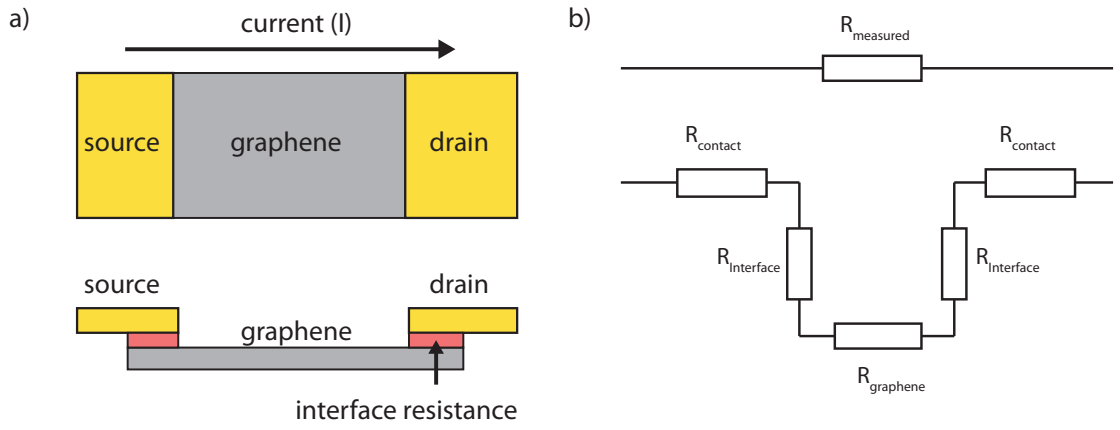

Figure 3.13: a)A schematic of a two terminal device, where yellow regions represent gold contacts, grey are graphene regions and red are the interface resistance regions, b) a diagram showing the two equivalent circuits; **Top**: the measured resistance ($R_{measured}$), **Bottom**: the series resistance of the contacts ($R_{contact}$), the interface ($R_{interface}$) and the graphene ($R_{graphene}$).

3.5.3 Electrical transport

To gain detailed information about the quality and structure of graphene samples, I perform electrical transport measurements in a range of perpendicular magnetic fields and temperatures. This subsection covers two and four terminal measurement techniques, constant current measurement, sweeping a back gate voltage and considerations of electron temperature for cryogenic measurements.

For all cryogenic measurements I use a Signal Recovery SR70025 lock-in amplifier to source and measure AC voltage, a Keithly 2400 source meter to provide the gate voltage. For DC measurements, a Keithly 2400 source meter and a Hameg 8008 LCR bridge are used.

Two terminal measurements

The simplest measurement to perform is the 'two terminal' resistance measurement, in which the graphene sample has two contacts applied as shown in Figure 3.13a. A current ($I_{applied}$) is driven between the two contacts and the voltage drop between the contacts is measured ($V_{measured}$).

$$R_{measured} = \frac{V_{measured}}{I_{applied}} \tag{3.3}$$

Applying Ohm's law (Equation 3.3) the resistance can be calculated ($R_{measured}$). However the measured resistance is not the resistance of the graphene, as the bottom part of Figure 3.13a shows that the current must pass through the contacts, interface barrier and graphene sample, each of which have an associated series resistance. This is illustrated by the two equivalent circuit diagrams shown in Figure 3.13b and Equation 3.4. In Figure 3.13b, the top panel shows the measured resistance ($R_{measured}$), whereas the bottom panel shows the series resistance of the contacts ($R_{contact}$), the interface ($R_{interface}$) and the graphene ($R_{graphene}$).

$$\frac{V_{measured}}{I_{applied}} = R_{measured} = 2R_{contacts} + 2R_{interface} + R_{graphene} \tag{3.4}$$

The contact and interface resistance contributions are sometimes larger than the resistance of the graphene. For cryogenic measurements, the wires leading to the sample require low thermal conductivity to reduce sample heating; however this increases the $R_{contact}$, hence contributing between 300-500Ω to the measured resistance. The interface between the gold contacts and the graphene is affected by the presence of insulating PMMA, glue residues left after sample fabrication, and the mismatch in the

work function between graphene and the contacts. The contribution of $R_{interface}$ can thus range between 20Ω and $1G\Omega$.

This method of measurement is suitable for devices with a large area between the contacts and graphene combined with low resistance measurement wires. An example of this is the measurement of the room temperature sheet resistivity of the graphene in a flexible touch sensor (Section 5).

Four terminal measurements

To eliminate the dependence of the measured resistance on the resistance of the measurement setup and the effect of the interface resistance, I use a four terminal measurement. Figure 3.14a shows the contact configuration where a current (I_{s-d}) is driven between the source and drain contacts. When the current is driven across the graphene sample, assuming the graphene is electrically isotropic, there is a uniform voltage drop that occurs between the source and drain contacts illustrated in Figure 3.14b, where contour lines of equivalent potential are shown. Voltage probes at the edge of the graphene sample equilibrate to the potential present at the position of the probe. Measuring the potential difference between probes V_1 and V_2 gives the longitudinal voltage drop across the length of the sample. Applying Ohm's law then allows the longitudinal resistance (R_{xx}) to be calculated, as expressed in Equation 3.5.

$$R_{xx} = \frac{V_1 - V_2}{I_{s-d}} = \frac{V_{1-2}}{I_{s-d}} \tag{3.5}$$

As an extension of this technique, I also measure transverse voltage (R_{xy}) by taking the voltage drop between the probes V_1 and V_3 and applying Ohm's law as expressed in Equation 3.6. An ideal sample with zero applied perpendicular magnetic field and

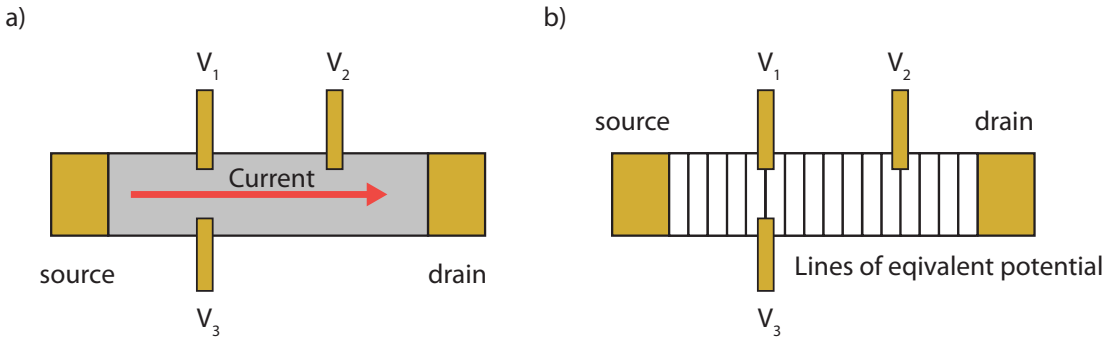

Figure 3.14: a) A schematic of the four terminal contact configuration, where R_{xx} is measured using V_1 and V_2 voltage probes and R_{xy} is measured using V_1 and V_3, b) a schematic showing the lines of equivalent voltage potential that occurs across the graphene current channel when a current is driver between the source-drain contacts.

a uniform voltage drop between source and drain contacts has $R_{xy} = 0$.

$$R_{xy} = \frac{V_1 - V_3}{I_{s-d}} = \frac{V_{1-3}}{I_{s-d}} = 0 \tag{3.6}$$

Constant current measurement

The constant current measurement is suitable for accurately measuring samples with a low resistance ($<20K\Omega$). The circuit diagram for both two and four terminal measurements is outlined in Figure 3.15a and b. When a voltage $V_{[}osc]$ is applied across the ballast resistor $R_{ballast}$ and graphene sample $R_{graphene}$, the current is given by Equation 3.7.

$$I = \frac{V_{osc}}{R_{ballast} + R_{graphene}} \tag{3.7}$$

$R_{graphene}$ is unknown, therefore I need to minimise the effect on the current in the

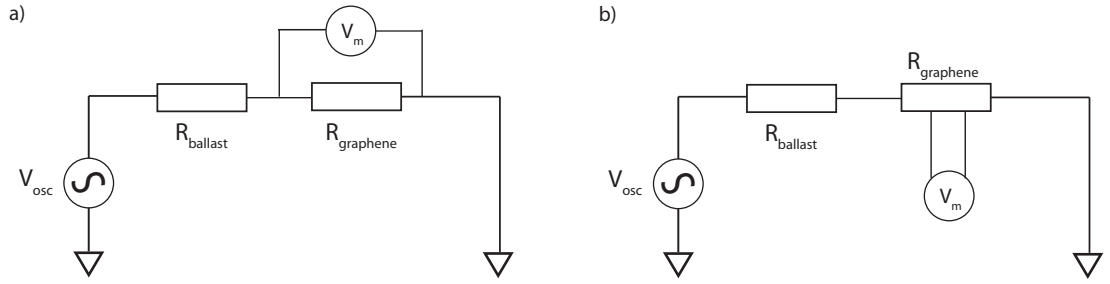

Figure 3.15: a)The two terminal configuration of the constant current measurement, b)the four terminal configuration of the constant current measurement where voltage probes are on the edge of the current channel.

circuit. This is done by imposing the condition that $R_{ballast} >> R_{graphene}$. By dividing the top and bottom of the fraction by $R_{ballast}$, as shown in Equation 3.8, and applying this condition I can define I using just V_{osc} and $R_{ballast}$.

$$I = \frac{V_{osc}/R_{ballast}}{1 + R_{graphene}/R_{ballast}} \approx \frac{V_{osc}}{R_{ballast}} = \frac{V_{1-2}}{R_{graphene}} \tag{3.8}$$

The value of the ballast resistor I use is $10M\Omega$, and $V_{osc} = 1V$ gives a current of 1×10^{-8}A and allows us to measure any graphene sample with a source to drain resistance of $<20K\Omega$ with a least 99.8% certainty in the current (I).

As described in the two previous sections, for the two terminal measurement the voltage drop is measured across source-drain of the sample and the four terminal from voltage probes at the edge of the graphene channel.

Applying a voltage to the gate

The charge carrier concentration of the graphene on a SiO_2/Si substrate is changed using the electric field effect by applying a potential difference between the graphene and Si backgate, as shown in Figure 3.16a. The induced electric field between the

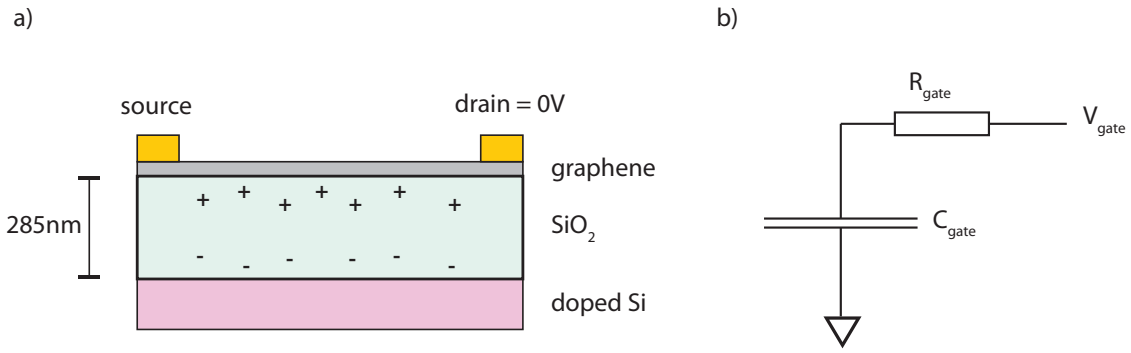

Figure 3.16: a)A schematic of a graphene device separated from the backgate electrode with a SiO_2 dielectric; the electric field generated between the two plates is indicated by the charge symbols in the dielectric, b)a diagram of the circuit used to change the backgate voltage.

graphene and gate increases the number of charge carriers in the graphene, the charge carrier concentration can then be estimated using the parallel plate capacitor model. To protect the gate electrode from dielectric breakdown due to electrical spikes or user error I use a 1GΩ resistor in series shown in Figure 3.16b.

3.5.4 Atomic force microscopy

The thickness of CVD grown carbon and graphene films on SiO_2/Si substrate are determined using a NT-MTD NTEGRA tapping mode AFM. The surface topography of a transferred carbon film grown on copper is measured, as shown in Figure 3.17a. An area which includes the substrate and the film highlighted in Figure 3.17a is sampled and the distribution of the heights is then plotted as a histogram shown in Figure 3.17b. The two peaks at lower and higher values of height represent the substrate height and the film height, respectively. Fitting each peak with a gaussian function and subtracting the height of the substrate from that of the film gives the total film

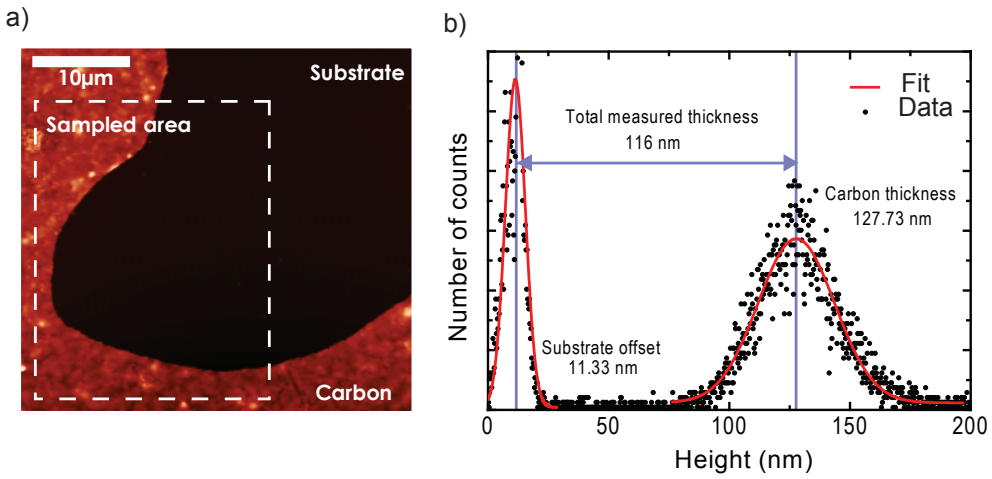

Figure 3.17: a)AFM topographic image of carbon film on a SiO_2 substrate; the highlighted region shows the sampled region for the statistical study, b) a histogram showing the distribution of measured heights from within the sampled area. Substrate and film distributions are fitted and the difference between the average heights gives the total thickness

thickness.

3.5.5 Scanning electron microscopy

During CVD growth graphene islands are formed therefore enabling to track the CVD graphene growth. For different stages of the growth process I use SEM to determine the average graphene island size and separation. SEM micrographs where taken for graphene islands transferred on to SiO_2/Si to determine the average area and separation of domains. Figure 3.18a shows a micrograph taken at 5000x magnification where graphene islands appear dark and the SiO_2 substrate is lighter. The image is then processed by inverting the colours and applying a threshold to create a two colour bitmap, as shown in Figure 3.18b. Using the Matlab image processing toolbox, each island is identified and the area is measured[17]. Figure 3.18c shows a single identified

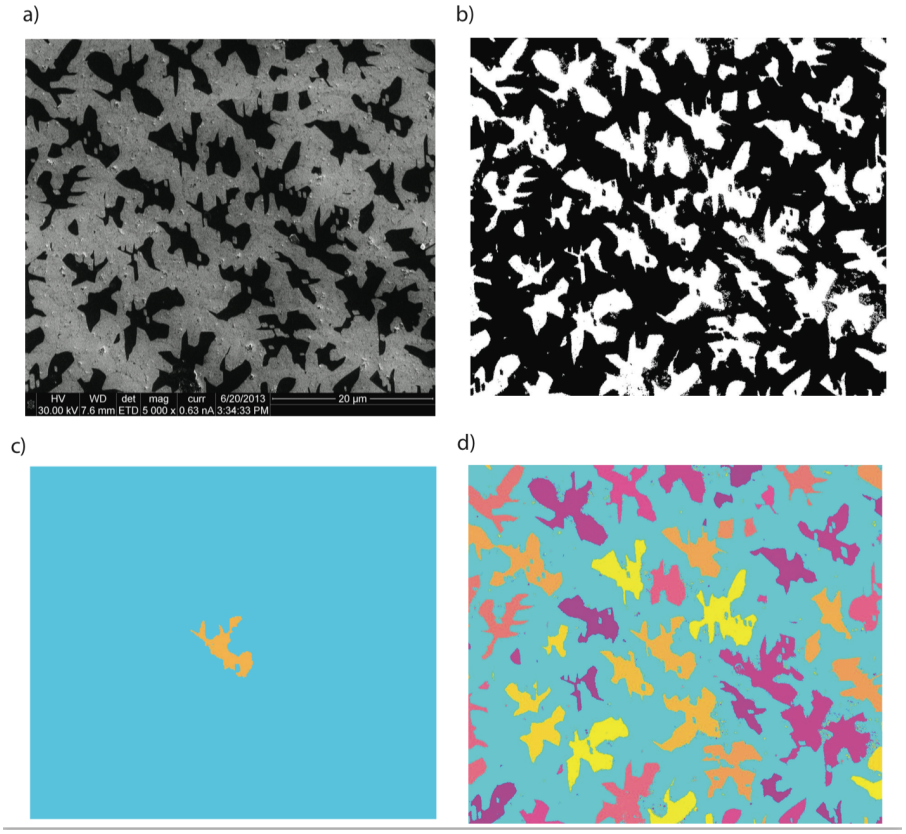

Figure 3.18: a)An scanning electron micrograph showing graphene islands (Black) on a SiO_2 substrate, b) processed micrograph with inverted intensities and applied black and white threshold, c) a single identified island extracted from the micrograph shown in false colour, d) all identified islands in the micrograph after applying a noise filter.

island on a false colour map. To reduce the effects of residues resulting from the transfer process, the data are filtered to remove any island with an area smaller than 1 μm^2. The so identified islands are given random false colour to check that no islands are connected as shown in Figure 3.18d.

$$A_{mean} = \frac{A_{islands}}{N_{islands}} \tag{3.9}$$

All calculations are based on the analysis of ten micrographs for each growth time,

where the average area of the islands is estimated by summing the area of all islands ($A_{islands}$) and dividing by the total number of islands ($N_{islands}$), as expressed in Equation 3.9. The average separation of the islands (S_{mean}) is estimated from the density of islands in Equation 3.10, where the density (d) is taken as the total number of islands ($N_{islands}$) divided by the total area of the micrograph (A_{total}).

$$S_{mean} = \sqrt{\frac{1}{d}} = \sqrt{\frac{A_{total}}{N_{islands}}} \tag{3.10}$$

Bibliography

[1] Novoselov, K. S., et al. Electric Field Effect in Atomically Thin Carbon Films. *Science* **306**, 666-669 (2004).

[2] Bae, S., et al. Roll-to-roll production of 30-inch graphene films for transparent electrodes. *Nature Nanotech.* **5**, 574-578 (2010).

[3] Li, X., et al. Large area synthesis of high-quality and uniform graphene films on copper foils.*Science* **324**, 1312-1314 (2009).

[4] Bointon, T. H., et al. High Quality Monolayer Graphene Synthesized by Resistive Heating Cold Wall Chemical Vapor Deposition. *Adv. Mater.* **Early Access**, (2015) doi:10.1002/adma.201501600.

[5] Piner, R., et al. Graphene Synthesis via Magnetic Inductive Heating of Copper Substrates. *ACS Nano* **7**, 7495-7499 (2013).

[6] Ryu, J., et al. Fast Synthesis of High-Performance Graphene Films by Hydrogen-Free Rapid Thermal Chemical Vapor Deposition. *ACS Nano* **8**, 950-956 (2014).

[7] Sun, J., et al. Low Partial Pressure Chemical Vapour Deposition of Graphene on Copper. *TNANO* **11**, 255-259 (2011).

[8] Li, X., et al., Graphene Films with Large Domain Size by a Two-Step Chemical Vapor Deposition Process. *Nano Lett.* **10**, 4328-4334 (2010).

[9] Suk, J. W., et al. Transfer of CVD-Grown Monolayer Graphene onto Arbitrary Substrates. *ACS Nano* **5**, 6916-6924 (2010).

[10] Cowley, J. M., et al. The structures of some ferric chloride-graphite compounds. *Acta. Cryst.* **9**, 421-431 (1956).

[11] Zhan, D., et al. FeCl3-Based Few-Layer Graphene Intercalation Compounds: Single Linear Dispersion Electronic Band Structure and Strong Charge Transfer Doping. *Adv. Func. Matter.* **20**, 3504-3509 (2010).

[12] Khrapach, I. et al. Novel Highly Conductive and Transparent Graphene?Based Conductors. *Func. Matter.*, **24**, 2844-2849 (2012).

[13] Blake, P. et al. Making graphene visible. *App. Phys. Lett.* **91**, 063124 (2007).

[14] Ferrari, A. C., et al. Raman spectrum of graphene and graphene layers. *Phys. Rev. Lett.* **97**, 187401 (2006).

[15] Craciun, M. F., et al. Trilayer graphene is a semimetal with a gate-tunable band overlap. *Nat. Nanotech.* **4**, 383 (2009).

[16] Lee, D. S., el al. Raman spectra of epitaxial graphene on SiC and of epitaxial graphene transferred to SiO2. *Nano Lett.* **8**, 4320 (2008).

[17] Matlab - Image processing toolbox -http://www.mathworks.co.uk/help/images/image-enhancement-and-analysis.html

Chapter 4

Graphene growth in a cold walled furnace

4.1 Introduction

Large area CVD graphene grown on copper has emerged as the most promising approach for the industrial exploitation of graphene[1, 2]. This is due to the compatibility with existing silicon based processing technologies and high efficiency roll-to-roll production techniques. Furthermore, recent technological advances offer control over the CVD graphene morphology, doping and the fabrication of hetero-structures, which allows for the tailoring of the properties of graphene granting access to emerging and traditional applications,[3, 4, 5].

Tailored CVD graphene is suitable for many applications ranging from transparent and flexible electrodes for solar cells, touch screen and light emitting displays[7, 8, 9, 10] to metrological systems, where fundamental constants can be redefined to unprecedented accuracy[11, 12].

There are many approaches to CVD graphene growth procedures that use different combinations of growth times, gas flow rates and the ratio of growth gases which affect growth rate and control growth morphology. Each method produces different qualities of the resulting graphene film. Quality of a graphene film is gauged by the measured charge carrier mobility, which is affected by grain boundaries, film continuity and doping. To maximise the apparent quality of graphene films it is typical to produce small devices (1μm $\times$ 6μm) to reduce the influence of grain boundaries and film continuity. However, for industrial applications it is necessary to not only have high quality films, but to have this quality throughout the large area of the film produced.

Therefore, to better quantify the quality of graphene films for electronic applications I propose an electronic quality factor (Q). By considering the size of the measured device alongside the charge carrier mobility, the quality of large area films can be

gauged. Comparing the range of produced film qualities listed in Table 4.1, there is a range of measured mobilities from 1800 $cm^2/(V.s)$ to 10800 $cm^2/(V.s)$. When considering the electronic quality, there is a redistribution of the perceived quality of the different growth processes in favour of large devices more suited for commercial applications, shown later in this chapter.

Each growth process also has different associated costs. Long growth times at high temperatures in hot walled tube furnaces has a large energy cost. However, the energy cost is not the only significant cost for graphene production. The price of the high purity copper foils, used as a substrate, and gases required for growth of graphene contribute significantly to the cost of production. To assess the viability of graphene production I estimate the total cost of CVD graphene production for a range of different procedures is summarised in Appendix A.

Table 4.2 and Table 4.3 show the estimated energy and growth gas costs, respectively, for each different growth recipe. The biggest contribution to the total cost of production is the energy cost. Table 4.2 shows the large variation in the energy cost of producing CVD graphene, where the use of a hot walled furnace has a price ranging from £0.52 to as much as £11.00; where long growth times significantly increase production cost. Cold walled systems [19, 16] use significantly less energy, hence have reduced energy and total costs.

Summing the cost of all processes involved us to compare the different approaches of CVD graphene production reported in Table 4.4. To grow higher quality and cheaper graphene the graphene growth process must be understood, allowing for a reduction in the growth time and volume of gases used. However, hot walled furnaces are slow to heat up and cool down ($>$ 40 minutes) due to the large thermal mass, hence obscuring the processes involved with growth and complicating the interpretation of

Article	Mobility ($cm^2/(V.s)$)	L (μm)	W (μm)	Electronic quality factor (Q)
Li et. al.[1] (2009)	4050	3.364	1.16	2.50×10^5
Bae et. al.[2] (2009)	3175	1.16	1	3.60×10^3
Li et. al.[13] (2011)	4000	–	–	–
Liu et. al.[14] (2011)	3600	0.5377	1.1	2.10×10^3
Sun et. al.[15] (2012)	1800	4	2	1.40×10^4
Hao et. al[3] (2013)	10800	3.364	1.16	4.20×10^4
Chen et. al.[4] (2013)	5200	3.899	16.4569	3.30×10^5
Our work (2014)	3300	50	25	4.10×10^6

Table 4.1: Literature data required to make an estimation of the electronic quality factor (Q) for each growth procedure of CVD graphene. The mobility is the field effect mobility ($cm^2/(V.S)$), L is the device length (μm), W is the device width (μm) and the electronic quality factor (Q) ($\mu m^2 \times cm^2/(V.S)$)). The electronic quality factor is rounded to the nearest two significant figures to account for uncertainty in device size.

	Heating up			Anneal and Growth			
Article	Time(hours)	Power(kW)	Cost(£)	Time(hours)	Power(kW)	Cost(£)	Total cost(£)
Li et. al.[1] (2009)	1.000	6.0	0.811 ±	0.50	5.175	0.349	1.20
Bae et. al.[2] (2010)	0.666	6.0	0.540	1.00	5.175	0.700	1.20
Li et. al.[13] (2011)	0.666	6.0	0.540	1.50	5.175	1.049	1.60
Liu et. al.[14] (2011)	0.167	6.0	0.135	0.55	5.175	0.384	0.52
Sun et. al.[15] (2012)	–	–	–	0.22	0.700	0.021	0.021
Hao et. al[3] (2013)	0.666	6.0	0.540	15.08	5.175	10.551	11.00
Chen et. al.[4] (2013)	0.666	6.0	0.540	6.30	5.175	4.408	4.90
Our work (2014)	0.050	0.3	0.002	0.26	0.195	0.007	0.009

Table 4.2: Energy consumption of each CVD graphene growth procedure, broken down into the heating of the foils and the annealing and growth process. Total cost is rounded to the nearest two significant figures to account for uncertainty in growth times and fluctuating costs.

	Hydrogen		Methane		Argon		
Article	Volume(m^3)	Cost(£)	Volume(m^3)	Cost(£)	Volume(m^3)	Cost(£)	Total cost(£)
Li et. al.[1] (2011)	2.6×10^{-4}	0.0081	4.5×10^{-5}	0.0040	–	–	0.012
Bae et. al.[2] (2010)	1.1×10^{-3}	0.0351	1.05×10^{-3}	0.0934	–	–	0.13
Li et. al.[13] (2011)	3.2×10^{-4}	0.0102	2.8×10^{-3}	0.2491	–	–	0.26
Liu et. al.[14] (2011)	4.3×10^{-4}	0.0130	1.6×10^{-5}	0.0150	1.54×10^{-2}	0.4940	0.52
Sun et. al.[15] (2012)	3.3×10^{-4}	0.0104	1.5×10^{-4}	0.0048*	1.66×10^{-2}	0.5334	0.55
Hao et. al[3] (2013)	9.8×10^{-3}	0.3059	8.3×10^{-4}	0.0738	–	–	0.38
Chen et. al.[4] (2013)	3.9×10^{-3}	0.1220	5.85×10^{-5}	0.1186	–	–	0.24
Our work (2014)	7.5×10^{-6}	0.0002	3.59×10^{-5}	0.0031	–	–	0.0033

Table 4.3: Gas consumption for several CVD graphene growth studies, for the estimation of the total cost of graphene growth gases. *The cost for methane has been replaced with that of argon, as argon diluted methane was used. The total cost is rounded to the nearest two significant figures to account for uncertainty in gas flow times.

	Cost (£)			
Article	Gas cost	Energy cost	Copper cost	Total cost
Li et. al.[1] (2009)	0.26	1.20	0.35	1.80
Bae et. al.[2] (2009)	0.13	1.20	0.35	1.70
Li et. al.[13] (2011)	0.012	1.60	0.35	1.90
Liu et. al.[14] (2011)	0.52	0.52	0.35	1.40
Sun et. al.[15] (2012)	0.55	0.021	0.35	0.92
Hao et. al[3] (2013)	0.38	11.00	0.35	11.00
Chen et. al.[4] (2013)	0.24	4.90	0.35	5.40
Our work (2014)	0.0033	0.009	0.35	0.36

Table 4.4: The estimation of cost of each price component and the total cost of the growth for each procedure in GBP (£). The total cost is rounded to the nearest two significant figures.

results. Furthermore, hot walled furnaces are inefficient for achieving and maintaining growth temperatures, leading to a high energy cost, as shown in Table 4.2[3, 4]. In contrast, a resistively heated cold walled system, by the fact that only a small volume is heated, can be heated and cooled rapidly (< 4 minutes). This allows for observation of the graphene growth required for the optimisation of the growth process. Additionally, cold walled furnaces offer an energy efficient alternative to hot walled systems. For example, a commercial cold walled furnace has a power draw of 0.3 kW[22] compared to the MTI 1200X hot walled furnace with a power draw of 6 kW. In the following sections, I present my approach to optimising the growth of CVD graphene using cold walled system, by characterising the growth process with the aim to reduce the price while keeping the quality of the product high. I then asses the electronic quality and cost of production, which is then compared to the approaches discussed earlier in this section.

4.2 Experimental details

Graphene islands are obtained using a commercial cold walled CVD system. Copper foils are heated to 1035°C in a low pressure hydrogen (H_2) atmosphere and annealed for 10 minutes to increase the copper grain size and clean the copper surface of oxides. Graphene growth is then initiated by introducing methane (CH_4) as a carbon source. To understand the initial stages of graphene formation, growths are carried out for a range of temperatures (950°C - 1035°C) and growth times (10 seconds - 600 seconds). After the growth, the methane gas flow is stopped and the foils are rapidly cooled to room temperature. The films are transferred from the copper foils to SiO_2/Si substrates for characterisation, using the wet etch technique described in Section 3.2.3. I characterise the films using Raman spectroscopy, atomic force microscopy (AFM) and scanning electron microscopy (SEM).

4.3 Initial stages of the growth of graphene

For all investigated growth temperatures (T_G), a thick disordered carbon film is observed, which forms in the early stages of growth, illustrated in Figure 4.4. As the growth time is extended, the film progressively becomes thinner and finally evolves into graphene islands.

4.3.1 Raman spectroscopy study

To track the transition from a disordered carbon film to graphene I first use Raman spectroscopy. Figure 4.1 shows a waterfall plot of the Raman spectra for growths at 950°C and growth times (t_G) ranging from 1 minute to 6 minutes. I observe peaks

characteristic of sp^2 bonded carbon atoms for all measured samples. From lowest to highest Raman Stokes shift the peaks are: the D peak at ≈1340 cm^{-1}, the G peak at ≈ 1600 cm^{-1}, the D' peak at ≈ 1600cm^{-1}, and the 2D peak at ≈ 2700cm^{-1}.

Lorentzian fitting of D, G and 2D peaks allows for the determination of the degree of ordering in the film, by analysing the relative band intensities taken from the peak maximum ($I_{D,G,2D}$), the Full Width at Half Maximum (FWHM(D,G,2D)), and the peak position $\widetilde{\nu_G}$. According to the three stage model for the classification of disorder, the evolution of I_D/I_G, FWHM (D,G,2D) and $\widetilde{\nu_G}$ allows us to asses the ordering/amorphisation in carbon materials, from graphite and amorphous carbon[23, 24] to few layer and monolayer graphene[25, 26].

For $t_G = 1$ minute, nano-crystalline graphene is observed. This is evidenced by the small intensity of the 2D peak with respect to the D and G peak intensities, together with the overlap between the G and D' peaks, which indicates that there is no significant long range two dimensional ordering. Furthermore, the absence of a doublet structure of the D and 2D peaks suggests that there is no three dimensional ordering.

Increasing t_G, there is an observed increase in I_{2D} and I_G, as shown in Figure 4.2a, combined with a decrease in the ratio I_D/I_G from 3.9 to 0.2, as seen in Figure 4.2b. Simultaneously, $\widetilde{\nu_G}$ downshifts from 1601 cm^{-1} to 1590 cm^{-1} and there is a significant reduction of FWHM(D,G,2D), as shown in Figure 4.2c and d. The evolution of $I_{G,2D}$, I_D/I_G, $\widetilde{\nu_G}$ and FWHM(D,G,2D) with increasing t_G is consistent with the stage 1 long range two dimensional ordering trajectory leading from nano-crystalline graphene to graphene, as described in Section 2.5.1. In this regime, the increase in two dimensional long range ordering increases the size of the sp^2 bonded clusters / domains (L_a). Cluster size can be estimated using the empirical Tuinstra-Koenig relation[27], expressed by Equation 4.1, where C(532nm) = 4.96nm. C is an empirically derived

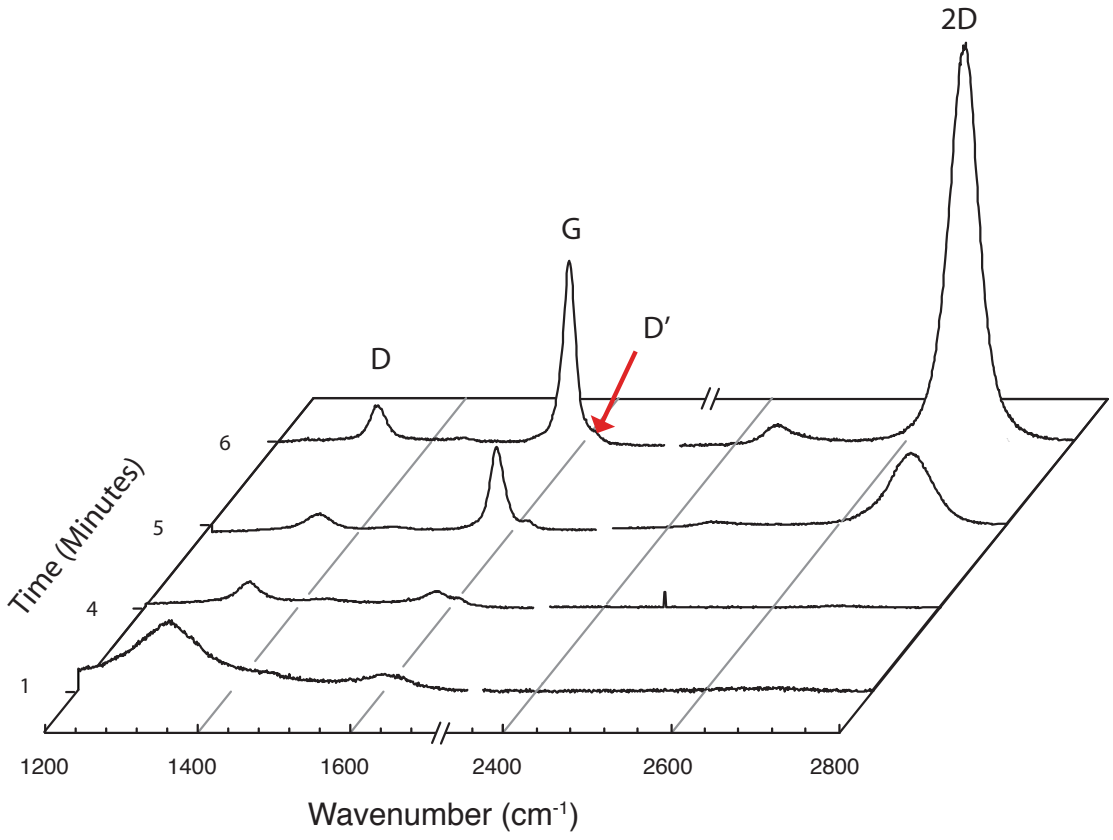

Figure 4.1: A waterfall plot showing Raman spectra for films grown at 950°C, transferred to SiO_2/Si with an excitation wavelength of 532nm. Raman spectra are normalised to the intensity of the Si Raman peak at 521cm^{-1} and are presented with ascending time, from 1 to 6 minutes. The peaks are identified from left to right as the D peak, the G peak, the D' peak, and the 2D peak.

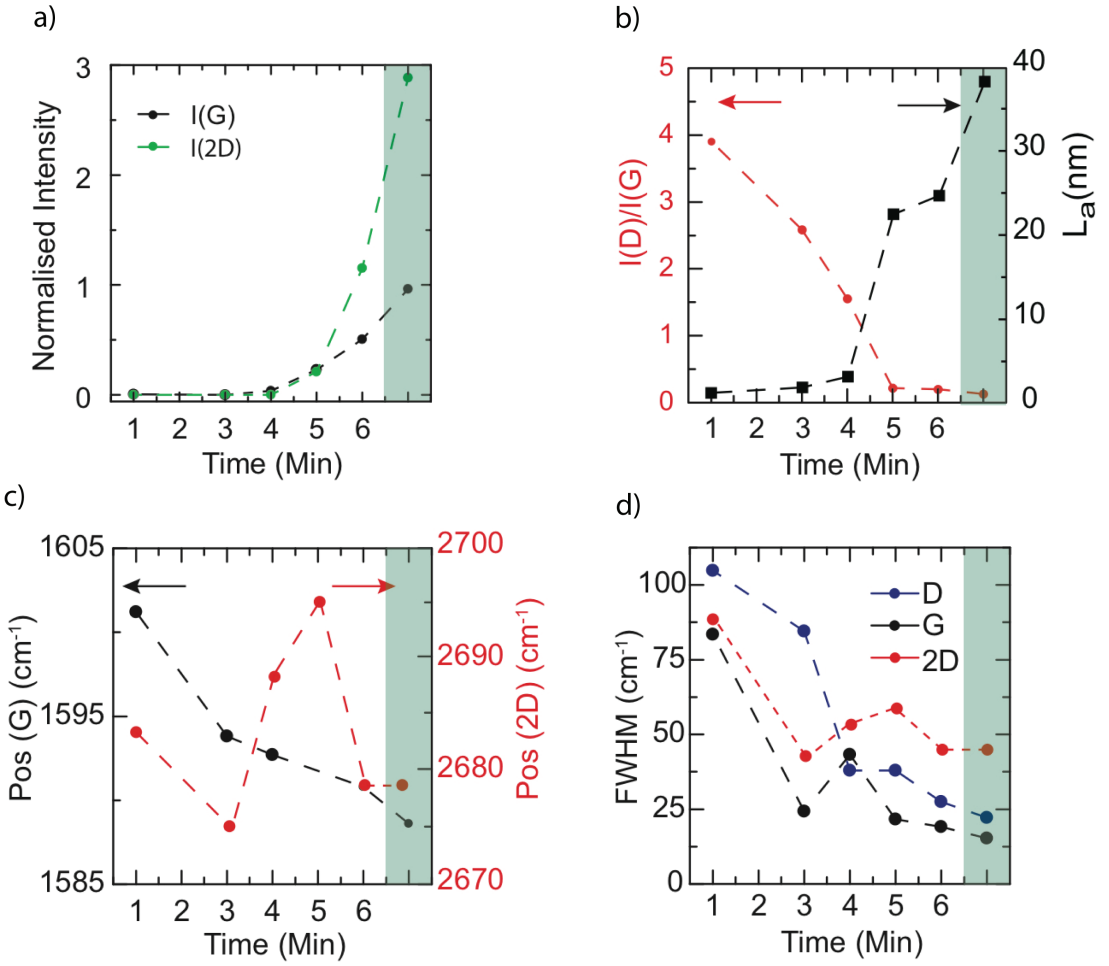

Figure 4.2: Fitted parameters plotted with respect to time for a growth temperature T_G = 950°C; each point is representative of a typical carbon film for each time. a) The intensity of the G and 2D peaks (I_G and I_{2D}), b) the peak maximum of the D peak divided by the G peak (I_D/I_G), left, and the estimated domain size from the Tuinstra-Koenig relation, right, c) the position of the G $\widetilde{\nu_G}$ and 2D peaks $\widetilde{\nu_{2D}}$, d) the FWHM of the D, G and 2D peaks, FWHM(D,G,2D). The highlighted regions show the relevant fitted parameters from a continuous graphene film produced using the two stage growth process. The dashed lines are a guide for the eye and the experimental errors are smaller than the data points used on the plot

number associated with the D peak and depends on the wavelength of the excitation laser[28]. Using this relation, L_a is estimated with respect to the growth time, as shown in Figure 4.2b. The observed domain size increases from 2nm for t_G = 1 minute to 25nm for t_G = 6 minutes.

$$L_a = \frac{C(\lambda)}{I_D/I_G} \tag{4.1}$$

For growth times above 6 minutes, the 2D peak has an intensity more than twice that of the G peak and can be fitted with a single Lorentzian, with $\widetilde{\nu_{2D}}$ = 2678 cm^{-1} and FWHM(2D) = 44.7 cm^{-1}. These findings are consistent with the formation of monolayer graphene[26, 25, 29].

When the growth temperature is increased to T_G = 1000°C and 1035°C, there is a similar behaviour, however, the transition occurs in a much shorter timeframe. Figure 4.3a and b show the evolution of the Raman spectra for 1000°C and 1035°C. After 5 seconds and 1 second, there is no long range two dimensional ordering and no three dimensional ordering for 1000°C and 1035°C respectively. This is evidenced by the low intensity 2D peak with respect to the D and G peaks and a lack of doublet structure of the D and 2D bands. After 10 seconds for both temperatures, I observe the same evolution of the peak characteristics, an increase in I_{2D} and I_G, a decrease in I_D/I_G, and an increasing separation of the G and D' peaks. This is also consistent with a stage 1 ordering trajectory, as with t_G = 950°C. After 40 seconds and 20 seconds respectively for 1000°C and 1035°C, I observe the Raman spectra of monolayer graphene.

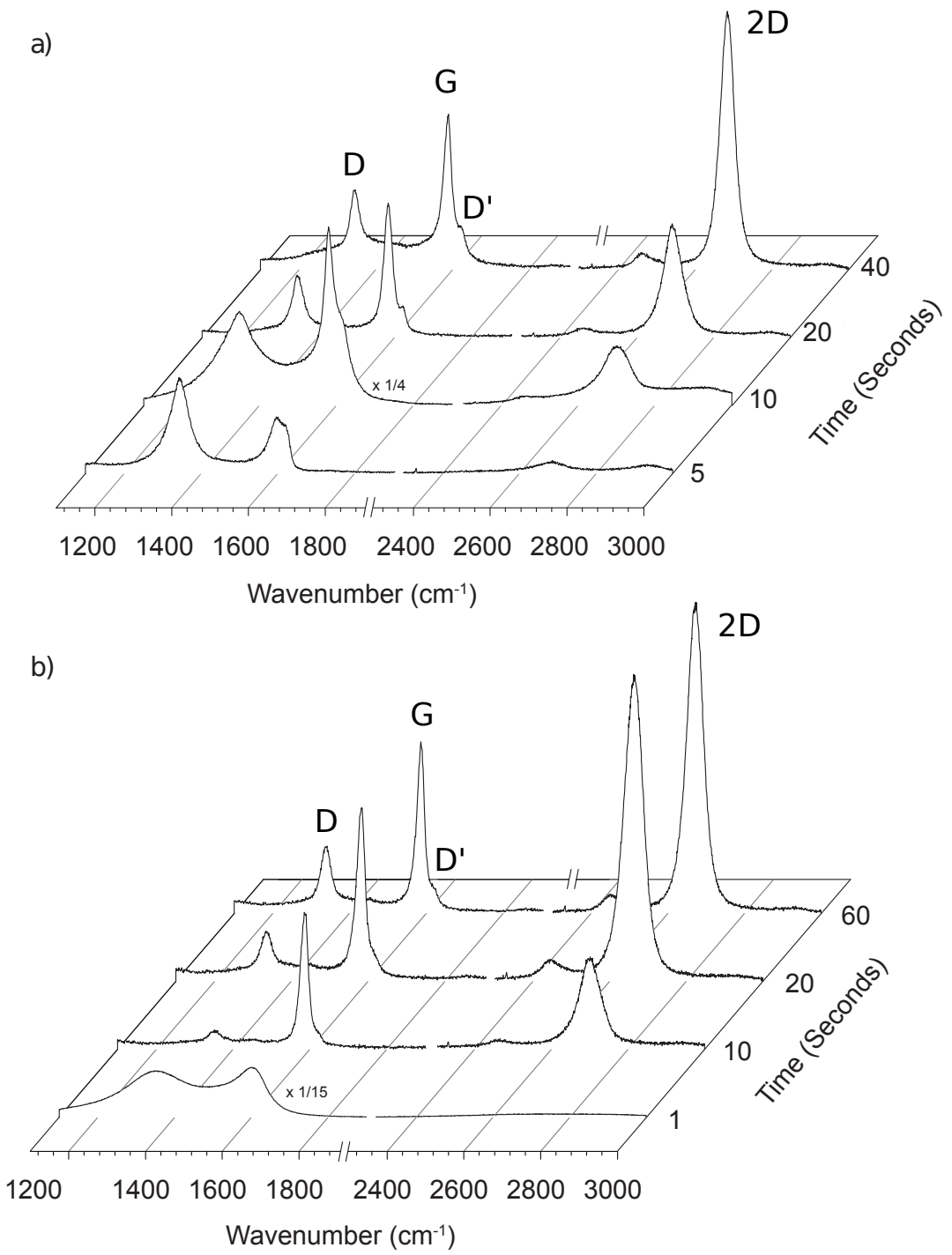

Figure 4.3: A waterfall plot showing Raman spectra of graphene transferred to SiO_2/Si, and with an excitation wavelength of 532nm. Raman spectra at 521cm^{-1} are normalised to the intensity of the Si Raman peak and are presented for a growth temperature T_G of a) 1000°C and growth time t_G ranged from 5 to 40 seconds, b) 1035°C and growth time t_G ranged from 1 to 60 seconds.

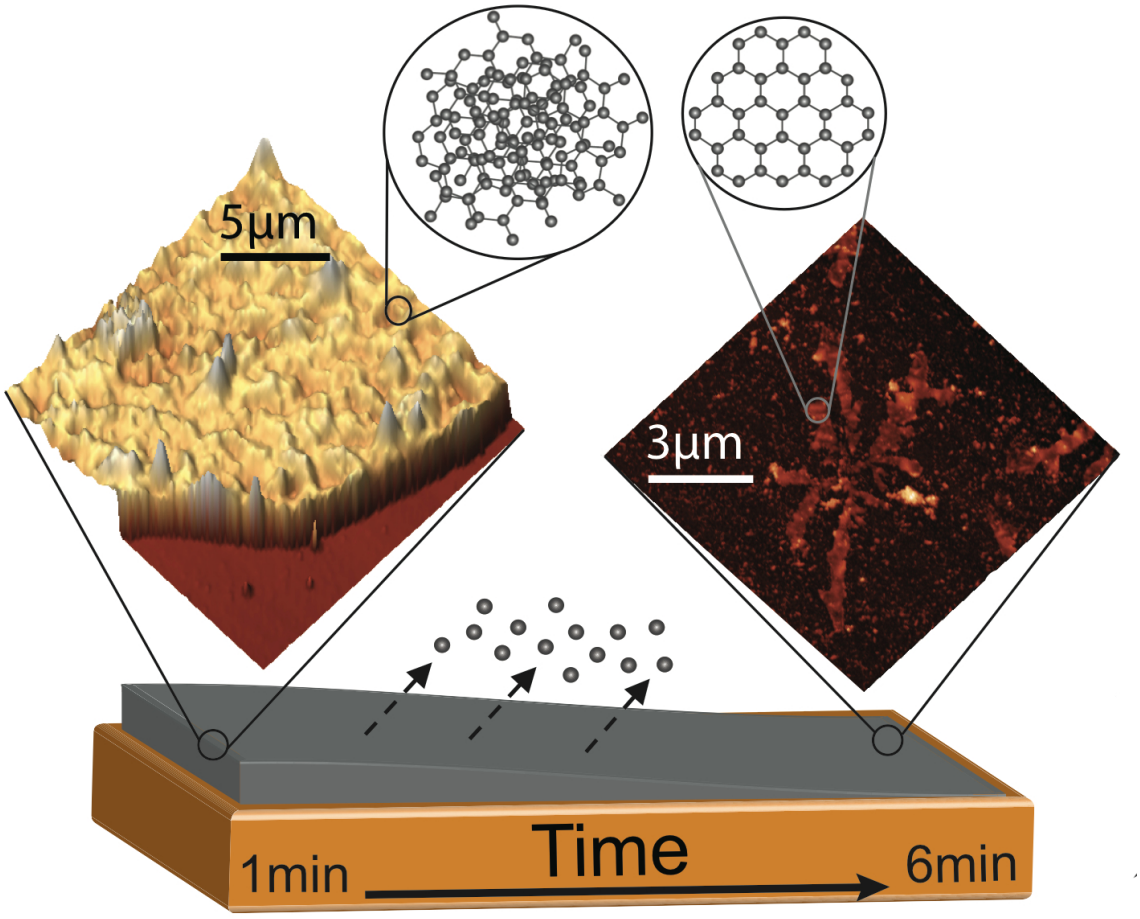

Figure 4.4: Illlustration of a carbon film as it converts from a disordered structure into graphene islands at T_G = 950°C. The inset, left, shows the AFM topography of a thick carbon film after 1 minute of growth, with the disordered structure highlighted. The inset, right, shows the AFM topography of a graphene island, with the structure highlighted, after 6 minutes.

4.3.2 AFM study of film thickness

To understand the process of graphene formation the film thickness changes with respect to growth time (t_G) are observed. As the Raman study alludes, the formation of graphene occurs for all growth temperatures (T_G), however, I focused my attention to the slowest growth rate to gain better temporal resolution, which occurs at T_G = 950°C, as shown in Figure 4.4 .

Sample thickness was measured using the AFM technique described in Section 3.5.4. Figure 4.5 shows that t_G=1 minute, the film thickness is 115nm, and it reduces as the growth time (t_G) is increased. A thickness of 2.7nm is observed after 6 minutes, and, accounting for fabrication residues and substrate effects, is representative of monolayer graphene[30]. It is observed that the carbon film is continuous during the initial stages of nano-crystalline graphene formation. As the film thickness is reduced, the composition tends to graphene. After 4 minutes, the film fragments into graphene islands, as shown in Figure 4.4.

This evidence, supported by the evolution of the Raman spectra as a function of t_G, suggests that the disordered carbons are desorbed during growth, eventually resulting in monolayer graphene, which is stable at the growth temperatures.

4.3.3 SEM study of island growth

SEM is used to provide further insight into the growth of the graphene islands after the fragmentation of the carbon film. The high contrast between the graphene islands (dark) and the insulating SiO_2/Si substrate (light) allows us to use a simple counting algorithm, described in Section 3.5.5, to extract information about the size and separation of the graphene islands. Figure 4.6 shows the evolution from a continuous film

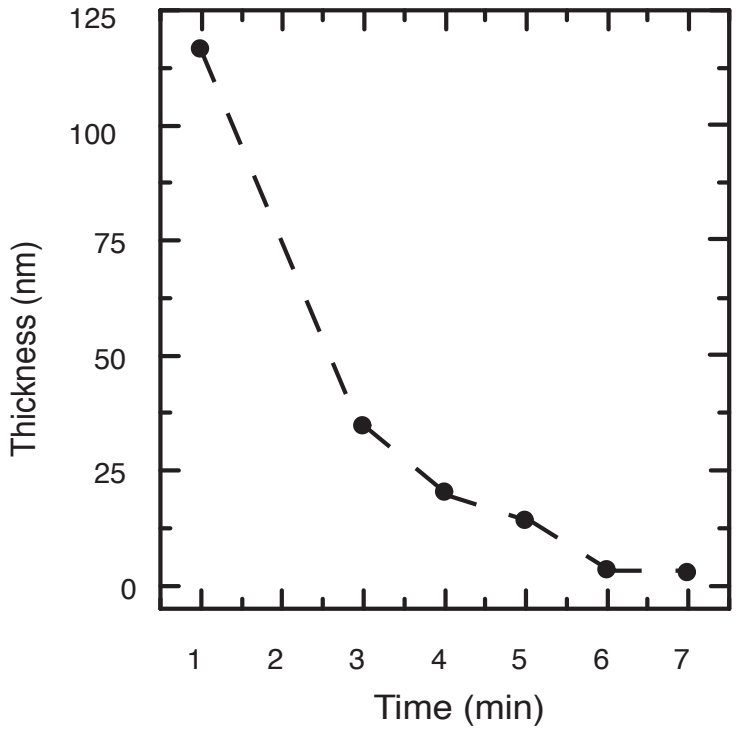

Figure 4.5: CVD film thickness plotted against the growth time t_G for transferred films grown at $T_G = 950$°C. The dashed line is a guide for the eye and the experimental error bars are smaller than the data points.

to fragmented graphene islands over t_G at $T_G = 950°C$.

A continuous film at $t_G = 1$ minute is observed. After 3 minutes, the film starts to fragment. Further increasing the growth time t_G to 4 minutes leads to full fragmentation. At this point, the change in the island size and separation is tracked with increasing growth time t_G.

Figure 4.7 shows the island size plotted against the growth time for a range of growth temperatures. For growth times between 5 and 7 minutes, for $T_G = 950°C$, there is an increase in island size with growth time. The maximum island size is achieved at $t_G = 7$ minutes; however, after 7 minutes the size of the islands begins to reduce. A similar behaviour is observed for $T_G = 1000°C$ and 1035°C, but on a shorter timescale. These observations show that increasing growth temperature accelerates the formation of graphene islands and the achievement of maximum island size.

As discussed in the previous Chapter 3.2, increasing growth time would not lead to a continuous film. The average separation of the forming graphene islands is also tracked. Post film fragmentation, the average separation for all growth temperatures is seen to increase with increasing growth time, as shown in Figure 4.8. There is a saturation in graphene island separation after 9 minutes for $T_G = 950°C$, and 2 minutes for $T_G = 1000°C$ and 1035°C. A saturation in the separation of graphene islands is observed, by a significant reduction in the rate of change of separation, indicates is that there are no new islands formed after the initial fragmentation.

4.4 Growth of continuous graphene film

Grown graphene islands can be connected using a two stage growth process [31]. This is achieved by increasing the ratio of methane to hydrogen after the graphene islands

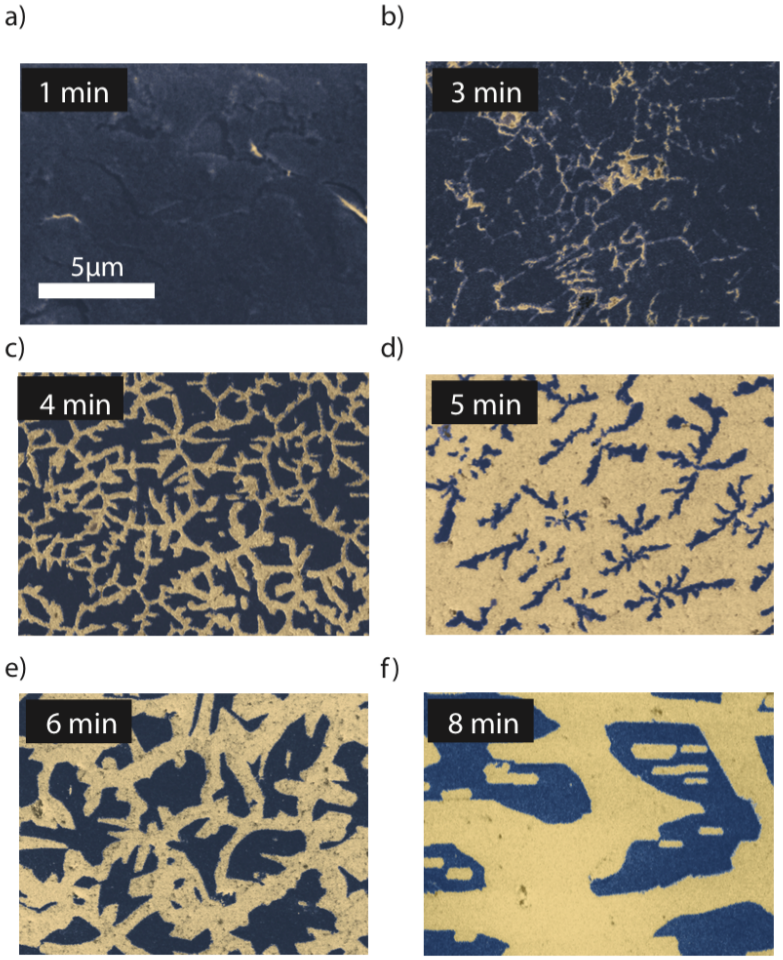

Figure 4.6: Scanning electron micrographs of transferred films, grown at $T_G = 950°C$, for growth times t_G of a) 1 minute, b) 3 minutes, c) 4 minutes, d) 5 minutes, e) 6 minutes, and f) 8 minutes. All images are in scale.

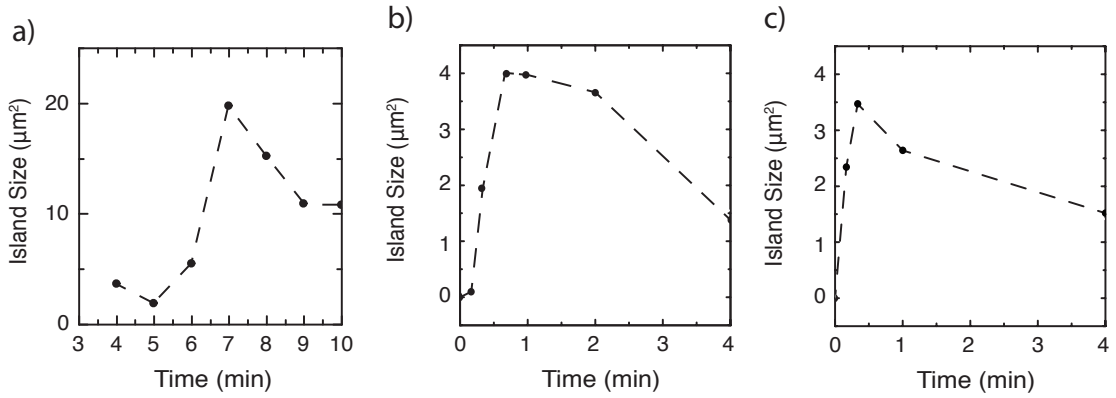

Figure 4.7: The average island size of grown graphene islands, determined from SEM, with respect to growth time t_G for growth temperatures T_G of a) 950°C, b) 1000°C and c) 1035°C.

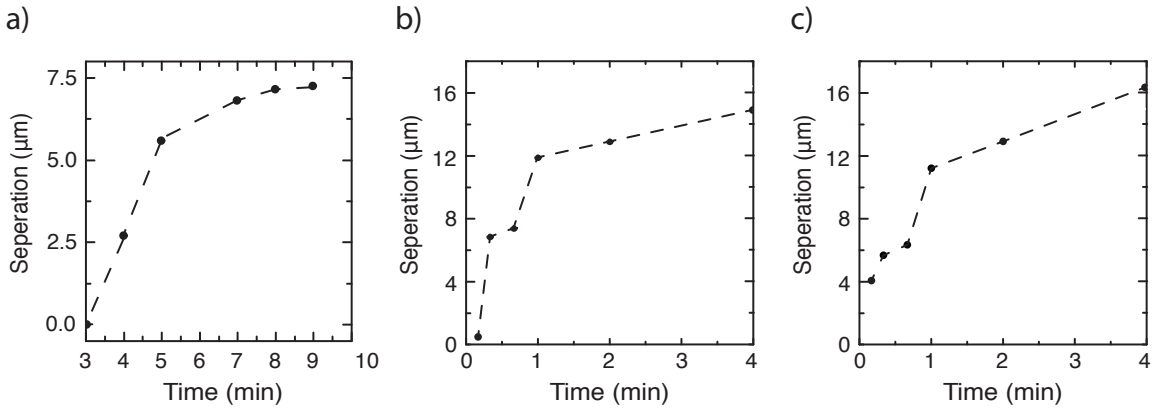

Figure 4.8: The average island separation of grown graphene islands, determined from SEM, with respect to growth time t_G for growth temperatures T_G of a) 950°C, b) 1000°C and c) 1035°C.

are formed. It has been demonstrated that changing the pressure, growth gas ratio and an extended growth time does not generate new islands, while causing the growth of existing islands. The islands then grow until they coalesce into a continuous film.

To maximise the quality of CVD graphene produced, the size of the graphene islands needs to be maximised, so that during coalescence there is a reduced number of grain boundaries. The criterion for this is to have large graphene islands with a large separation. However, to reduce the cost of production total growth time required to form a film of graphene needs to be minimised.

As a compromise between quality and cost of production, I select a growth temperature of $T_G = 1000°C$ and a growth time of $t_G = 40$ seconds. This accounts for a maximum in island size, a large separation, and a short time required to grow the graphene islands, reducing the total energy costs. To fill the gaps between the graphene islands on the copper foil, I change the hydrogen/methane ratio from 2:7 to 2:35. I grow graphene with this new ratio of gases for 5 minutes, stop all growth gases and cool the copper foil to room temperature.

4.5 The electronic quality of graphene films grown by cold wall CVD

Using cryogenic electrical transport measurements the quality of the graphene film is determined to prove that the graphene produced is monolayer. First I transfer the grown film to a SiO_2/Si substrate. I create an electrically connected Hall bar, with the dimensions of 225 μm $\times$ 25 μm, using electron beam lithography, as described in Section 3.3.

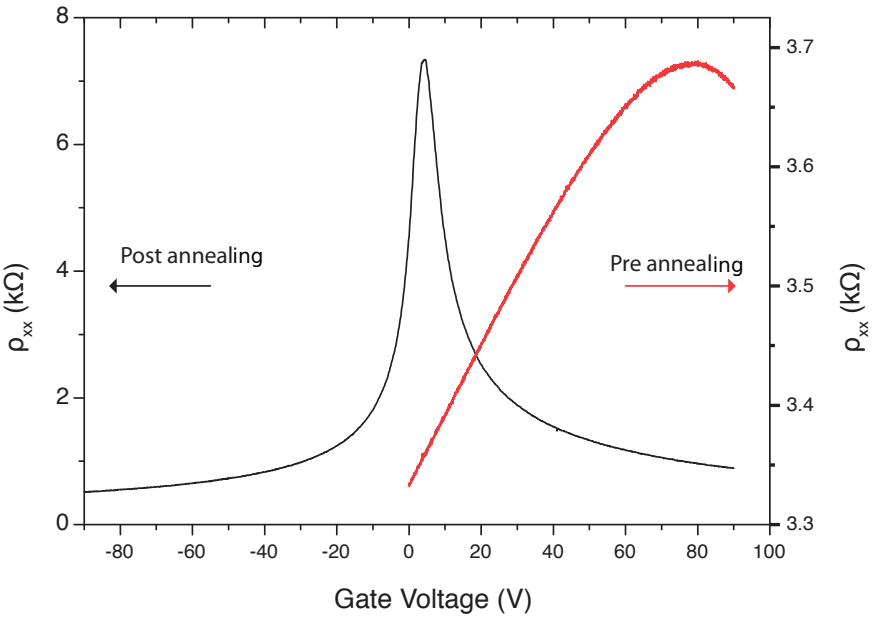

Figure 4.9: The four terminal resistivity (ρ_{xx}) plotted against applied backgate voltage and measured at a temperature of 4.2K. The red curve is obtained before the annealing procedure and the black curve is obtained after the annealing procedure.

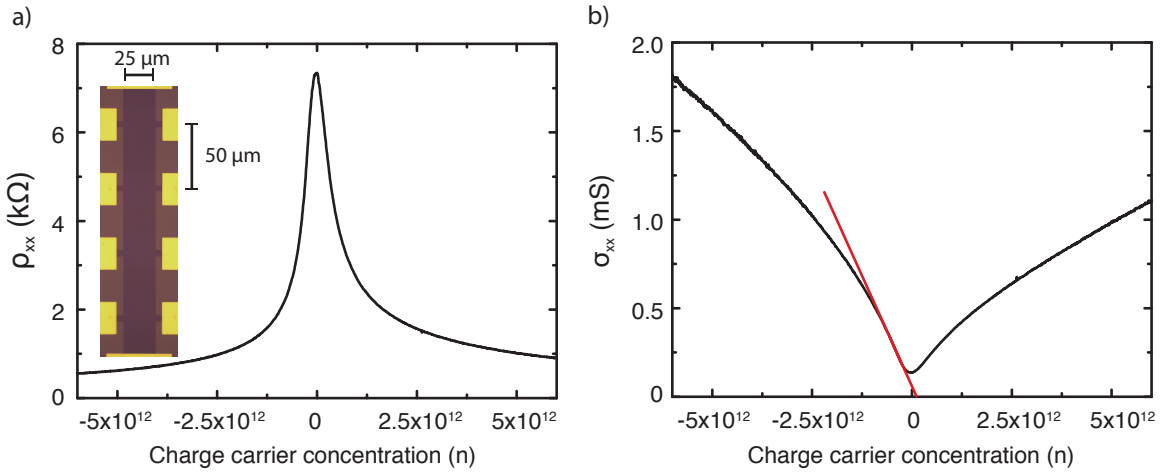

Figure 4.10: a) The measured four terminal longitudinal resistivity (ρ_{xx}) plotted with respect to the charge carrier concentration (n) at a temperature of 4.2K. The inset shows the dimensions of the measured device on a false colour image, b) the longitudinal conductivity (σ_{xx}) plotted with respect to the charge carrier concentration (n). The linear gradient (red) shows the region where the charge carrier mobility is estimated.

The initial measurement of the resistivity versus gate voltage shows that the charge neutrality point (CNP) occurs at $V_g = +80$V, indicating that the sample is doped by fabrication residues. To clean the graphene Hall bar of fabrication residues, I thermally anneal the device at 140°C in the top of a helium dewar. After 12 hours of annealing, there is a shift in the CNP from $\approx +80$V to 4V, as shown in Figure 4.9. To determine the charge carrier mobility, the longitudinal resistivity (ρ_{xx}) is measured with respect to the charge carrier concentration (n). By plotting the conductivity against charge carrier concentration and taking the gradient for low charge carrier concentration, the charge carrier mobility is estimated. Several devices were measured and had a typical mobility of ≈ 3000 cm^2/ (V.s) .In the shown sample, the estimated maximum carrier mobility is 3300 cm^2/ (V.s). From this value, the estimated electronic quality factor for the sample is 4.13×10^6.

It is proved that the grown graphene is monolayer by measuring the response of the longitudinal and Hall resistivity at high perpendicular magnetic field. The measurements are performed using a constant current of 1nA, as described in Section 3.5.3. At a perpendicular field of 13T and a temperature of 250mK, the Hall conductance is measured with respect to the applied gate voltage, and results as shown Figure 4.11.

It is observed that there are well developed conductance plateau when the Fermi energy is within a Landau level with values that correspond to the conductance relationship $\sigma_{xy} = (n + 1/2) \times 4e^2/h$. As described in Section 2.2.3, this is characteristic of the half integer quantum Hall effect[32, 33]. The four fold degeneracy in the quantised conductance is a signature of monolayer graphene, with two fold spin and valley degeneracy. Simultaneously, I observe $\rho_{xx} = 0\Omega$, where the Fermi energy is within the n = 0 Landau level for both electrons and holes; as seen in Figure 4.12. The fact that there are observed localised and extended states in the quantum Hall regime for both electrons and holes at relatively low magnetic fields indicates that the grown graphene is of high quality over a large area.

Plotting a colour map of the differential Hall conductance, Figure 4.13, shows that there are bands, which represent the Landau levels. These quantum Hall features are observed, specifically for n = 0, down to fields of 5T, further highlighting the high quality of the CVD graphene produced.

4.6 Estimation of the cost of graphene production

Having established that high quality graphene can be grown by cold wall CVD, I proceed now to estimate the cost of production.

For the growth process, the copper foil is annealed for 10 minutes at 1035°C with

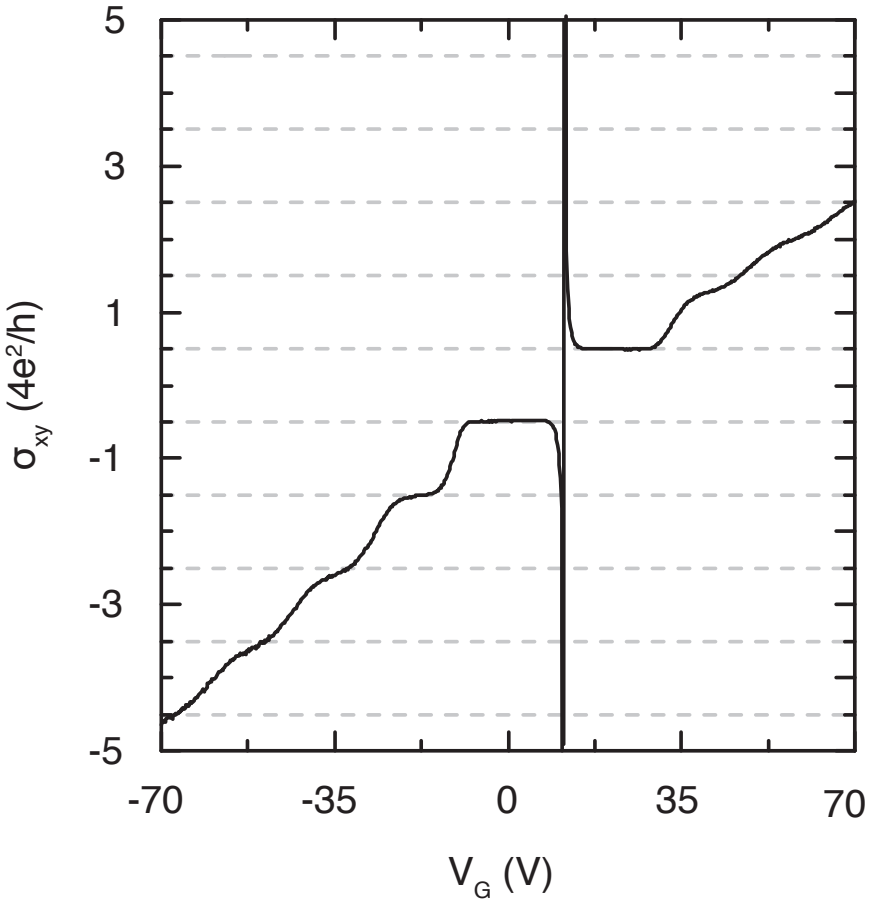

Figure 4.11: The Hall conductance (σ_{xy}), normalised to ($4e^2/h$), plotted against the applied gate voltage (V_g) at a temperature of 250mK with a perpendicular magnetic field of 13T. The dashed lines represent the half integer steps corresponding to the relationship $\sigma_{xy} = (n + 1/2) \times 4e^2/h$.

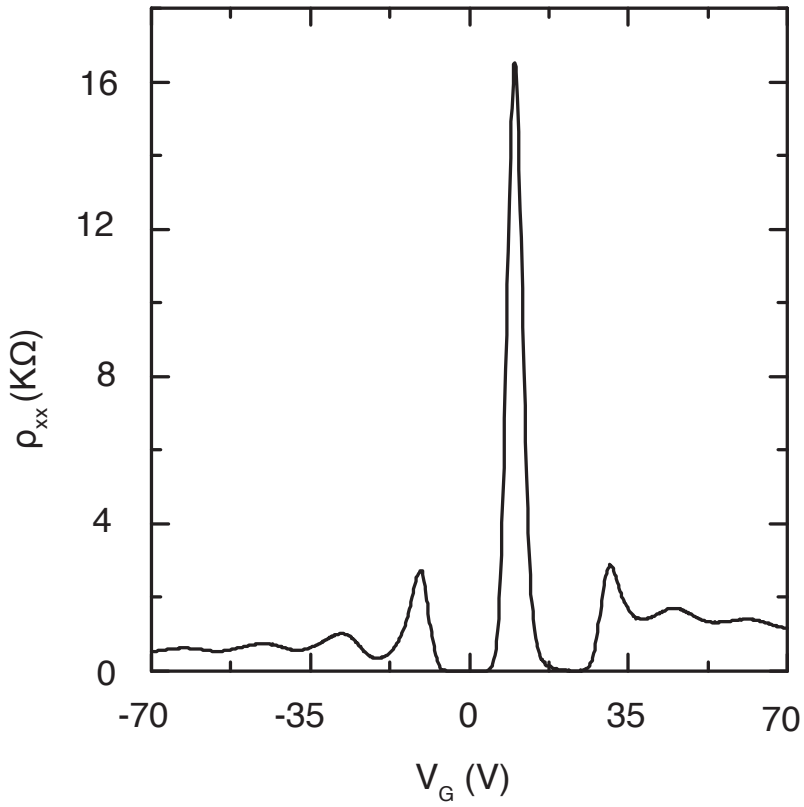

Figure 4.12: The four terminal longitudinal resistivity (ρ_{xx}) plotted against the applied gate voltage (V_g), measured at a temperature of 250mK with a perpendicular magnetic field of 13T.

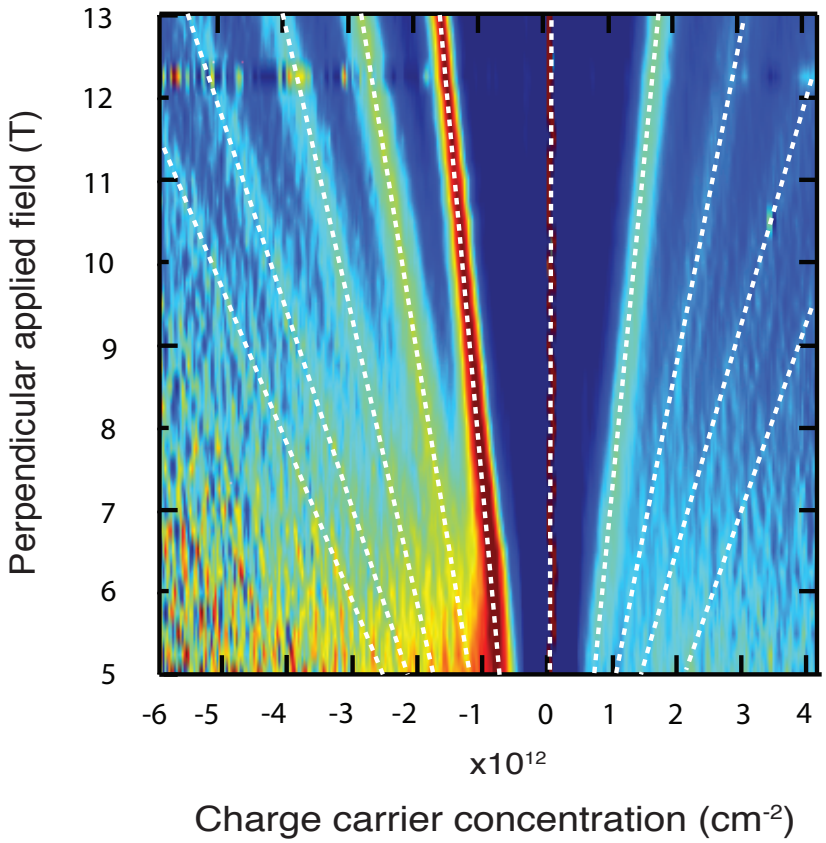

Figure 4.13: A colour map showing the differential Hall conductance at a temperature of 250mK for a range of applied magnetic fields from 5 to 13T and charge carrier concentration (n) ranging from -6×10^{12} to 4.1×10^{12} cm^{-2}. The dashed lines indicate the Landau levels.

a flow rate of hydrogen gas of 0.4 SCCM. The island forming stage is performed at 1000°C for 40 seconds with a flow rate of 0.4 SCCM and 1.4 SCCM of hydrogen and methane respectively. Finally the growth stage is performed at 1000°C for 300 seconds with a gas flow rate of 0.4 SCCM and 7 SCCM for hydrogen and methane respectively, as shown in Table 4.2 and Table 4.3 . The total cost of the whole process is summarised in Table 4.4.

I then compare the cold walled CVD process to the processes presented at the beginning of this chapter. Figure 4.14 shows the electronic quality factor plotted against the cost of production. In this graph, the ideal graphene would have a low production cost and high electronic quality factor. It is apparent that the quality of my produced graphene in this work exceeds that of graphene from other processes, while simultaneously having a significantly lower cost of production. However, there is a different issue in the comparison to the hot walled processes. I have reduced the cost of energy and growth gases to the point where the total cost of our process is dominated by the cost of the copper foil substrate. Fortunately, the copper foil can be reconstituted from the etchant solution to reclaim up to 99% of the original copper in the foil [17]. If the majority of the copper could be reclaimed, the cost of the copper foil can be effectively neglected. The resulting cost of production would reduce by 98.83%-99.89% when compared to the cost of other processes presented at the beginning of this chapter.

4.7 Conclusion

In this chapter, a cold walled furnace is used to optimise the process of growing high quality CVD graphene. Firstly, I characterise the transition from an adsorbed disordered carbon film to monolayer graphene islands, through tracking the increase of two

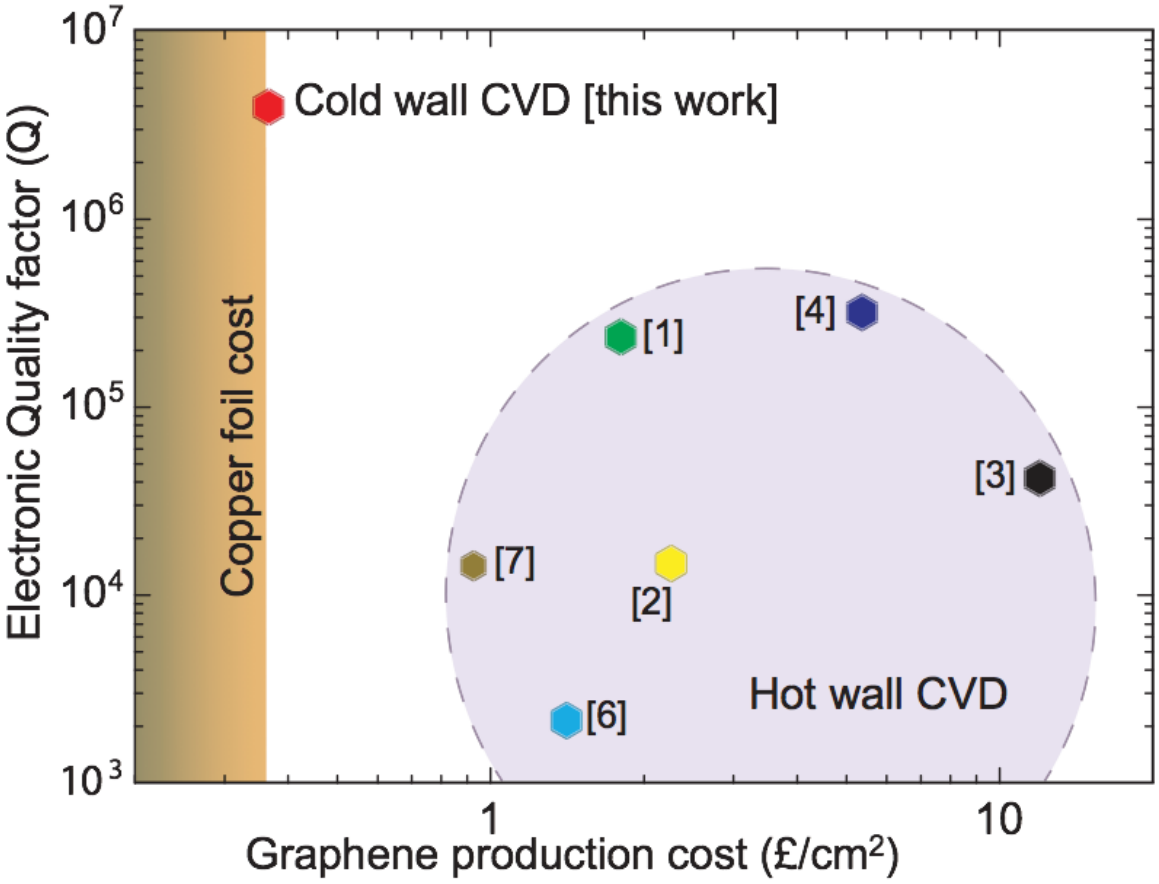

Figure 4.14: A plot comparing the electronic quality factor (Q) to the cost of graphene production, where our work has been included.

dimensional ordering using Raman spectroscopy. Secondly, I determine the change in the thickness of the carbon film until monolayer graphene is observed. Drawing on this information from the Raman and AFM studies, I observe that the increase in growth temperature leads to a reduction in the time required to grow graphene islands. I then track the growth and separation of the grown islands using SEM, which ultimately give me the information required to optimise our growth process. I then determine the quality of the grown graphene using the electronic transport techniques, where I extract a charge carrier mobility of 3300 $cm^2/(V.s)$ and an electronic quality factor (Q) of 4.13×10^6. Finally, I demonstrate that the new process produces high quality graphene, while reducing the cost of producing CVD graphene as much as 99.89%.

Bibliography

[1] Li, X., et al. Large-area synthesis of high-quality and uniform graphene films on copper foils. *Science* **324**, 1312-1314 (2009).

[2] Bae, S., et al. Roll-to-roll production of 30-inch graphene films for transparent electrodes. *Nature Nanotech.* **5**, 574-578 (2010).

[3] Hao, Y., et al. The role of surface oxygen in the growth of large single-crystal graphed on copper. *Science* **342**, 720-723 (2013).

[4] Chen, S., et al. Millimeter-size crystal graphene by suppressing evaporative loss of Cu during low pressure chemical vapor deposition. *Adv. Matt.* **25**, 2062-2065 (2013).

[5] Gan, L., et al. Turning off hydrogen to realise seeded growth of subcentimeter single-crystal graphene grains on copper. *ACS Nano.* **7**, 9480-9488 (2013).

[6] Khrapach, I., et al. Novel Highly Conductive and Transparent Graphene-Based Conductors. *Adv. Matt.* **24**, 2844-2849 (2012).

[7] Kim, H., et al. Organic solar cells using CVD-grown graphene electrodes. *Nanotechnology* **25**, 014012 (2013)

[8] Hecht, D. S., et al. Emerging Transparent Electrodes Based on Thin Films of Carbon Nanotubes, Graphene, and Metallic Nanostructures. *Adv. Matt.* **23**, 1482-1513 (2011).

[9] Chun, S., et al. A flexible graphene touch sensor in the general human touch range. *App. Phys. Lett.*, **2014**, *105*, 041907 (2014).

[10] Ryu, J., et al. Fast Synthesis of High-Performance Graphene Films by Hydrogen-Free Rapid Thermal Chemical Vapor Deposition. *ACS Nano*, **2014**, *8*, 950-956.

[11] Giesbers, A. J. M., et al. Quantum resistance metrology in graphene, *App. Phys. Lett.* **93**, 222109 (2008)

[12] Kyle, J. R., et al. Industrial graphene metrology, *Nanoscale* **4**, 3807-3819 (2012).

[13] Li, X., et. al. Lare-area graphene single crystals grown by low-pressure chemical vapor deposition of methane on copper. *J. Am. Chem. Soc.* textbf133, 2816-2819 (2011).

[14] Liu, W., et al. Synthesis of high-quality monolayer and bilayer graphene on copper using chemical vapor deposition. *Carbon* **49**, 4122-4130 (2011).

[15] Sun, J., et. al. Low partial pressure chemical vapor deposition of graphene on copper. *TNANO* **11**, 255-260 (2012).

[16] Bointon, T. H., et al. High Quality Monolayer Graphene Synthesized by Resistive Heating Cold Wall Chemical Vapor Deposition. *Adv. Mater.* **Early Access**, (2015) doi:10.1002/adma.201501600.

[17] The cost for 2.5cm x 100cm of 99.999% pure 25 μm thick copper from Alfa Aesar - http://www.alfa.com/en/catalog/10950

[18] Specifications taken from MTI website for MTI 1200X - 5L split tube furnace - http://www.mtixtl.com - Dec 2013

[19] Specifications taken from AXITRON website for Black magic II - http://www.aixtron.com/en/products/technologies/ - Dec 2013

[20] Energy saving trust estimation of average electricity cost in the uk - http://www.energysavingtrust.org.uk/Energy-Saving-Trust/Our-calculations - Dec 2013

[21] Costs and Volumes taken from BOC LTD website- http://www.Boconline.co.uk - Dec 2013

[22] Specifications taken from Moorfield website for the NanoCVD-8G - http://www.moorfield.co.uk/ - Dec 2013

[23] Ferrari, A. C., et al. Interpretation of Raman spectra of disordered and amorphous carbon. *Phys. Rev. B* **61**, 14095 (2000).

[24] Ferrari, A. C., et al. Resonant Raman spectroscopy of disordered, amorphous, and diamondlike carbon. *Phys. Rev. B* **64**, 075414 (2001).

[25] Malard, L. M., et al. Raman spectroscopy in graphene. *Phys. Rep.* **473**, 51-87 (2009).

[26] Ferrari, A. C., et al. Raman spectroscopy as a versatile tool for studying the properties of graphene. *Nature Nanotech.* **8**, 235-246 (2013).

[27] Tuinstra, F., et al. Raman spectrum of graphite. *J. Chem. Phys.* **53**, 1126-1130 (1970).

[28] Pimenta, M. J., et al. Origin of dispersive effects of the Raman D band in carbon materials. *Phys. Rev. B* **59**, 6585 (1999).

[29] Ferreri, A. C., et al. Raman spectrum of graphene and graphene layers. *Phys. Rev. Lett.* **97**, 187401 (2006).

[30] Novoselov, K. S., et al. Electric field effect in atomically thin carbon films. *Science* **306**, 666-669 (2004).

[31] Li, X., et al. Graphene films with large domain size by a two-step chemical vapour deposition process. *Nano Lett.* **10**, 4328-4334 (2010).

[32] Zhang, Y., et al. Experimental observation of the quantum Hall effect and Berry's phase in graphene. *Nature* **438**, 201-204 (2005).

[33] Novoselov, K. S., et al. Unconventional quantum Hall effect and Berry's phase of 2π in bilayer graphene. *Nature Phys.*, **2**, 177-180 (2006).

Chapter 5

All-graphene flexible touch sensor

5.1 Introduction

Touch sensing has become the dominant human interface method for detecting input for all smart phone and tablet touch screens, and all laptop computer trackpads. There are two main methods of touch sensing: capacitive and resistive[1, 2].

A four wire resistive touch sensor is illustrated in Figure 5.1a and a cross section in b, where two resistive layers are separated by insulating spacers. Each layer has two electrical contacts identified. To identify if and where the sensor is being touched, the resistance between the combination of the electrical contacts (1,2,3 and 4) is measured. If there is no pressure applied to the sensor, the top and bottom layers are isolated, hence there is high resistance between the bottom contacts (1 and 2) and the top contacts (3 and 4). When a pressure is applied, such as a stylus, shown in Figure 5.1b, the top and bottom layers are brought into electrical contact. Subsequently, a unique set of resistances is measured between the combinations of the electrical contacts (1,2,3 and 4), which corresponds to an x and y position where the touch sensor is pressed.

A four wire resistive touch sensor is limited to only detecting one input at a time. To solve this problem a more advanced geometry is required, with multiple x and y detecting electrodes, although the principle of measuring a set of resistances remains the same[3]. Resistive touch sensors dominated the market in the 90's, however the slow response times and poor sensitivity to touch input associated with resistive touch sensors has lead to the dominance of capacitive touch sensors.

There are two types of capacitive touch sensors, self capacitance and mutual capacitance [4, 5]. They have the same configuration illustrated in Figure 5.2a, where two sets of conductive electrodes are separated by a dielectric layer and the intersection between the electrodes forms a capacitor shown in Figure 5.2b. When pressure is ap-

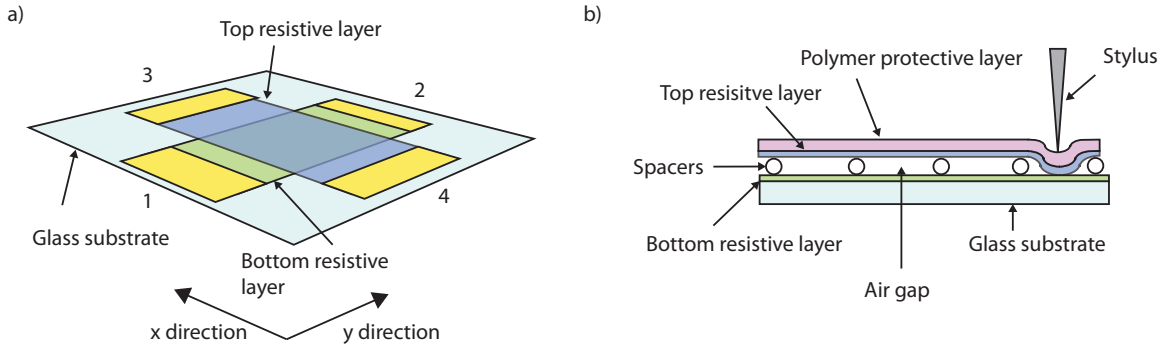

Figure 5.1: a) A schematic of a four wire resistive touch sensor, where 1 and 2 are electrical connections to the bottom resistive layer and 3 and 4 are electrical connections to the top resistive layer. Note: protective polymer layer not shown. b) A side slice across the area where both top and bottom resistors overlap, where insulating spacers are shown to separate the two resistive layers. A stylus is shown in contact with one area to demonstrate the action of pressing the two resistive layers together.

plied with a stylus to the top electrode, the dielectric material is elastically deformed hence reducing the distance between the two electrodes, as shown in Figure 5.2c. The change in the system can be explained using the parallel plate capacitor model given in Equation 5.1, where C is the capacitance of the system, ε is the permittivity of the dielectric material, A is the area of the electrodes overlapping, and d is the distance between the electrodes.

$$C = \frac{\varepsilon A}{d} \longrightarrow \Delta C = \frac{\varepsilon A}{d_1 - d_2} \tag{5.1}$$

When pressure is applied to the system, the distance between the two electrodes changes from d_1 to d_2 and the capacitance of the system is increased. In the case where the change in capacitance depends on the change in the separation of the electrodes, this is called self capacitance [4]. However, when the pressure is applied with a grounded conductor such as a human finger, shown in Figure 5.2d, there is a stray electric field

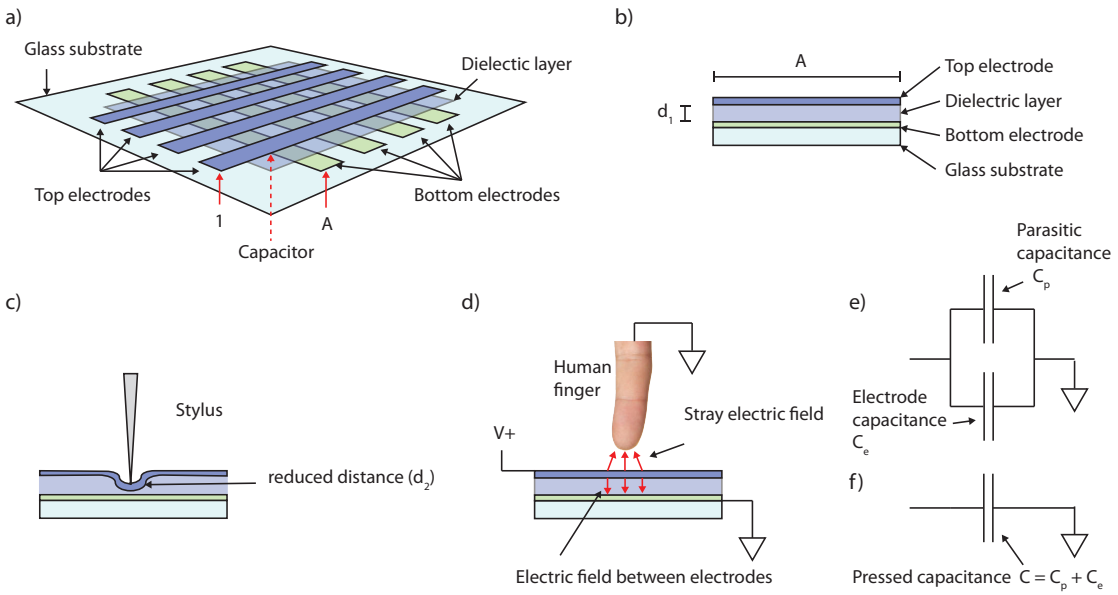

Figure 5.2: a) A schematic of a capacitive touch sensor, where two sets of conducting strips are separated by a dielectric layer, b) a side slice of a region where the top and bottom electrodes intersect, c) a schematic of self capacitance, where an insulating stylus elastically deforms the dielectric layer bringing the two electrodes closer together, d) a schematic of mutual capacitance where a human finger causes stray electric field and hence a parasitic capacitance, e) and f) are equivalent circuits showing the effect of the parasitic capacitance on the measured capacitance.

that forms between the top and bottom electrodes and the finger. The stray electric field causes a parasitic capacitance, which reduces the capacitance between the two electrodes depicted by the two equivalent circuit diagrams in Figure 5.2e and f. This is called the mutual capacitance[5]. Both methods are viable for touch sensing and are commonly used for current applications.

It is simple to detect pressure applied to a surface; however, to gain spacial information about where on the surface is being pressed requires the geometry shown in Figure 5.2a to form an array of capacitors. Each capacitor can be independently measured using the corresponding strips; for example, to address the capacitor shown,

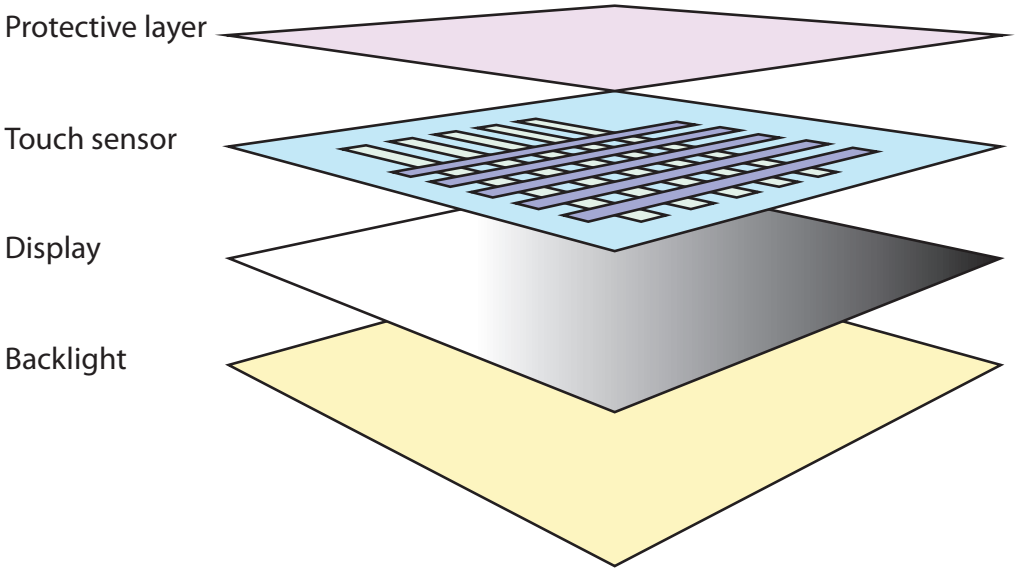

Figure 5.3: A schematic of the construction of a smart phone screen illustrating the need for the touch sensor to be transparent.

strips A and 1 are used.

When touch screens are used for smart phones and tablets they are sandwiched between the display and a protective glass layer as shown in Figure 5.3. Therefore, the sensor must be transparent to allow light to efficiently travel from the backlight and out of the front of the device. The industry standard transparent conductor is Indium Tin Oxide (ITO), which has high optical transmission combined with a low sheet resistance[6]. However, for the next generation of flexible electronics, all of the materials used in the construction of the touch sensor must be flexible. ITO is brittle and when exposed to repeated strain the electrodes crack [7, 8, 9]. This has a significant effect on the electrical properties of the ITO electrodes, causing a reduction in the sensitivity and response time of the sensor, which eventually leads to a total failure of functionality.

It is clear that new transparent conductors are required for the next generation of flexible and transparent touch sensors. Graphene has demonstrated a high tolerance to flexing [10], high optical transparency and high electrical conductance [11]. Furthermore, with the outstanding chemical stability and compatibility with existing silicon based electronics [12], graphene is an ideal material to replace ITO for flexible touch sensors.

The first resistive graphene touch sensor was demonstrated in 2013[11]; the approach used a four wire resistive geometry, shown in Figure 5.1, where ITO was replaced with monolayer CVD graphene. When the sensor is pressed, the two graphene layers are brought into electrical contact, and the position of the touch can be determined though resistance measurements. Building on this advancement, there has been the recent development of resistive graphene touch sensors that allow for multi-touch inputs[13]; however, the functionality of these devices is limited by the mechanical properties of graphene. Repeated pressing of the unprotected graphene layers causes damage to both layers. Over time this reduces the functionality of these resistive touch sensors, limiting the viability of commercialisation.

CVD graphene has been used as the electrode material for a capacitive touch sensor[14] as illustrated in Figure 5.2a. In this device, two sets of graphene strips are separated, by an optically clear adhesive (OCA), which is used as the dielectric layer and supported by a glass substrate. The device was demonstrated in a smart phone by replacing a conventional ITO based touch sensor. However, the sensor was fabricated on a rigid glass substrate. limiting the applications to conventional rigid electronics, and not flexible systems. This alludes to the major technical hurdle for an all-graphene capacitive touch sensor.

It has been shown that the adhesion of graphene to a surface depends on the surface

roughness[15, 16]. There is high adhesion for flat substrates like hexagonal boron nitride (h-BN) and glass, and poor adhesion for rough substrates like plastic. However, plastic must be used to allow for flexibility of the device. When a flexible dielectric material is added by spin coating, which is needed to achieve thin dielectric layers, the graphene strips detach from the plastic surface destroying the device. To solve this problem I developed a novel fabrication procedure which preserves the structure of the graphene strips, therefore allowing us to create the first flexible all-graphene touch sensor. Furthermore, the processes allows for the touch sensor to be created on arbitrary insulating substrates.

5.2 Fabrication process

To fabricate the touch sensor I use CVD graphene grown on a copper foil, as shown in Figure 5.4a. The foil is spin coated with PMMA and baked at 180°C to cure the PMMA film. The PMMA is exposed using electron beam lithography to define contacts (shown in Figure 5.4b and Figure 5.5a). The PMMA is developed, coated with 50nm of gold and lifted off (shown in Figure 5.4c and Figure 5.5b). PMMA is then spin coated, baked at 180°C and the graphene strips are patterned using electron beam lithography (shown in Figure 5.4d). The PMMA is then developed and the exposed graphene is etched using an oxygen/argon plasma (shown in Figure 5.4e and Figure 5.5c). A support layer of PMMA, which also acts as the dielectric layer, is spin coated onto the structure and vacuum cured for 30 minutes. The copper foil is floated on the surface of a 1 mol $FeCl_3$ solution and the copper foil is etched (shown in Figure 5.4f and Figure 5.5d). The PMMA coated graphene structure is repeatedly transferred to ultrapure deionised water to remove the residual $FeCl_3$ etchant (shown in Figure 5.4g). It is then

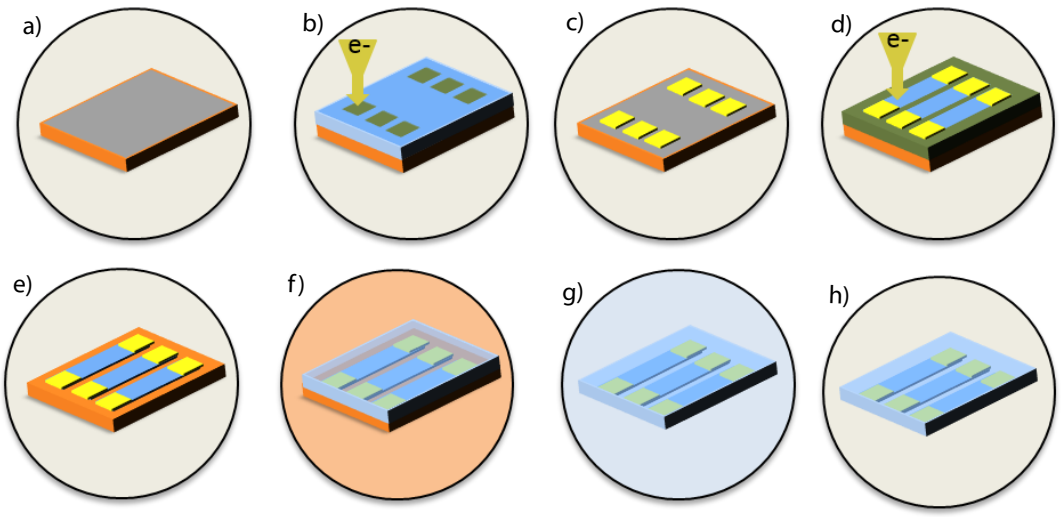

Figure 5.4: A schematic of the process for fabricating the touch sensor devices. a) Graphene is grown on a copper substrate, b) the foil is coated with PMMA and contacts are exposed using electron beam lithography, c) exposed regions are developed and metallised with 50nm of gold, d) the foil is coated with PMMA and an etch mask is defined between the gold contacts with electron beam lithography, e) exposed graphene is etched using an argon/oxygen plasma, f) the foil is coated with PMMA and the copper is etched using 1 molar $FeCl_3$, g) the film is washed in ultrapure water, and h) the film is transferred to a PEN substrate.

transferred onto a Polyethylene naphthalate (PEN) substrate (shown in Figure 5.4h and Figure 5.5e) resulting in a set of contacted graphene strips coated with PMMA dielectric on a flexible plastic substrate. For the top layer of graphene strips, I pattern and contact the graphene on a copper foil as before, (shown in Figure 5.4a-g and Figure 5.5a-d). The copper foil is then wet etched and transferred orthogonally onto the PEN substrate to the bottom layer of graphene strips (as shown in Figure 5.5f).

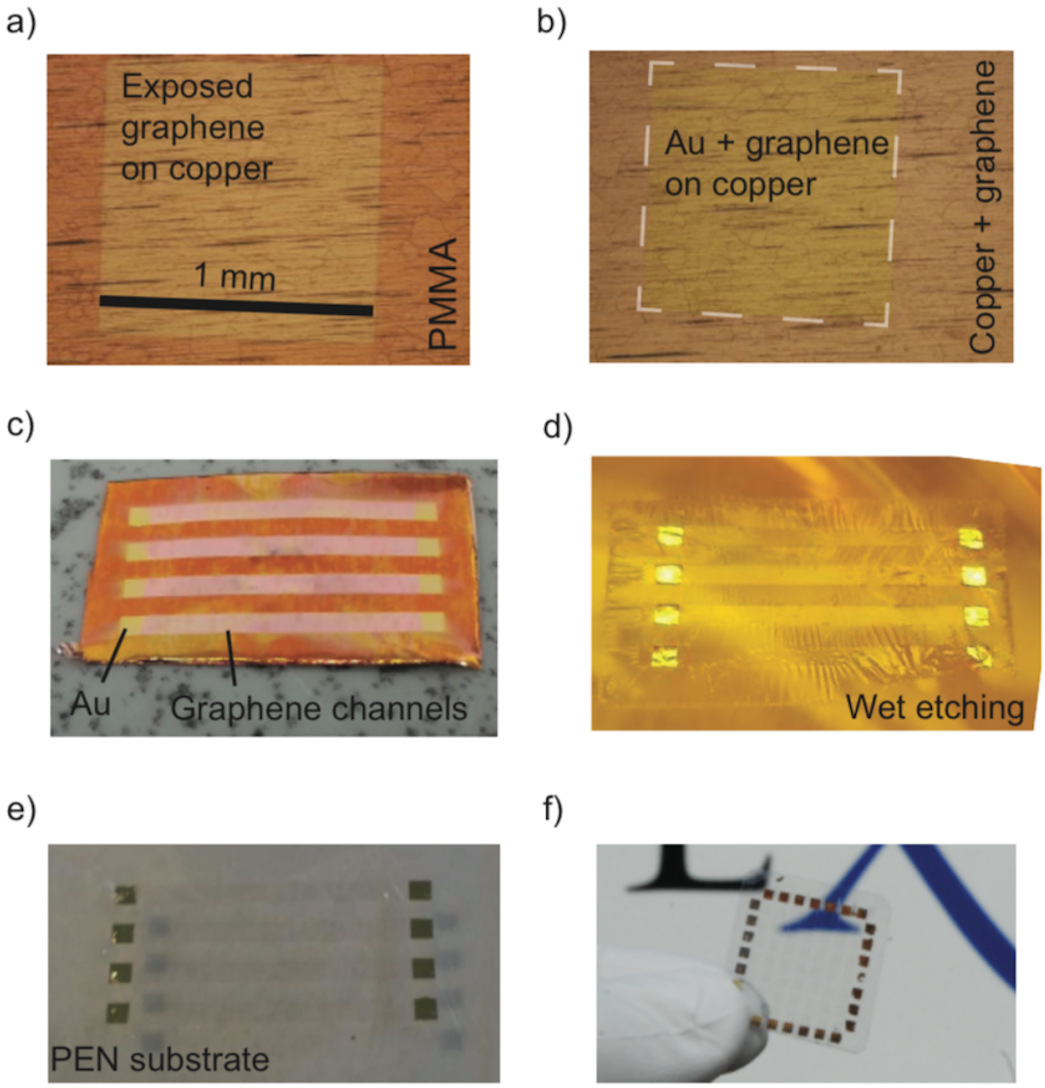

Figure 5.5: a) Window in PMMA after electron beam exposure and development on copper foil coated in CVD graphene, b) a gold square after the metallisation gold on top of a copper foil coated with CVD graphene, c) gold contacts connected by graphene strips on the surface of the copper foil, d) the gold contacts and graphene strips supported by a PMMA film floating on $FeCl_3$ etchant solution, e) the transferred structure onto a PEN substrate, and f) an example of a finished device where two sets of graphene strips have been orthogonally transferred on the PEN substrate

5.3 Device characterisation

To characterise the electrical properties of the graphene strips, I made a single strip of graphene with multiple gold contacts (Figure 5.6a) where the width of the channel is W and the length between the contacts is L. I used electrical probes to make electrical contact with the gold pads on the device, shown in Figure 5.6b. To determine the resistivity of the graphene strip I measured the two terminal resistance between pairs of gold contacts with different separations (Figure 5.6c) using a Keithly 2400 source meter. The resistivity of a two-dimensional material is related to the resistance by Equation 5.2.

$$R_{graphene} = \rho_{graphene}\frac{L}{W} \tag{5.2}$$

Where $R_{graphene}$ is the sample resistance, $\rho_{graphene}$ is the sample resistivity or sheet resistance, L is the sample length and W is the sample width. By plotting the measured resistance against the length between the contacts divided by the channel width (the number of squares), as in Figure 5.6d, I observed a linear relationship as implied by Equation 5.2. However, in this two terminal measurement, as dwscribed in Section 3.5.3, R is a combination of the series resistance of the measurement circuit wires (R_{system}), the contact resistance ($R_{contact}$) and the resistance of the graphene ($R_{graphene}$). As the contact pads are all identical and the measurement circuit is unchanged, I assume that $R_{contact}$ and R_{system} are constant and independent from sample length, as expressed in Equation 5.3.

$$R_{measured} = R_{system} + 2R_{contact} + R_{graphene}(L) \tag{5.3}$$

Therefore as only $R_{graphene}$ depends on L, a linear fit of the plot in Figure 5.6d give the resistivity of the graphene strip of 1.3 KΩ per square (KΩ / □). The system resistance is measured by shorting the two electrical probes together, for which I measured 0.4Ω. Finally, the contact resistance is estimated by taking the value of the y intercept (where L = 0) which results in a contact resistance of 68Ω per contact. This measurement shows that a continuous strip of graphene is present across the device with a low contact resistance.

To ensure that each graphene strip in the touch sensor was continuous, I measured the resistance across all of the strips to check for electrical continuity. I found that all of the strips conducted and had a resistance that is described by Equation 5.2.

5.4 Touch sensing

The measurement of a single element with unknown capacitance, illustrated in Figure 5.7a and b, was performed with a capacitive Wheatstone bridge in null offset operation. An AC voltage is applied between points 1 and 2 in the circuit shown in Figure 5.7b. The value of R_1 is tuned until the voltage drop measured between points 3 and 4 is zero. Once the bridge is balanced ($V_{3\to4} = 0$), the unknown capacitance C_x can be estimated from the known values of R_1, R_2 and C_1, through Equation 5.4.

$$C_x = C_1 \frac{R_2}{R_1} \tag{5.4}$$

To detect the change in self capacitance for the touch sensor when a load is applied to one element, I first measured the capacitance of each element with no load applied to the sensor. For this I used two electrical probes and a Hameg 8118 capacitive bridge. A

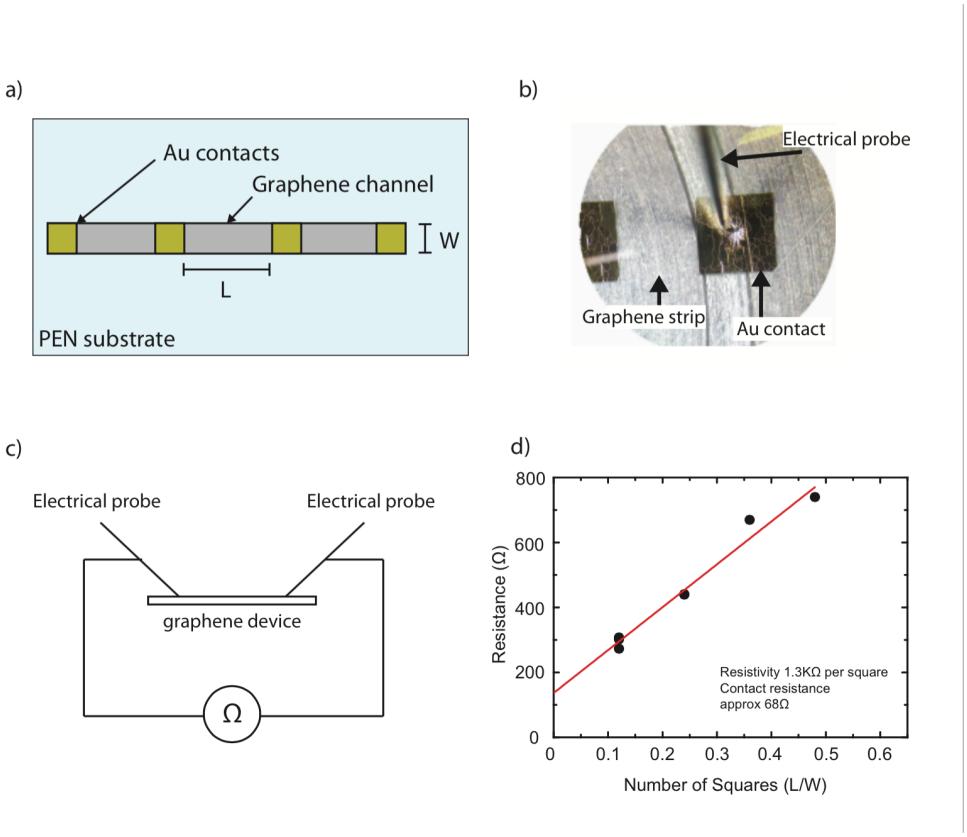

Figure 5.6: a) Schematic of a set of gold contacts on a single graphene strip, where L is the length between gold contacts and W is the width of the graphene strip, b) a photograph showing a measurement probe in electrical contact with a gold pad, c) a circuit diagram showing the two terminal measurement of the graphene strip using a Keithly 2400 source meter, and d) the measured two terminal resistance plotted against the number of squares (L/W). The error bars as smaller than the size of the data points.

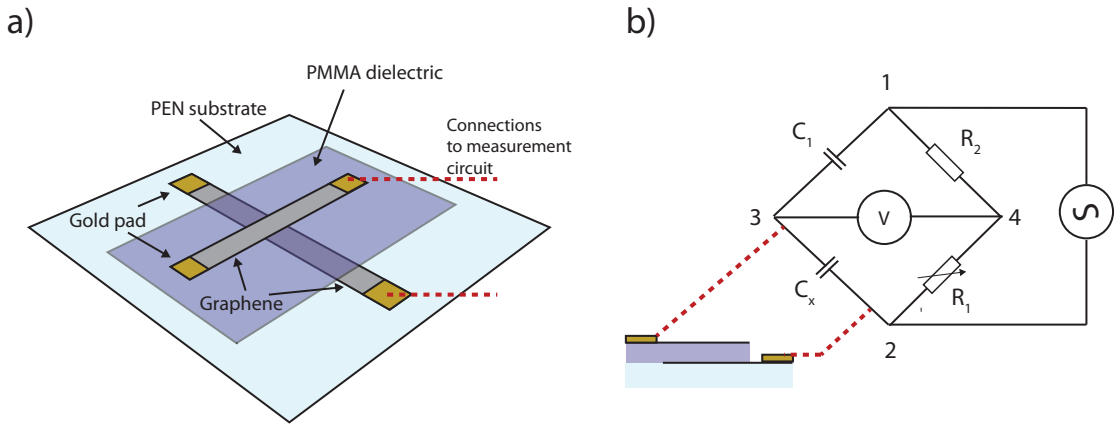

Figure 5.7: a) Schematic of a single element of the all-graphene touch sensor, where the dashed red lines indicate the connections to the measurement circuit, and b) the circuit diagram showing a variant of the Wheatstone bridge used for measuring an unknown capacitance C_x of the element; inset: the element connected by red dashed lines.

load of 36g was applied to one element (indicated by a white arrow) using an insulating probe. Simultaneously, the capacitance of each element was measured as before. The normalised change in capacitance is plotted in Figure 5.8a, where C_1 and C_0 are the loaded and unloaded capacitance respectively and $\Delta C = C_1 - C_0$.

From the response of the sensor, I observed that the maximum change in capacitance occurs at the element where the pressure is applied. This result indicates that the touch sensor can detect applied pressure through self capacitance and determine where the pressure is applied.

Furthermore, I demonstrated the mutual capacitive response for the touch sensor by measuring the change in capacitance, where one element is repeatedly touched with a human finger. Figure 5.8b shows the change in capacitance with respect to time for several light presses of the device. It was observed that the measured capacitance changes significantly, however upon unloading the capacitance returns to the initial

value. Once the resulting change from loading or unloading has occurred, the capacitance remains stable until the load is changed.

5.5 Flexibility measurement

To determine the tolerance of the touch sensor to repeated flexing, I bent the device around a 2cm cylindrical radius. I measured the change in the resistance across the graphene strips after the sensor was returned to its natural state. Figure 5.8c shows the percentage change in the resistance of two graphene strips over the course of 2000 bends, one parallel (black) and the other perpendicular (red) to the bending direction. It was observed that there was some variation of the resistance, however it remains below a 3% change in total strip resistance for both strip orientations after 2000 bends. This demonstrates the durability and flexibility of the graphene strips in the touch sensor, in stark contrast to the degradation of the electrical properties of ITO electrodes.

5.6 Conclusion

In this chapter, I presented a novel fabrication technique for manufacturing a graphene capacitive touch sensor. Subsequently, I demonstrated that the sensor can spatially detect when a probe is brought into contact with a load of 36g through self capacitance. Furthermore, I showed the repeated detection of a human finger on a single element due to mutual capacitance. Finally, I demonstrated the flexibility and durability of the sensor by observing only minor changes in the electrical properties of the graphene strips after 2000 bends.

I conclude two important facts. Firstly, graphene is indeed a suitable electrode

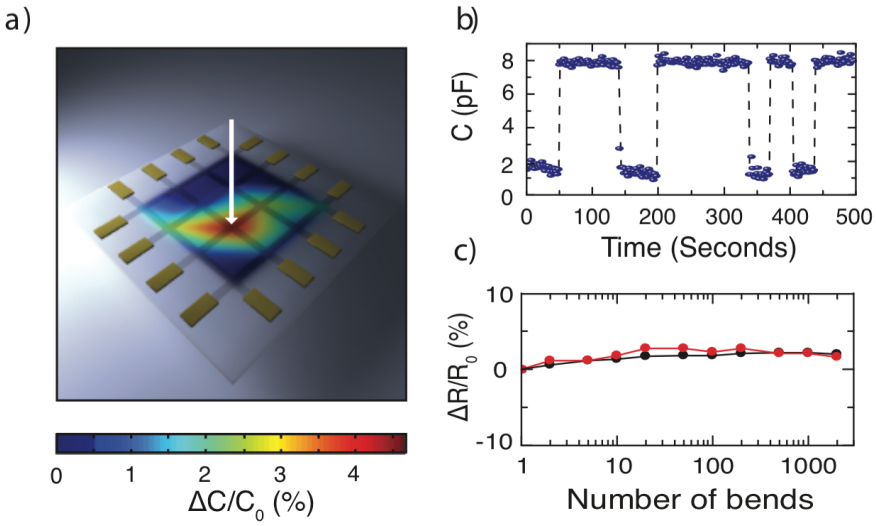

Figure 5.8: a) Schematic of all of the elements on the device, the colour plot represents the change in the capacitance when a 36g load is placed on one element and the white arrow indicates the element where the load was applied, b) change in capacitance with respect to time for a human finger repeatedly touching an element, c) change in resistance of the graphene strips after uniaxially bending the sensor around a 2cm bending radius, parallel (black) and perpendicular (red) to bending radius

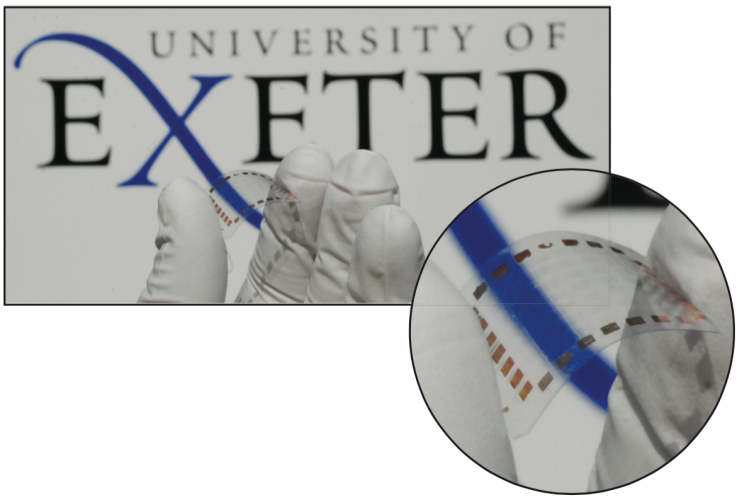

Figure 5.9: An example of a touch sensor similar to the device tested.

material for flexible capacitive touch sensors, proved by my prototype device shown in Figure 5.9. Secondly, this novel fabrication technique can be used to create structures where other fabrication techniques were previously limiting the development of flexible graphene electronics.

Bibliography

[1] Stumpe, B., et al. Data processing. *CERN Courier*, **1**, 117 (1974).

[2] Johnson, E. A., Touch display? A novel input/output device for computers. *Electronics Lett.* **1**, 219-220 (1965).

[3] Cheng, D., Onetouch Technologies Co., Ltd., Patent number: US6917358.

[4] Hanauer, J., et al., Microchip Technology Incorporated., Patent number: US20120113047 A1.

[5] Hotelling, S., Apple Inc., Patent number: US8514185 B2.

[6] Lee, J., et al. Solution-Processed Metal Nanowire Mesh Transparent Electrodes. *Nano Lett.* **8**, 689-692 (2008).

[7] Yu, Z., et al. Highly Flexible Silver Nanowire Electrodes for Shape-Memory Polymer Light-Emitting Diodes. *Adv. Matt.* **23**, 664-668 (2010).

[8] Cairns, D. R., et al. Strain-dependent electrical resistance of tin-doped indium oxide on polymer substrates. *App. Phys. Lett.*, **76**, 1425-1427 (2000).

[9] Hecht, D. S., et al. Emerging Transparent Electrodes Based on Thin Films of Carbon Nanotubes, Graphene, and Metallic Nanostructures. *Adv. Matt.* **23**, 1482-1513 (2011).

[10] Bae, S., et al. Roll-to-roll production of 30-inch graphene films for transparent electrodes. *Nature Nanotech.* **5**, 574-578 (2010).

[11] Bae, S. H., et al. Graphene-based transparent strain sensor. *Carbon* **51**, 236-242 (2013).

[12] Wang, X., et al. Transparent, Conductive Graphene Electrodes for Dye-Sensitized Solar Cells. *Nano Lett.* **8**, 323-327 (2008).

[13] Chun, S., et al. A flexible graphene touch sensor in the general human touch range. *App. Phys. Lett.* **105**, 041907 (2014).

[14] Ryu, J., et al. Fast Synthesis of High-Performance Graphene Films by Hydrogen-Free Rapid Thermal Chemical Vapor Deposition. *ACS Nano* **8**, 950-956 (2014).

[15] Kinloch, I., et al., The University of Manchester, Patent number: EP2526050 A1.

[16] Chen, H., et al. Adhesive contact between a graphene sheet and a nano-scale corrugated surface. *J. Phys. D:Appl. Phys.* **46**, 205303 (2013).

Chapter 6

Functionalising few layer graphene flakes with $FeCl_3$

6.1 Introduction

Future flexible displays and photovoltaics, and the associated electronics require materials that are flexible, optically transparent and electrically conductive. As discussed in Section 2.4 and Chapter 5, the industry standard transparent electrode material is indium tin oxide (ITO), however, it is mechanically rigid and incompatible with flexible applications[1, 2]. Monolayer and few layer graphene share many of the properties desirable for flexible transparent conductors, including high optical transparency[3], low production cost (Chapter 4), high mechanical flexibility and strength[4, 5]. Yet graphene electrodes are limited by a high intrinsic resistivity, when compared to ITO. This leads to a higher dissipation of energy in the electrode material, hence reduced device efficiency.

A reduction in the sheet resistance of monolayer and few layer graphene has been achieved through chemical functionalisation, where the best results yield 30 $\Omega/\square$ with 90% optical transmission and 125 $\Omega/\square$ with 97.7% optical transmission respectively[4, 6]. However, this is still three times larger than values reported for 10 μm thick ITO (10 $\Omega/\square$ with 85% optical transmission[7]).

In this chapter, I demonstrate a novel graphene based graphene conductor with a sheet resistance as low as 8.8 $\Omega/\square$ with 84% optical transmission. Furthermore, I observed a high charge carrier concentration of $8.9\times10^{14}\text{cm}^{-2}$ and a room temperature mean free path as large as ≈ 0.6 μm. These graphene based materials are obtained with intercalation of ferric chloride ($FeCl_3$). Through a combined study of Raman spectroscopy, optical transmission spectroscopy and electrical transport techniques, I confirm the intercalation of $FeCl_3$ and the suitability of the resulting material as a transparent conductor. Finally, I demonstrate the stability of the $FeCl_3$ intercalated

few layer graphene in a range of conditions.

6.2 Fabrication of $FeCl_3$ intercalated few layer graphene flakes

Pristine few layer graphene ranging from bilayer to five layers was obtained on a glass substrate using mechanical exfoliation, as described in Section 3.2.1. The number of layers of each few layer graphene flake was determined using optical contrast techniques (Section 3.5.1) and Raman spectroscopy (Section 3.5.2). The $FeCl_3$ intercalation was performed using the two zone vapour transport technique[8], as discussed in Section 3.4. The resulting flakes were characterised using Raman spectroscopy, optical transmission measurements and low temperature electrical transport techniques.

6.3 Raman spectroscopy of $FeCl_3$ intercalated few layer graphene

Figure 6.1 shows the Raman spectra of few layer graphene before the intercalation procedure. For the pristine graphene, I observed an increase in the G-peak intensity and an evolution of the multipeak structure of the 2D peak related to the increase in the number of layers, discussed in Section 3.5.2. After the intercalation, I observed a change in the measured Raman spectra (Figure 6.3) due to the charge transfer from the $FeCl_3$ molecules[9, 10].

First there is an upshift in the G-peak related to the configuration of $FeCl_3$ and the graphene layers in the structure[9, 10], shown in Figure 6.2. For each layer of graphene

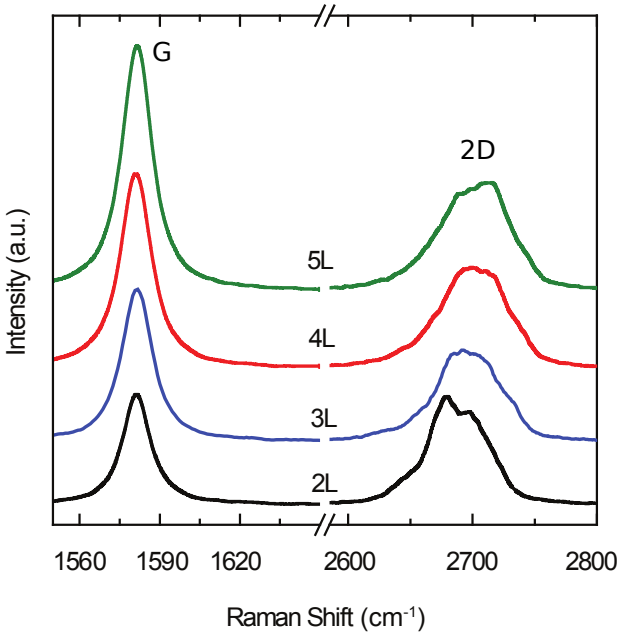

Figure 6.1: The Raman spectra of pristine bilayer graphene to five layer graphene, in the region on the G and 2D peaks.

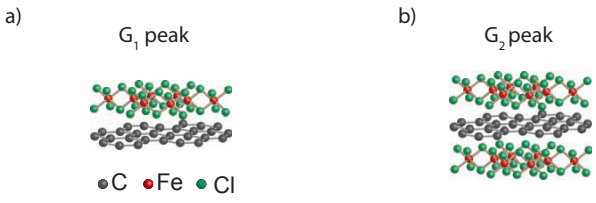

Figure 6.2: The configuration of the $FeCl_3$ and graphene layers that give rise to a) the G_1 peak, where each graphene layer has one adjacent layer of $FeCl_3$ and b) the G_2 peak, where each graphene layer has two adjacent $FeCl_3$ layers.

with one adjacent layer of $FeCl_3$, the G-peak is upshifted to 1612cm^{-1}, known as the G_1 peak. Similarly, for each layer of graphene with two adjacent layers, the G-peak is upshifted to 1624cm^{-1}, the G_2 peak. The frequencies, line widths and line shapes of the G_1 and G_2 peaks do not depend on the number of graphene layers. Furthermore the multipeak structure of the 2D-peak becomes single peaked, as shown in Figure 6.3. This behaviour is consistent with observations from studies where few layer graphene was intercalated with Potassium and Rubidium[11, 12]. However, in the case of a partial intercalation, identification of the structural composition cannot rely uniquely on the Raman spectra. Further confirmation is required using complementary electrical transport measurements[13].

6.4 Electrical transport measurements of $FeCl_3$ intercalated few layer graphene

To measure the electrical properties of $FeCl_3$ intercalated graphene, I first characterised pristine few layer graphene. All devices were patterned into a Hall bar geometry and electrically contacted, as described in Section 3.3.

I measured the resistivity of bilayer to 5-layer pristine graphene flakes as a function of temperature and results are shown in Figure 6.4. Firstly, I observed room temperature resistivities of $2.5\times10^3\Omega/\square$ for bilayer devices, monotonously decreasing to $1.2\times10^2\Omega/\square$ for a 5-layer device. Secondly, I observed a semi metallic temperature dependence, where the resistivity of all of the graphene samples increases with reducing temperature. The measured resistivity of the bilayer to 5-layer $FeCl_3$ intercalated graphene (Figure 6.5) shows a significant reduction in the room temperature resistivi-

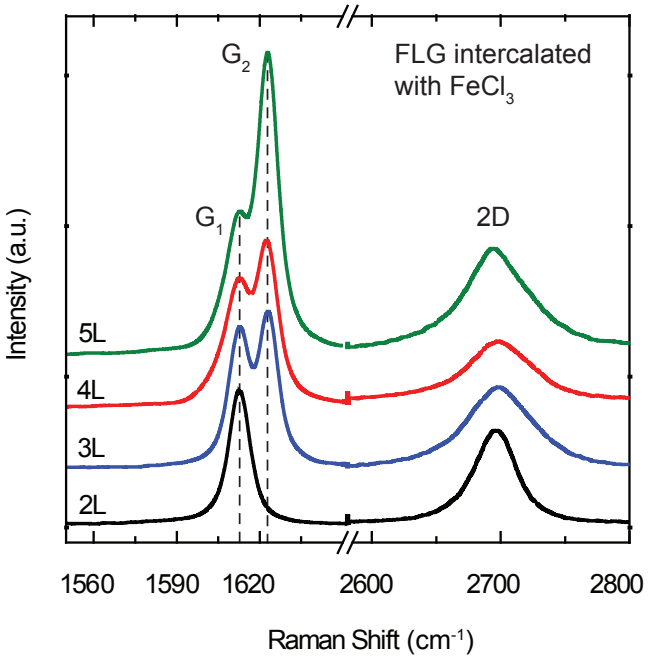

Figure 6.3: The Raman spectra for $FeCl_3$ intercalated graphene ranging from bilayer graphene to 5-layer graphene, with a focus on the $G_{1,2}$ and 2D peaks.

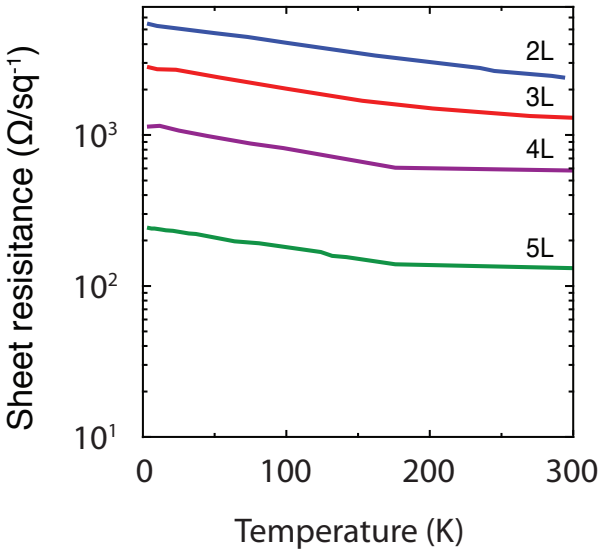

Figure 6.4: The measured sheet resistance with respect to sample temperature for pristine bilayer, trilayer, 4-layer and 5-layer graphene.

ties for all flake thicknesses, apart from the bilayer sample. The resistivity reduced as the layer number increased from 600 Ω/□ for trilayer graphene to 8.8 Ω/□ for 5-layers graphene. Furthermore, the temperature dependence shows, for trilayer to 5-layers, of a metallic conductor, that the resistivity reduces with decreasing temperature. However, the bilayer sample shows the semi-metallic behaviour of the pristine analogue. The explanation for why the measured bilayer sample behaves differently to the other intercalated samples is routed in the fabrication process. It has been shown that exposure to solvents, such as Acetone and IPA, used in the patterning and contacting procedure causes a deintercalation of the structure [13, 14]. As the bilayer sample has only one $FeCl_3$ layer, it is more susceptible to deintercalation.

To discover the origin of the low sheet resistivity of the intercalated few layer graphene, I investigated the effect of the charge transfer from the introduced $FeCl_3$.

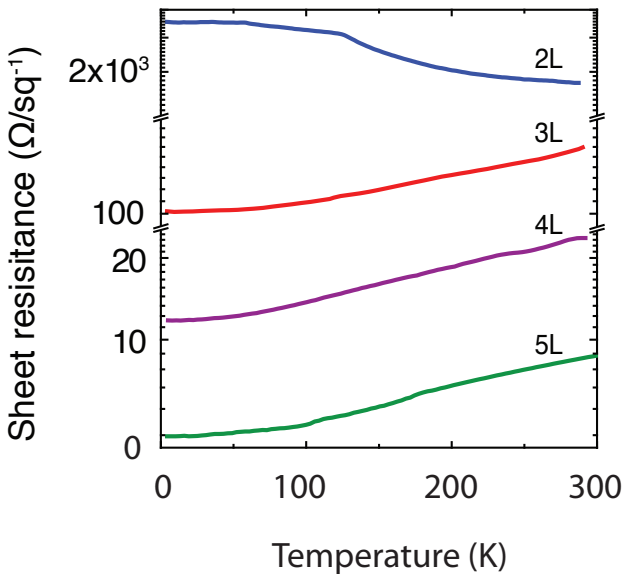

Figure 6.5: The measured sheet resistance with respect to temperature for $FeCl_3$ intercalated bilayer, trilayer, 4-layer and 5-layer graphene.

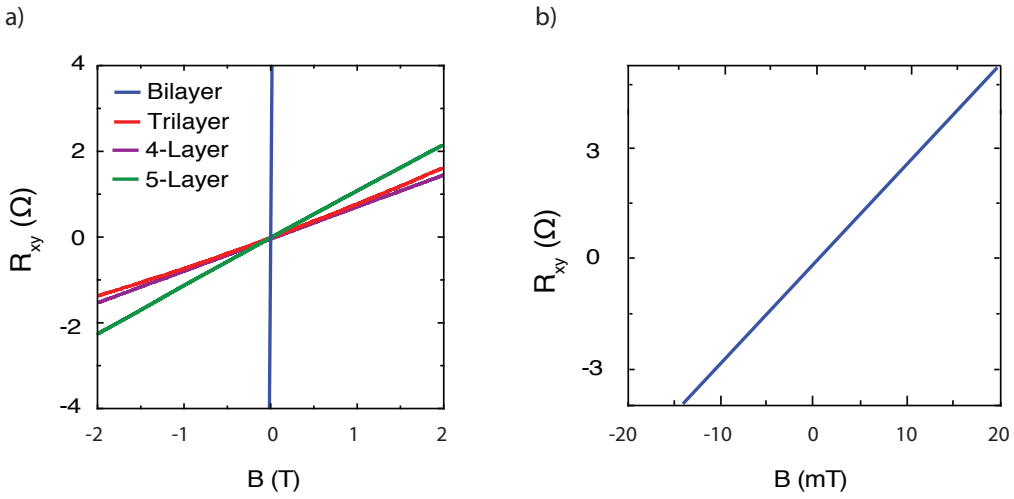

Figure 6.6: a) The measured Hall resistance plotted against perpendicular applied magnetic field, b) a zoomed plot of the measured Hall resistance for $FeCl_3$ intercalated bilayer graphene. All measurements were performed at 4.2K.

I measured the Hall resistance with respect to perpendicular applied magnetic field, and results are shown in Figure 6.6. Fitting the linear Hall resistance allows for the estimation of the charge carrier concentration, as described in Section 2.2.2. I observed, for all samples thicker than bilayer, a charge carrier concentration between 4×10^{14} and 9×10^{14} cm^{-2}, as shown in Figure 6.7a. Furthermore, the sign of the fitted gradient shows that the dominant charge carriers are holes as the Lorentz force acts oppositely for electrons and holes. This record high charge carrier concentration is three orders of magnitude larger than that of pristine graphene at the CNP. The increased charge carrier concentration increases the Fermi energy, hence the conduction of the material, as discussed in Section 2.2.1.

To demonstrate that there is no degradation of the electrical quality of the intercalated graphene, I estimated the charge carrier mobility, using the method discussed in Section 2.2.3, which is shown in Figure 6.7b. I observed mobilities similar to that of

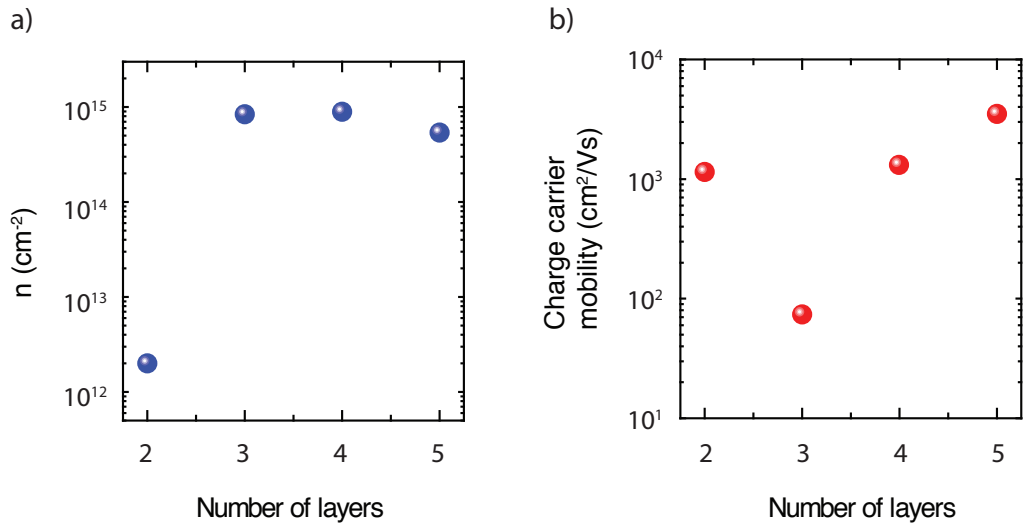

Figure 6.7: a) The measured charge carrier concentration, of $FeCl_3$ intercalated graphene plotted against the number of graphene layers, b) the estimated charge carrier mobility of $FeCl_3$ intercalated graphene plotted against the number of graphene layers.

pristine graphene, with a maximum observed mobility in $FeCl_3$ intercalated few layer graphene of 3500 cm^2/(V.s). Furthermore, I estimated the room temperature mean free path for 5 layer intercalated graphene to be 0.6 μm, suggesting low amounts of disorder or structural damage present after the intercalation process.

6.5 Determining the optical transmission of $FeCl_3$ intercalated few layer graphene

I prepared mechanically exfoliated few layer graphene onto transparent glass substrates and determined the number of layers. The optical transmission was determined using the technique described in Section 3.5.1. The few layer graphene flakes were then intercalated with $FeCl_3$ using the two zone vapour transport method and the intercalation

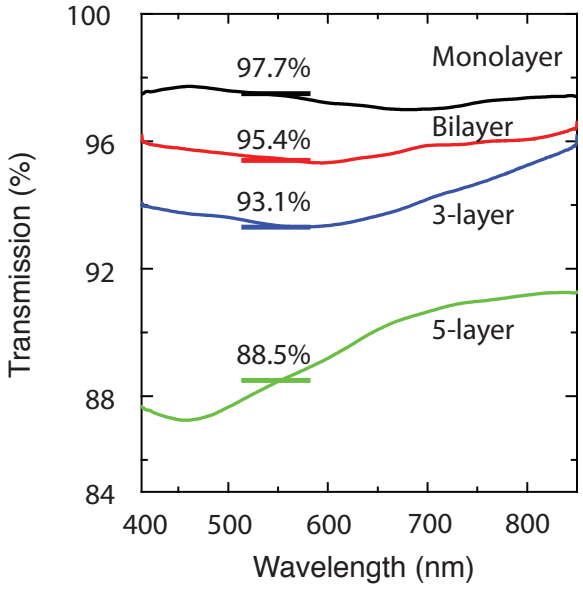

Figure 6.8: The optical transmission of pristine few layer graphene ranging from monolayer graphene to 5 layer graphene. The transmission indicated is for a wavelength of 550nm.

was confirmed using Raman spectroscopy. To monitor the change in the optical transmission I remeasured the transmission after the intercalation of the few layer graphene flakes.

Figure 6.8 shows the optical transmission of pristine graphene (mono-, bi-, tri- and 5-layer), while Figure 6.9 shows the optical transmission for $FeCl_3$ intercalated few layer graphene (bi-, tri-, 4- and 5-layer), both for the visible wavelength range of light (400nm-850nm). I observed the transmission taken at 550nm of the pristine graphene ranged from 97.7% for monolayer graphene to 88.5% for 5-layer graphene. When I compared this to the $FeCl_3$ intercalated graphene, I observed a small reduction in the 550nm transmission. The $FeCl_3$ intercalated bilayer graphene has a transmission of 94.5%, which reduces monotonously to 84.1% for 5 layers.

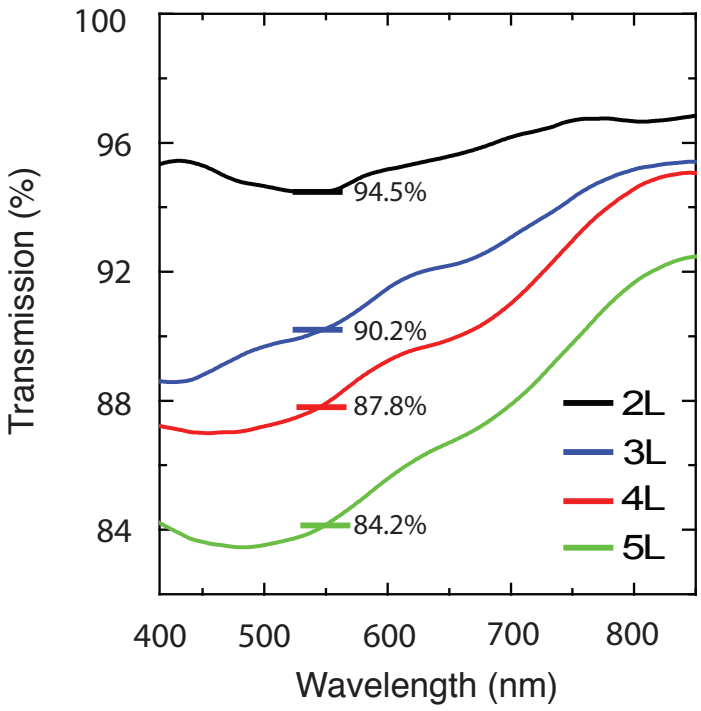

Figure 6.9: The optical transmission of $FeCl_3$ intercalated few layer graphene, ranging from bilayer graphene to 5 layer graphene. The transmission indicated is for a wavelength of 550nm.

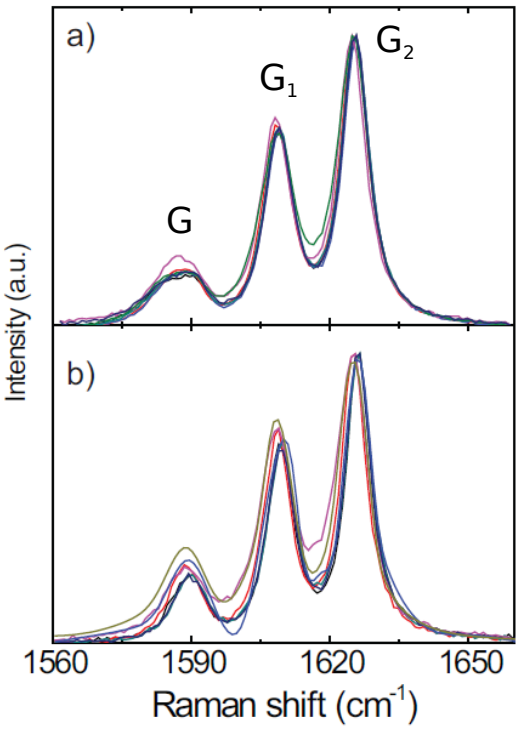

Figure 6.10: Several Raman spectra taken across the area of an $FeCl_3$ intercalated sample a) just after the intercalation process and b) after 3 month exposure to atmosphere.

6.6 The stability of $FeCl_3$ intercalated graphene

$FeCl_3$ is highly soluble in water, therefore it would be intuitive to suggest that $FeCl_3$ intercalated graphene would not be stable in air, due to the ambient humidity, quickly reducing the material to pristine graphene. However, I found that the $FeCl_3$ intercalated graphene is stable and shows no significant deintercalation. I demonstrated this stability with three experiments; leaving the sample exposed to the atmosphere for three months and comparing the Raman spectra before and after; heating the sample in atmosphere up to 150°C and measuring the room temperature resistivity; exposing a sample to high levels of humidity (>95%) and measuring the resistivity.

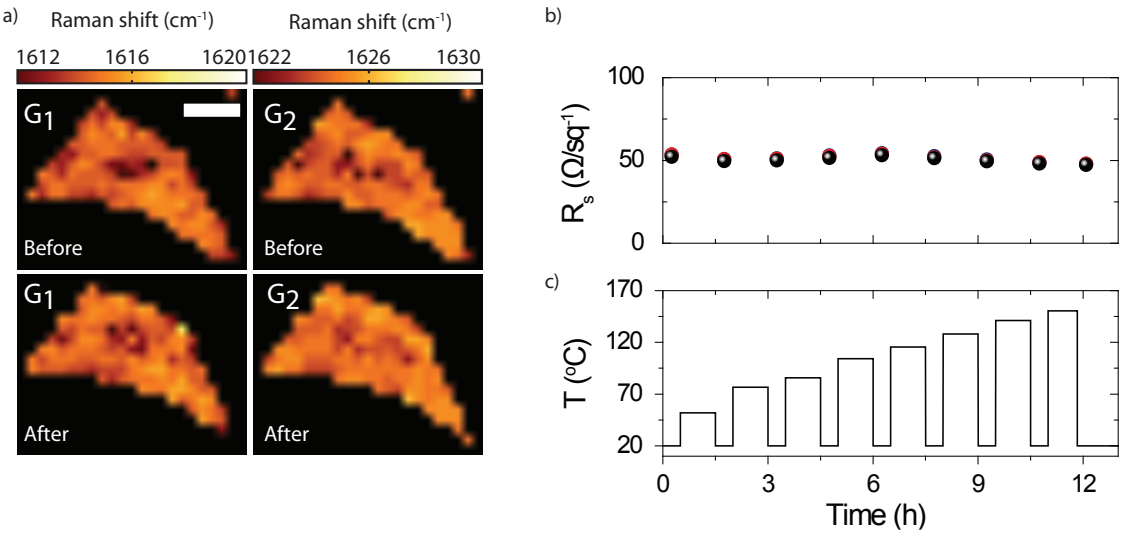

Figure 6.11: The Raman maps showing the G_1 and G_2 peaks before and after heating to 150°C (scale bar : 10μm), b) the sheet resistance measured at room temperature after exposure to heating detailed in c). All sample heating was performed in atmosphere.

Figure 6.10 shows the Raman spectra of a partially $FeCl_3$ intercalated graphene flake just after the intercalation process and after exposure to atmosphere for three months. Although there are minor changes in the intensities of the G, G_1 and G_2 peaks, the peak positions, shapes and relative intensities remain the same. If deintercalation had occurred, I would observe an increase in the G peak and simultaneous reduction in the G_1 and G_2 peaks. This is not observed allowing me to conclude that $FeCl_3$ intercalated graphene is stable in atmosphere at room temperature.

I then determined the stability of $FeCl_3$ intercalated graphene up to temperatures of 150°C in atmosphere. First, I compared the Raman spectra before and after heating, as shown in Figure 6.11a. I observed no change in the positions of the G_1 and G_2 between before and after heating the sample to 150°C for 30 minutes. This demonstrates that there is no deintercalation occurring in the sample of the sample. Furthermore, I tested

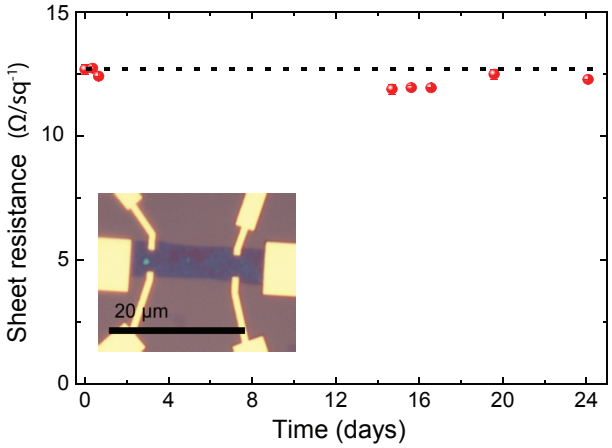

Figure 6.12: The sheet resistance of a $FeCl_3$ intercalated graphene flake measured after exposure to $>$ 95% humidity from 0 to 24 days. The inset shows the measured device.

the stability at temperatures up to 150°C using electrical transport measurements. I patterned and contacted a $FeCl_3$ intercalated few layer graphene device. The resistivity was measured at room temperature, the sample was heated to 50°C for 30 minutes, the sample was cooled to room temperature and the room temperature resistivity was measured. The temperatures at which the sample was exposed where incrementally increased from 50 to 150°C, as shown Figure 6.11c. As the resistivity of the sample does not change (Figure 6.11b) I conclude that there is no deintercalation while the sample is heated in atmosphere, reinforcing the results from the Raman maps in Figure 6.11a.

Finally, I demonstrate the stability of $FeCl_3$ intercalated graphene in high humidity conditions. I loaded a contacted $FeCl_3$ intercalated graphene device into a chamber where the (relative) humidity can be controlled in the range, 0 to 95%, and the resistivity can be measured in-situ.

I measured the resistivity of the sample before humidity exposure, then I exposed

the sample to $> 95\%$ humidity for 1 day. The sample was dried and the resistivity was remeasured. I repeated the exposure until the cumulative exposure was 24 days. I plotted the resistivity against time in Figure 6.12, where the device is shown in the inset. There was no significant change in the resistivity after the prolonged exposure to high levels of humidity.

To complement the electrical transport study for high humidity exposure, I performed a Raman study of the same sample. Figure 6.13 shows the Raman spectra from the same region of the sample after exposure to high levels of humidity. I observed that there is no observable change in the relative intensities of the G_1 and G_2 after an exposure of 25 days.

Combining the information from these experiments, I demonstrated the stability of $FeCl_3$ intercalated graphene for long atmospheric exposure, temperatures of up to 150°C and 24 days at $> 95\%$ humidity.

6.7 $FeCl_3$ intercalated graphene flakes as a transparent conductor

The high optical transparency observed for $FeCl_3$ intercalated graphene is complemented by the remarkable electrical conductivity. However, to replace materials such as ITO as a transparent electrode, the properties should exceed or match that of commercially available ITO ($R_s = 10\ \Omega/\square$ with a 550nm transmission of 85%)[7]. In Figure 6.14, I compare the 550nm transmission and conductivity of ITO and the leading carbon based materials, doped carbon nanotube arrays [15, 4], doped monolayer graphene and $FeCl_3$ intercalated graphene. The multiple points represent different thicknesses

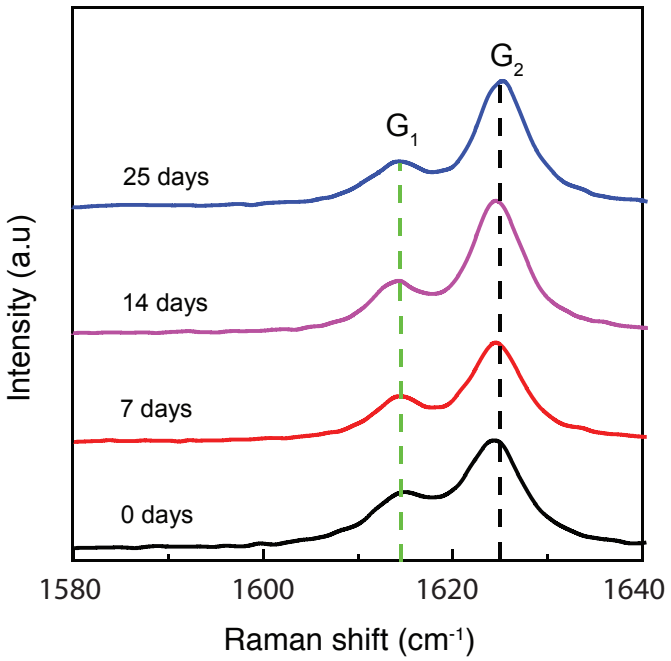

Figure 6.13: The Raman spectra of a $FeCl_3$ intercalated sample after exposure to humidity (>95%) for 0 to 25 days.

of the materials; for example, ITO has a resistivity of 7Ω/□ with a 550nm transmission of 75% for a thick film, where reducing the thickness increases the resistivity to 100Ω/□ with a 550nm transmission of 90%. Reducing the material thickness increases the 550nm transmission, but reduces the parallel conductance in the film hence increasing the resistivity, this leads to the bounding grey area highlighting the empirical dependence of resistivity on the 550nm transmission. In the comparison, the ideal transparent conductor would have a high optical transmission and low resistivity, hence tending to the bottom right corner of the graph. It is apparent that the resistivity and 550nm transmission of the 5-layer intercalated graphene outperforms the commercially available ITO films. Furthermore, the doped carbon nanotubes and doped monolayer graphene are poor performers, when compared to $FeCl_3$ intercalated graphene.

6.8 Conclusion

In conclusion, I have shown the successful functionalisation of few layer graphene through $FeCl_3$ intercalation, which is confirmed through Raman spectroscopy and electrical transport measurements. I demonstrated a significant reduction of the electrical resistivity of up to three orders of magnitude when $FeCl_3$ intercalated graphene is compared to the pristine analogue. I showed a small change in the optical transmission spectrum of graphene flakes after the intercalation procedure, where the optical transmission is still high enough to compete with commercially used ITO films. Finally, I also presented a systematic study of the stability of $FeCl_3$ intercalated few layer graphene, where I showed through Raman spectroscopy and electrical transport measurements no significant change for a long exposures to high levels of humidity and at temperatures of up to 150°C in atmosphere.

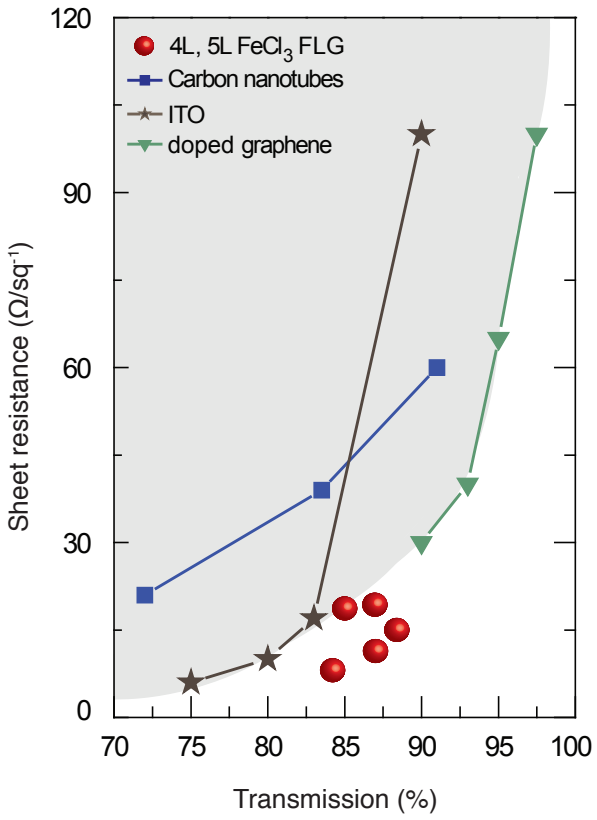

Figure 6.14: A plot comparing the 550nm transmission and sheet resistance of ITO to those of a range of carbon based conductors.

However, in this chapter, I only consider small flakes to demonstrate the properties of $FeCl_3$ intercalated few layer graphene. The limitations are clear, it would be impossible to create a 5 inch display for a mobile phone, using mechanically exfoliated and intercalated graphene flakes, that can commercially compete with ITO for scalability. This problem is addressed in the following chapter, where I extend the characterisation techniques and refine the intercalation and fabrication processes to increase the scalability of the $FeCl_3$ intercalation procedure.

Bibliography

[1] Kumar, A., et al. The race to replace tin-doped indium oxide: which material will win? *ACS Nano* **4**, 11-14 (2010).

[2] Hecht, D. S., et al. Emerging transparent electrodes based on thin films of carbon nanotubes, graphene, and metallic nanostructures. *Adv. Mater.* **23**, 1482 (2011).

[3] Nair, R. R., et al. Fine structure constant defines visual transparency of graphene. *Science* **320**, 1308 (2008).

[4] Bae, S., et al. Roll-to-roll production of 30-inch graphene films for transparent electrodes. *Nat. Nanotechnol.* **5**, 574 (2010).

[5] Lee, C., et al. Measurement of the elastic properties and intrinsic strength of monolayer graphene. *Science* **321**, 385 (2008).

[6] Kim, K. K., et al. Enhancing the conductivity of transparent graphene films via doping. *Nanotechnology* **21**, 285205 (2010).

[7] De, S., et al. Are there fundamental limitations on the sheet resistance and transmittance of thin graphene films? *ACS Nano* **4**, 2713 (2010).

[8] Dresselhaus, M. S., et al. Intercalation compounds of graphite. *Adv. Phys.* **51**, 1 (2002).

[9] Zhao, W., et al. Intercalation of few-layer graphite flakes with FeCl3: Raman determination of Fermi level, layer by layer decoupling, and stability. *J. Am. Chem. Soc.* **133**, 5941 (2011).

[10] Zhan, D., et al. FeCl3-Based Few-Layer Graphene Intercalation Compounds: Single Linear Dispersion Electronic Band Structure and Strong Charge Transfer Doping. *Adv. Func. Mat.* **20**, 3504 (2010).

[11] Howard, C. A., et al. Phonons in potassium-doped graphene: The effects of electron-phonon interactions, dimensionality, and adatom ordering. *Phys. Rev. B* **84**, 241404 (2011).

[12] Jung, N., et al. Optical reflectivity and Raman scattering in few-layer-thick graphene highly doped by K and Rb. *ACS Nano* **5**, 5708 (2011).

[13] Khrapach, I., et al. Novel Highly Conductive and Transparent Graphene-Based Conductors. *Adv. Mater.* **24**, 2844-2849 (2012).

[14] Song, Y., et al. Iron (III) Chloride doping of CVD graphene. *Nanotechnology* **25**, 395701 (2014).

[15] Hecht, D. S., et al. High conductivity transparent carbon nanotube films deposited from superacid. *Nanotechnology* **22**, 075201 (2011).

Chapter 7

Functionalising large area few layer epitaxial graphene for transparent electrodes

7.1 Introduction

As demonstrated in the previous chapter, the electrical properties of graphene flakes can be modified through $FeCl_3$ intercalation. However, to make $FeCl_3$ intercalated graphene viable for next generation electrical applications, the producible sample size needs to be significantly increased. One approach is to use few layer graphene grown on silicon carbide (4H-SiC) [1]. This method of growth produces high quality films with little variation in the number of layers grown and is combined with a substrate which is compatible with the $FeCl_3$ intercalation procedure. In this chapter, I demonstrate the $FeCl_3$ intercalation of trilayer graphene grown on 4H-SiC through Raman spectroscopy, large area room temperature and microscopic cryogenic transport techniques.

7.2 Intercalating few layer epitaxial graphene

Epitaxial few layer graphene was obtained through the thermal decomposition of Si face of a 4H-SiC silicon carbide substrate. The C face was cleaned of any graphene present using plasma etching. The sample was then intercalated with $FeCl_3$ for 24 hours using the procedure outlined in Section 3.4.

7.2.1 Raman identification

First, I characterised the Raman spectra of the few layer epitaxial graphene to determine the number of layers. Figure 7.1 shows the G and 2D peaks, after subtracting the SiC Raman background, of the pristine sample. I observed a G peak and a multipeak structure of the 2D peak. This indicates that the sample is not monolayer[2]. It has been shown that for few layer graphene grown on SiC, the FWHM of the 2D peak

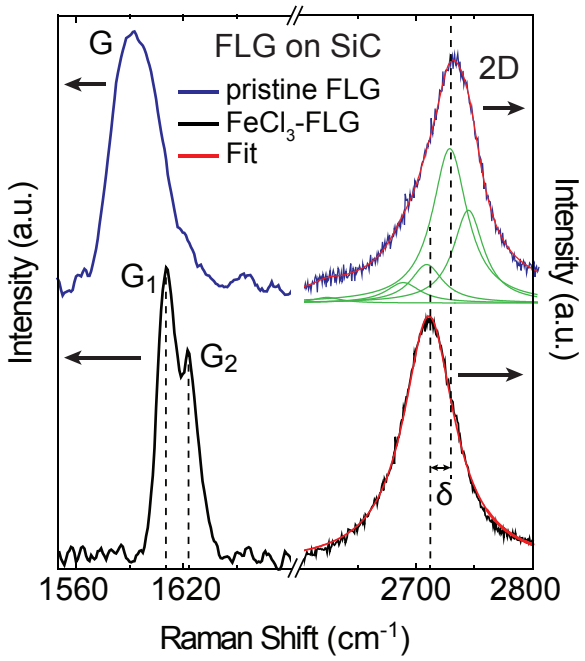

Figure 7.1: The top spectrum shows the pristine trilayer graphene G and 2D peaks, where fitting the 2D peak gives the number of layers of the graphene film. The bottom spectra shows the spectra after the intercalation process including an upshifted G peak to the G_1 and G_2 peak positions and a single peaked 2D peak.

exhibits a linear dependence on the inverse number of layers (N). FWHM(2D) = (-45(1/N)+88)[cm^{-1}][3]. The 2D peak measured in the sample has a FWHM of 72cm^{-1}, from which I estimate a layer number of 3.

Upon the intercalation with $FeCl_3$, the G peak upshifts to the G_1 and G_2 peak positions, 1610cm^{-1} and 1624cm^{-1} respectively[4, 5]. This is a demonstration of the intercalation of $FeCl_3$ molecules into the epitaxial few layer graphene. At the same time, the 2D band structure of the few layer graphene on SiC is changed from a multi peak structure to that of a single Lorentzian and the 2D peak position downshifts to that of monolayer graphene on 4H-SiC ($\approx$ 2715cm^{-1})[3]. These observations demonstrate that the $FeCl_3$ intercalated few layer graphene on SiC has three graphene sheets and two $FeCl_3$ layers intercalated between the graphene sheets.

7.2.2 Large area transport measurements of intercalated epitaxial graphene

The sheet resistance of the as grown epitaxial few layer graphene and $FeCl_3$ intercalated few layer graphene was measured in a four terminal configuration in macroscopic samples, with a conductive channel of fixed width (0.7cm) and channel length ranging from 0.7 to 4.2 mm using Ti/Au (5/50 nm) contacts. Figure 7.2 shows that the pristine epitaxial graphene has an average sheet resistance of (174 $\pm$ 9)$\Omega/\square$, estimated from the linear fit. The corresponding values of resistance in the same devices after intercalation with $FeCl_3$ are systematically lower with an average value of (16.6 $\pm$ 0.6)$\Omega/\square$.

The distribution of sheet resistance of pristine and $FeCl_3$ intercalated graphene are presented as two histograms, shown in Figure 7.3. In both cases, I found a single peaked distribution with narrow spreading of the sheet resistivity demonstrating the

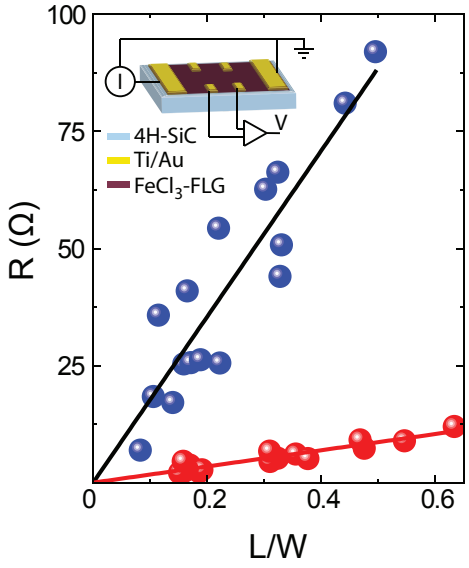

Figure 7.2: Longitudinal resistance plotted against the aspect ratio of the device, where L is the sample length and W is the width of the current channel (0.7cm). The blue points are for pristine trilayer graphene, the red points are for intercalated trilayer graphene, where the fitted linear gradients represents the large area resistivity. The inset describes the device geometry and measurement circuit. Error bars are smaller than the size of the data points

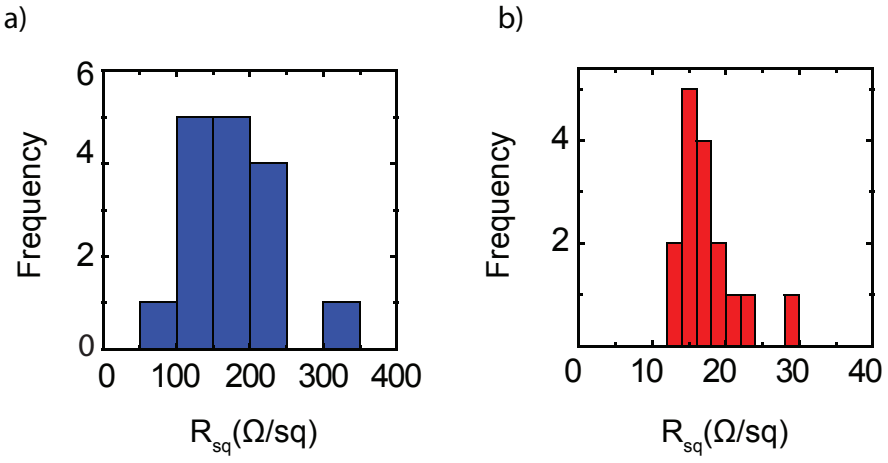

Figure 7.3: a) Distribution of the measured large area resisitvities for pristine trilayer graphene, b) distribution of the measured large area resistivities for intercalated trilayer graphene.

homogeneous and reproducible electrical properties in large area $FeCl_3$ intercalated graphene.

7.3 Characterising the electrical properties of intercalated epitaxial graphene

The charge carrier sign and concentration are readily characterised from measurements of the Hall resistance in Hall bar devices, shown in the inset of Figure 7.4. The positive slope of the Hall resistance with respect to applied field indicates that the dominant charge carriers are holes with a concentration of $n > 1.5\times10^{14}$ cm^{-2}. The charge carrier concentration far exceeds the values achievable with top-gates on SiC[6] and is comparable to that achieved in electric double layer few layer graphene transistors[7].

Measurements of the temperature dependence of the longitudinal resistivity ρ_{xx}

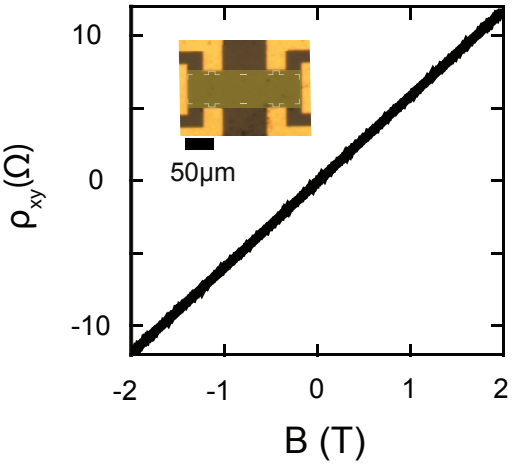

Figure 7.4: The Hall resistance plotted against the applied perpendicular magnetic field, at a temperature of 1K, for $FeCl_3$ intercalated trilayer graphene. The inset shows the device geometry.

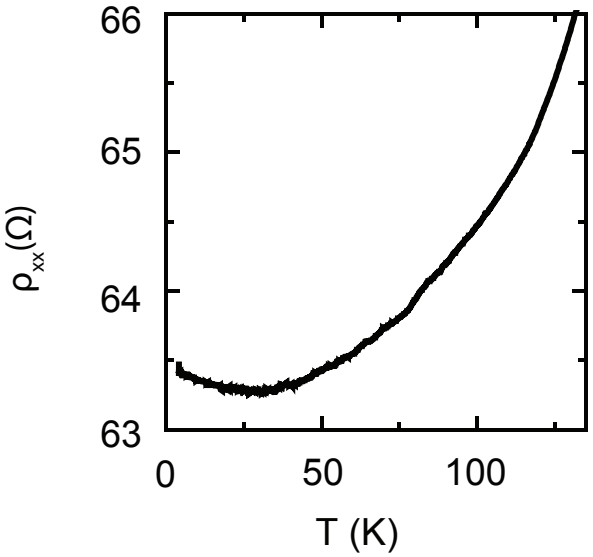

Figure 7.5: The measured temperature dependence with respect to longitudinal resistivity for the $FeCl_3$ intercalated graphene device shown in the inset of Figure 7.4.

show that this decreases monotonously from 175K down to 25K as expected for heavily doped graphene[8], as shown in Figure 7.4. However, at temperatures below 25K, there is an increase in ρ_{xx} that was not previously observed in $FeCl_3$ intercalated graphene flakes and whose quantum nature can only be unveiled with a detailed study of the magnetic field dependence.

7.4 Magneto-resistance in intercalated graphene

Figure 7.6 shows the results of a measurement of ρ_{xx}(B) performed at a temperature of T = 1K. A zero-field peak characteristic of weak localisation is clearly visible[9]. As the magnetic field breaks time reversal symmetry, the quantum interference and a classical magneto-resistive signal are observed ($|B| > 250$ mT). Due to the size of the sample of the Hall bars, I can directly measure the weak localisation signal without any need for subtracting any mesoscopic conductance fluctuations typically present in mechanically exfoliated pristine graphene[9].

A detailed study of the temperature dependence of the longitudinal magneto-resistivity shows that the weak localisation peak is heavily suppressed when the temperature increases, as shown in Figure 7.7. At the same time for larger fields ($|B| > 250$ mT), the concavity of the parabolic shape background of ρ_{xx} verus B is clearly temperature independent. Recent experiments have shown that the longitudinal magneto-resistance can be understood as the sum of a Drude term plus a correction due to the electron-electron interaction[10]. The signature of the electron-electron interaction is a strong temperature dependence of the concavity of ρ_{xx}. However, there is no observable change in the concavity or sign of the parabola, indicating that the magneto-resistance is described by the classical Drude term.

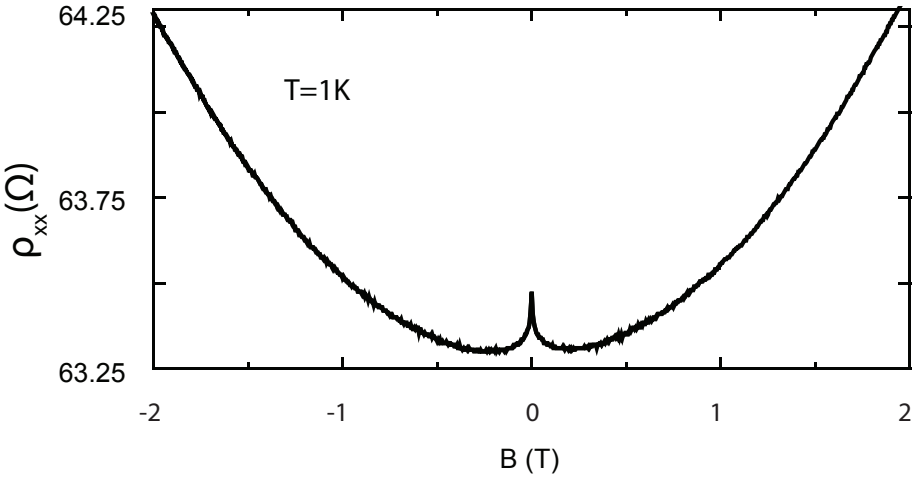

Figure 7.6: The measured longitudinal resistivity at 1K with respect to applied perpendicular magnetic field for $FeCl_3$ intercalated graphene.

I can describe accurately the experimental data using the equivalent magneto-resistance for three parallel hole gases with similar carrier concentrations, as previously identified with Raman spectroscopy. To analyse the weak localisation signal, I subtracted the classical magneto-resistance background by fitting a classical parabolic field dependence.

7.5 Weak localisation in intercalated graphene

Figure 7.8 shows the measured weak localisation signal extracted from the longitudinal magneto-resistivity after subtracting the classical background and the corresponding best fit of the total magneto-conductance modelled with the parallel of three decoupled hole gases for different temperatures. I considered the equivalent magneto-conductance for the intercalated few layer graphene to be $\Delta\sigma = \sum_{j=1}^{3} \Delta\sigma_j$, where $\Delta\sigma_j$ is that well

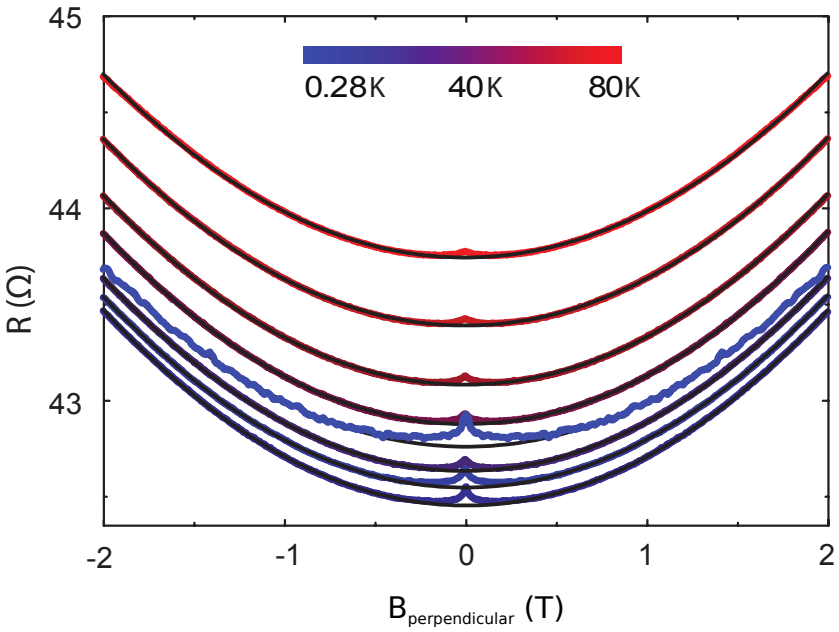

Figure 7.7: The measured longitudinal resistivity with respect to perpendicular magnetic field for a temperature range between 280mK and 80K. The black lines indicate a parabolic fit of the data under the condition $|B| > 250$mT.

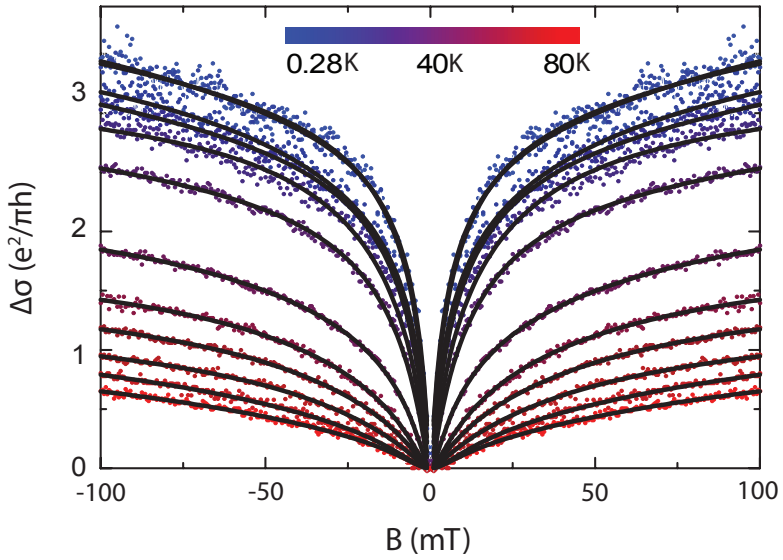

Figure 7.8: A plot of the change in longitudinal conductance due to weak localisation plotted against perpendicular magnetic field from 280mK to 80K. The black lines are the fit of the data to Equation 7.1.

established magneto-conductance for monolayer graphene, described in Section 2.2.2.

$$\Delta\sigma_j(B) = \frac{e^2}{\pi h}\left[F\left(\frac{B_j}{B_{j,\phi}}\right) - F\left(\frac{B_j}{B_{j,\phi}+2B_{j,i}}\right) - 2F\left(\frac{B_j}{B_{j,\phi}+B_{j,i}+B_{j,\star}}\right)\right] \quad (7.1)$$

At T = 280 mK, the best fit values for the middle hole gas with higher charge carrier concentration are $B_i = (7.4 \pm 0.6) \times 10^{-4}$T and $B_\phi = (1.2 \pm 0.2) \times 10^{-4}$T and for the outer hole gases with lower charge density $B_i = (4.6 \pm 5) \times 10^{-3}$T and $B_\phi = (1.6 \pm 3) \times 10^{-3}$T. In the fitting procedure, the term containing $B_\star$ is large with respect to B_i and B_ϕ, stemming from the very short $\tau_\star$ compared to the other characteristic times (τ_i and τ_ϕ). Furthermore, τ_i is independent of temperature and is assumed to be the same for all of the fits of the magneto-conductance. This leaves τ_ϕ as a free fitting parameter for the magneto-conductance peaks.

If I assume an identical diffusion constant for each hole gas, I can estimate the value of τ_ϕ at each temperature. When I plot τ_ϕ for two representative samples with respect to measurement temperature, I observe two different regimes, highlighted by plotting the data in a log-log plot, shown in Figure 7.9. For temperatures above 4 K, I observed a rapid decrease in the dephasing time and for temperatures below 4 K, there is a saturation in the dephasing time. Although this saturation is observed in pristine graphene samples, which is attributed to magnetic impurities in microscopic concentrations, it typically occurs at lower temperatures[11]. In this case, the presence of iron in the intercalant species is attributed to as the source of the saturation in dephasing time[12].

The dephasing length (L_ϕ) can be extracted from the parameter B_ϕ using the relation $L_\phi = (D\tau_\phi)^{1/2}$, which gives $B_\phi = \hbar/(4eL_\phi^2)$. Therefore, without making any

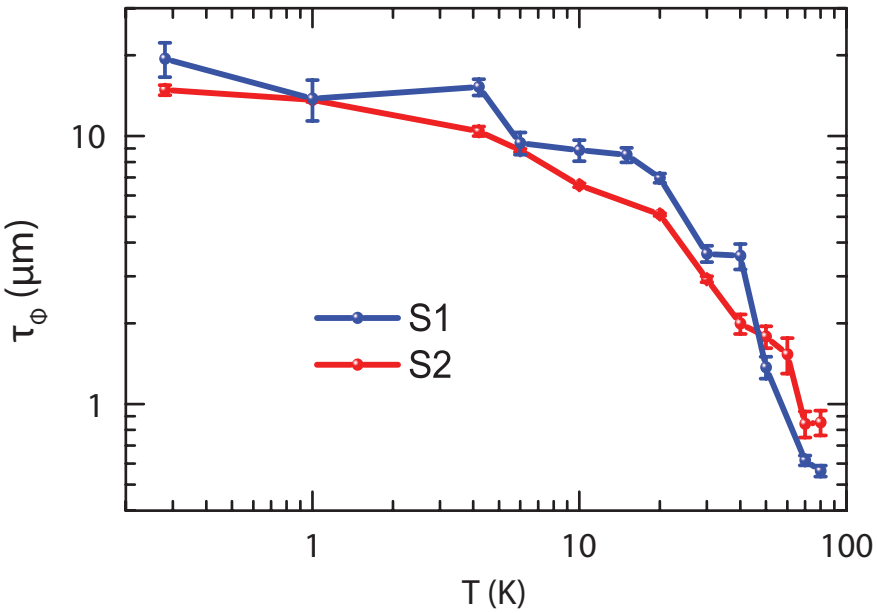

Figure 7.9: A plot showing the estimated τ_ϕ with respect to temperature for two different samples.

assumption in the diffusion constant of the hole gases, I extracted the corresponding values of L_ϕ for a wide range of temperatures (80 K to 280mk), as shown in Figure 7.10. Upon lowering the temperature, the values of L_ϕ estimated for $FeCl_3$ intercalated epitaxial few layer graphene increase monotonically; however below 4 K the increase of L_ϕ is less pronounced with a maximum value of $L_\phi = 1.17$ μm at 280 mK. To understand the possible origin of the temperature dependence of L_ϕ in the material, I compared L_ϕ(T) for two representative samples (Labeled S1 and S2) with values measured in pristine mechanically exfoliated[9], pristine epitaxial[10, 11] and CVD graphene[13], as shown in Figure 7.10. The overall temperature dependence of L_ϕ is similar for all kinds of graphene, however there are two striking features that separate the intercalated graphene from the pristine graphene. The intercalated graphene has a higher L_ϕ than the pristine graphene at any give temperature and L_ϕ decreases rapidly only for

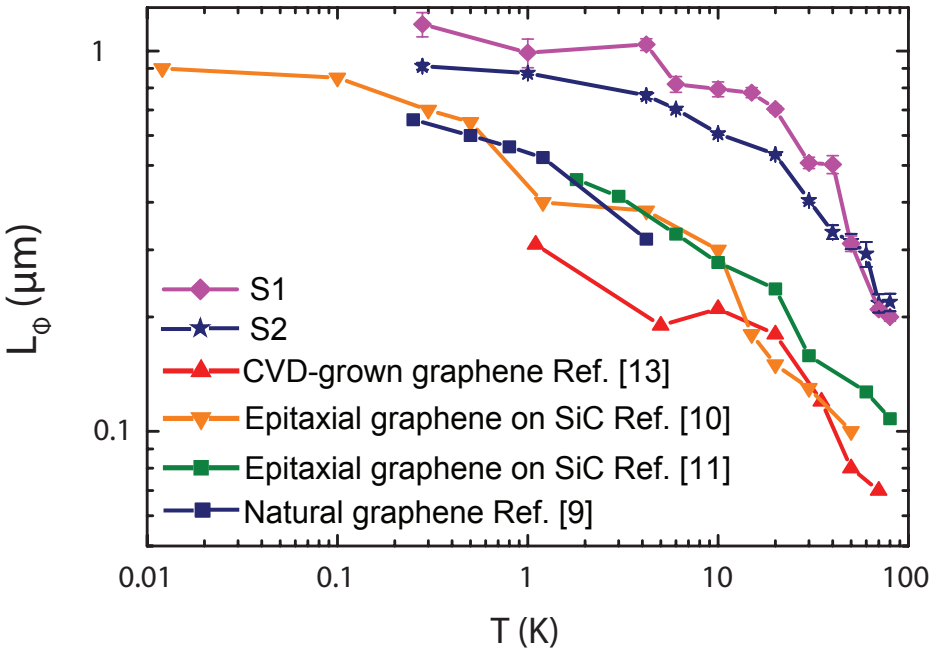

Figure 7.10: A plot showing the estimated dephasing length (L_ϕ) with respect to temperature for two different samples. For comparison, there are four other studies included which use CVD graphene[13], epitaxial graphene[10, 11] and natural graphene[9].

temperatures much higher than what is observed in pristine graphene.

The origin of the < 4 K saturation of L_ϕ is unclear, although it occurs at a temperature where a magnetic phase transition is reported in bulk $FeCl_3$ stage one intercalated graphite[14], which would explain the absence of this effect in the pristine graphene samples. However, without further transport measurements I only conjectured that this is the origin of the saturation at 4 K.

7.6 Conclusion

In conclusion, I have demonstrated the successful intercalation of large area epitaxial graphene grown on 4H-SiC with $FeCl_3$, through Raman spectroscopy. I found that this material has a very low square resistance ($\approx 16\Omega/\square$) becoming an ideal candidate for transparent electrodes in novel complementary applications targeted by SiC-based electronics. With a detailed study of the Raman spectra, I have characterised the structure of this material. Finally, I conducted a systematic study of the magnetoresistance in Hall bar devices and I have estimated a larger dephasing length reported in pristine graphene at any temperature in the range 280 mk $<$ T $<$ 80 K, with $L_\phi \approx$ 1.2 μm at 280 mK.

Bibliography

[1] Eriksson, J., et al. The influence of substrate morphology on thickness uniformity and unintentional doping of epitaxial graphene on SiC. *Appl. Phys. Lett.* **100**, 241607 (2012).

[2] Ferrari, A. C., et al. Raman Spectrum of Graphene and Graphene Layers. *Phys. Rev. Lett.* **97**, 187401 (2006).

[3] Lee, D. S., el al. Raman spectra of epitaxial graphene on SiC and of epitaxial graphene transferred to SiO2. *Nano Lett.* **8**, 4320 (2008).

[4] Zhao, W., et al. Intercalation of few-layer graphite flakes with FeCl3: Raman determination of Fermi level, layer by layer decoupling, and stability. *J. Am. Chem. Soc.* **133**, 5941 (2011).

[5] Zhan, D., et al. FeCl3-Based Few-Layer Graphene Intercalation Compounds: Single Linear Dispersion Electronic Band Structure and Strong Charge Transfer Doping. *Adv. Func. Mat.* **20**, 3504 (2010).

[6] Wu, Y., et al. Top-gated graphene field-effect-transistors formed by decomposition of SiC. *Appl. Phys. Lett.* **92**, 092102 (2008).

[7] Uesugi, E., et al. Electric double-layer capacitance between an ionic liquid and few-layer graphene. *Sci. Rep.* **3**, 1595 (2013).

[8] Khrapach, I., et al. Novel Highly Conductive and Transparent Graphene-Based Conductors. *Adv. Mater.* **24**, 2844-2849 (2012).

[9] Tikhonenko, F. V., et al. Weak Localization in Graphene Flakes. *Phys. Rev. Lett.* **100**, 056802 (2008).

[10] Jobst, J., et al. Electron-Electron Interaction in the Magnetoresistance of Graphene .*Phys. Rev. Lett.* **108**, 106601 (2012).

[11] Lara-Avila, S., et al. Disordered Fermi liquid in epitaxial graphene from quantum transport measurements. *Phys. Rev. Lett.* **107**, 166602 (2011).

[12] Bointon, T. H., et al. Approaching Magnetic Ordering in Graphene Materials by $FeCl_3$ Intercalation. *Nano Lett.* **14**, 1751-1755 (2014).

[13] Cao, H., et al. Electronic transport in chemical vapor deposited graphene synthesized on Cu: Quantum Hall effect and weak localization. *Appl. Phys. Lett.* **96**, 122106 (2010).

[14] Dresselhaus, G., et al. Magnetism in Graphite intercalation compounds. *NATO ASI series* **148**, 407-424 (1986).

Chapter 8

Functionalising large area few layer graphene grown on nickel substrates for transparent electrodes

8.1 Introduction

The development of flexible photovoltaic and light emitting devices depend on the availability and compatibility between flexible and transparent electrodes and photoactive materials[1]. Furthermore, the diffusion of ITO into the photoactive layers of photovoltaic (PV) or organic light emitting diode (OLED) is also a well-known cause of device degradation[2]. Meshes of metallic nanowires are emerging as an attractive alternative, since they have high optical transmission ($\approx 80\%$ at 550nm) and low sheet resistivity (38 $\Omega/\square$) even when subject to 16% strain[3]. However, scattering of light off nanowires can introduce significant optical haze, limiting the range of applications for which these materials are suitable. Graphene, as shown in Chapter 5, is an emerging contender for future flexible electronics as the conductance remains unchanged even when subjected to strains of 6.2%[4] and does not form haze as it is a continuous film. However, the high sheet resistivity sets an upper limit to the maximum transparent electrode area. The potential drop across the transparent electrode increases with area, resulting in a voltage gradient hence a non uniform light emission from OLED devices or other light emitting devices.

So far my search for the best suitable transparent and flexible conductor has addressed $FeCl_3$ intercalated flakes, which are limited in viability by sample size, and $FeCl_3$ intercalated large area epitaxial graphene, which is limited by a rigid SIC substrate.

In this chapter, I show that large area $FeCl_3$ intercalated few layer CVD graphene exhibits a macroscopic low resistivity of 20.52 $\Omega/\square$ and high optical transmission of 77% at 550nm, which is comparable to 10 μm thick ITO. Furthermore, I demonstrate the success of the large intercalation of $FeCl_3$ through Raman spectroscopy for a $1cm^2$

sample on SiO_2/Si substrate. Finally, I demonstrate a novel transfer process where $FeCl_3$ intercalated few layer graphene can be transferred onto arbitrary substrates.

8.2 Fabrication of $FeCl_3$ intercalated graphene grown on nickel substrates

Large a few layer graphene grown on silicon supported nickel film was purchased from Graphene Square. It was transferred to glass and SiO_2/Si substrates using the PMMA supported wet etch transfer, described in Section 3.2.3, in a 1M $FeCl_3$ solution. The films were subsequently transferred to ultrapure water, to a concentrated HCl solution for 1 hour and rinsed in ultrapure water[5]. Finally the film of PMMA and few layer graphene were transferred to a glass or SiO_2/Si substrate and, after 24 hours, the PMMA was removed with acetone/IPA. The samples where intercalated using the two zone vapour transport method discussed in Section 3.4.

8.3 Raman spectroscopy

Figure 8.1 shows two representative spectra of the resulting intercalation of $FeCl_3$ into a few layer region of the graphene film. There are two different regimes observed. Firstly, there is an underlying uniform thin graphene film which shows no intercalation (Figure 8.1a). Secondly, there are multilayer graphene islands on top of the continuous film which show the distinctive G_1 and G_2 bands, which occur at 1610cm and 1624cm^{-1} respectively. Furthermore, for this regime the few layer graphene layers are decoupled due to the adjacent $FeCl_3$ layers; this manifests as a change from the multipeak to a single peak, as shown in Figure 8.1b. These factors demonstrate the intercalation of the

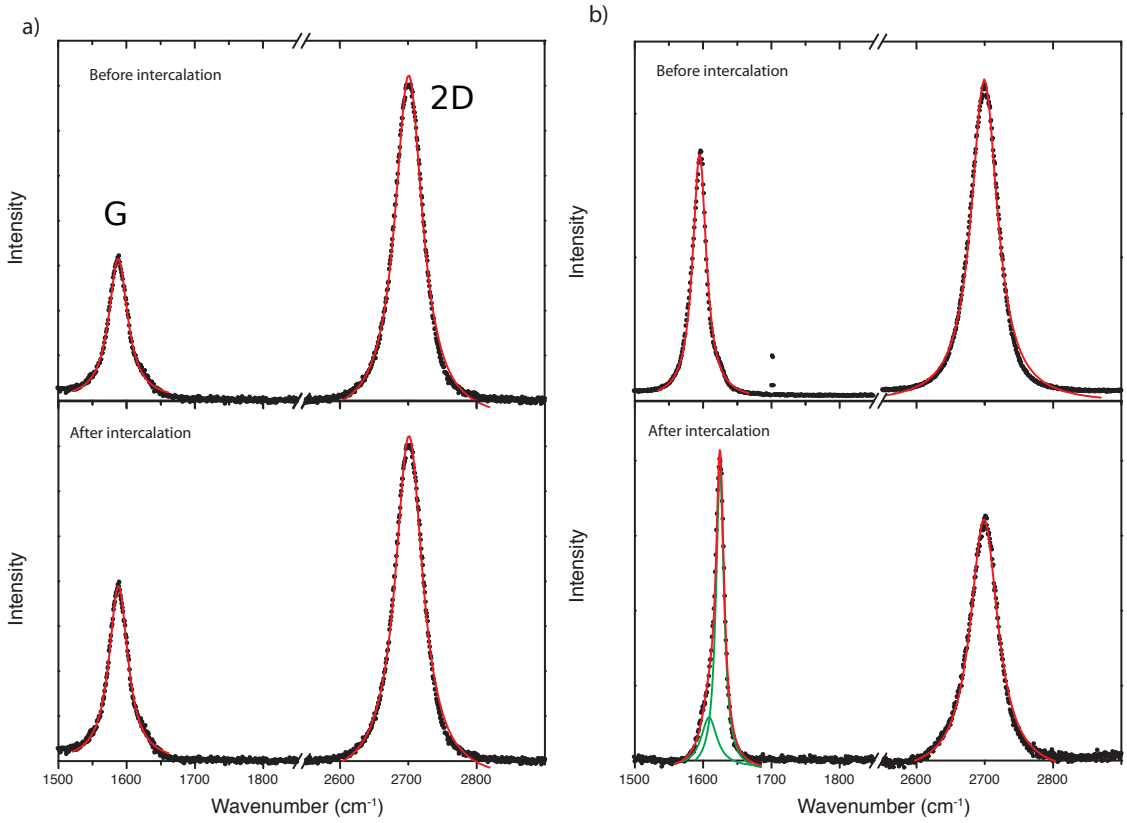

Figure 8.1: a) Raman spectrum for a thin region of graphene before (Top) and after (Bottom) the intercalation process, b) Raman spectrum for a few layer island of graphene before (Top) and after (Bottom) the intercalation process.

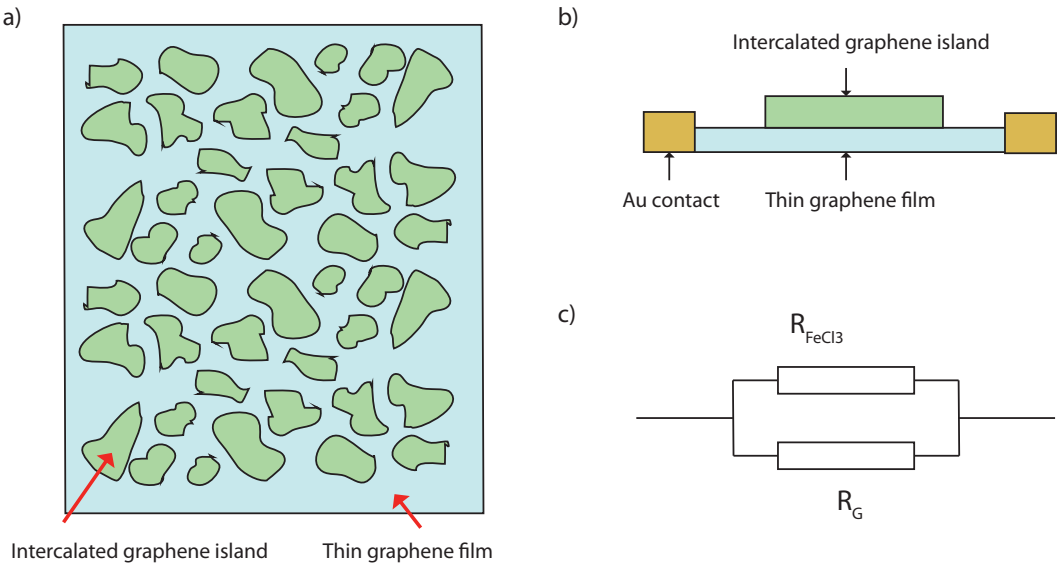

Figure 8.2: a) An illustration of the $FeCl_3$ intercalated graphene islands on a thin film of not intercalated graphene, b) a schematic of the cross section through the film showing the parallel conduction and c) the equivalent circuit diagram of b) where R_G is the resistance of the graphene under layer and R_{FeCl3} is the resistance through the intercalated multilayer graphene.

some of the regions probed with the excitation laser. To understand the effect of these intercalated regions on the electrical performance of the film, transport measurements were performed.

8.4 Large area transport measurements

The four terminal resistance was used to probe the effect of the intercalation and determine if there is low sample resistivity of the islands of $FeCl_3$ intercalated few layer graphene shorting the underlying graphene film illustrated in Figure 8.2.

The sample resistance was measured with respect to the device aspect ratio, using a channel width of 1 cm and length ranging from 1.5 to 6 mm. Figure 8.3 shows

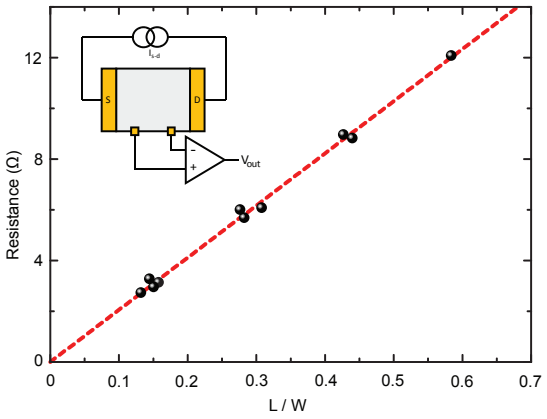

Figure 8.3: A graph showing the measured resistance (R) of an $FeCl_3$ intercalated few layer graphene film plotted against the aspect ratio (L/W), where the dashed gradient is representative of the resistivity. The inset shows the measurement circuit.

the measured sample resistance plotted against the aspect ratio of the device, where the average sheet resistance is determined to be 20.52 ± 0.48 Ω/□. Furthermore, the strong correlation between the resistance and the aspect ratio confirms that the sample is uniformly doped on a macroscopic scale.

8.5 Optical transmission

I measured the optical transmission of $FeCl_3$ intercalated few layer graphene grown on a nickel substrate transferred onto glass. Figure 8.4 shows the optical transmission over the range of light wavelengths from 450 to 850nm. Similarly to the $FeCl_3$ intercalated mechanically exfoliated flakes, a high optical transmission is observed from 74% at 450nm increasing monotonously to 88% for 850nm, where the 550nm transmission is 77%.

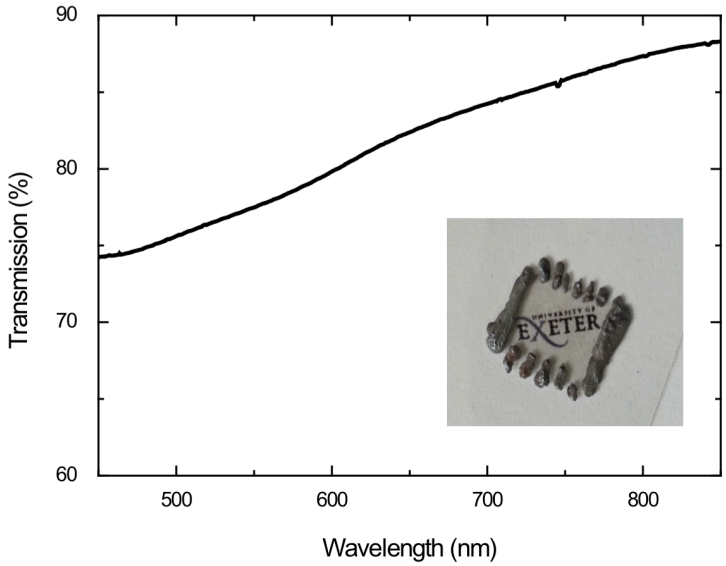

Figure 8.4: The optical transmission of the $FeCl_3$ intercalated few layer graphene film from 450 to 850nm. The inset shows the $FeCl_3$ intercalated graphene on glass.

8.6 Intercalated graphene grown on nickel as a transparent conductor

It is clear that the large area $FeCl_3$ intercalation of the multilayer graphene gives significantly reduced resistivity, as with the mechanically exfoliated[8] and epitaxial analogues[7]. However, the resistivity of 20.52 $\Omega/\square$ is still larger than the desired 10 $\Omega/\square$ of ITO. The optical transmission is also high, with a value of 550 nm, but is still below that of ITO, 80% at 550 nm[6]. Although these values underperform by a small margin with respect to ITO, these parameters do not exclusively affect the viability of a transparent conductor. For example, the production of ITO requires indium, a rare earth metal, making the price increase due to increasing demand and a finite supply[9]. The materials required for the production of multilayer graphene and the intercalation process (hydrogen,methane, nickel and $FeCl_3$) however are all abundant giving sustainability in production costs and capacity.

8.7 Transfer to of $FeCl_3$ intercalated graphene to arbitrary substrates

The correct choice of the substrate used for the intercalation process depends on the tolerance of the substrate to the intercalation temperatures (360°C), exposure to high temperature $FeCl_3$ vapours and Cl_2 gas. Materials such as glass and silicon wafer are stable to temperatures up and beyond the intercalation temperature and do not react with $FeCl_3$ or Cl_2, making them suitable for the intercalation process; however they are rigid. Plastic substrates, on the other hand, are flexible and cheap to produce, but they

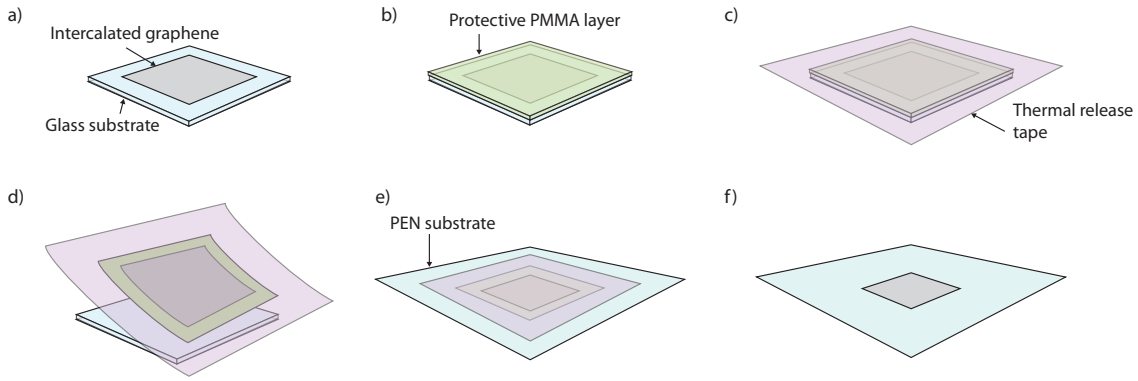

Figure 8.5: A schematic showing the transfer of $FeCl_3$ intercalated graphene onto arbitrary substrates. a) $FeCl_3$ intercalated graphene on a glass substrate, b) PMMA spun coated on the substrate, c) thermal release tape is applied and the PMMA and $FeCl_3$ intercalated graphene were pealed off the glass substrate, d) the thermal release tape was applied to a PEN substrate, e) the thermal release tape was heated and removed, then the PMMA was removed using acetone and IPA.

do not tolerate the extreme conditions of the intercalation process. I have developed a method which combines both substrates; first I intercalate the few layer graphene on a glass substrate, spin coat PMMA and attach to thermal release tape. I then peeled the thermal release tape off the substrate with the intercalated film attached to the tape and then released the film onto a plastic substrate using heat. This process is shown in Figure 8.5a-e.

8.8 Conduction on flexible substrates

To demonstrate the conduction of the transferred film the sample was tested as a component in a simple circuit. Contacts were attached to the sample using silver paint and put in series with a battery, LED and 1KΩ resistor. Figure 8.6a shows the LED illuminated when the circuit is complete. Furthermore, removing the resistor,

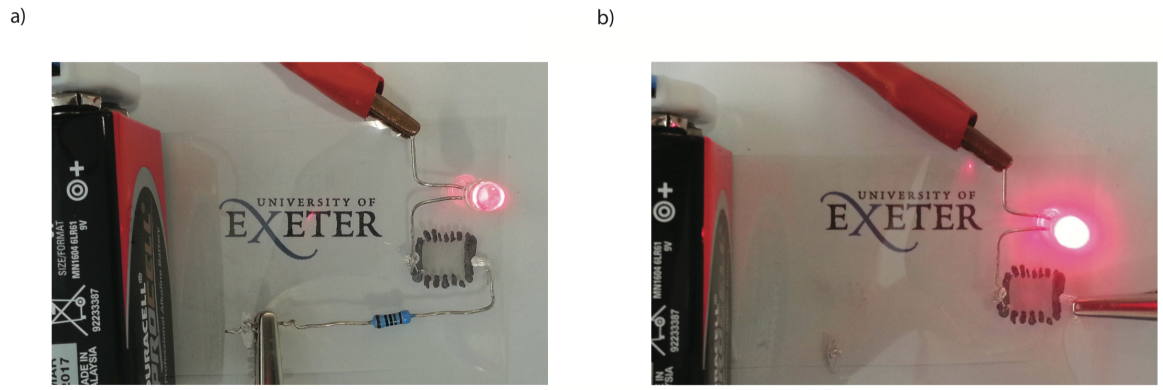

Figure 8.6: a) A photograph showing the series circuit of a 9V battery, an LED, the transferred intercalated film and a resistor, b) the same circuit with the resistor removed.

Figure 8.6b shows a brighter illumination of the LED. The resistor is clearly limiting the current flowing through the LED, demonstrating that the sample has a resistivity much lower than that of the 1KΩ resistor.

Finally, Figure 8.7 shows the transferred film conducting while the substrate is deformed by flexing.

8.9 Conclusion

In conclusion, the intercalation of large area multilayer graphene has been demonstrated through Raman spectroscopy and large area transport measurements. The lower resistivity and high optical transmission were observed over a large area and is comparable to that of ITO as a transparent electrode. Futhermore, the abundance of production materials gives $FeCl_3$ intercalated graphene the stability in price and capacity compared to that of ITO.

As an extension to the $FeCl_3$ intercalation of large area graphene, I also demonstrated a novel transfer technique to overcome the issue of producing $FeCl_3$ intercalated

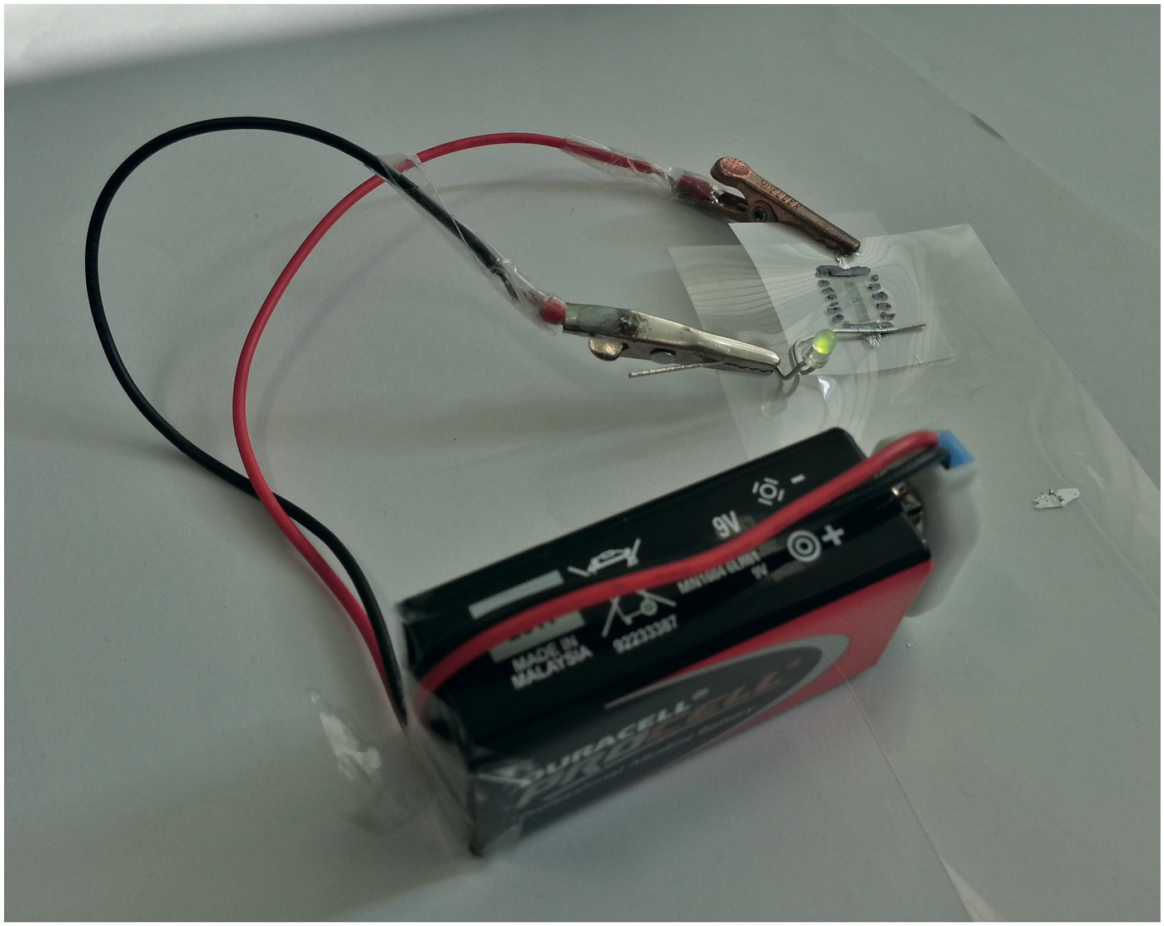

Figure 8.7: A photograph showing the film conducting while the substrate is flexed.

graphene on substrates not compatible with the intercalation process. Finally, the conductivity of the transferred sample was demonstrated by illuminating an LED.

Bibliography

[1] Hancox, I., et al. Optimization of a High Work Function Solution Processed Vanadium Oxide Hole-Extracting Layer for Small Molecule and Polymer Organic Photovoltaic Cells. *J. Phys. Chem.* **117**, 49-57 (2013).

[2] Wu, J., et al. Organic Light-Emitting Diodes on Solution-Processed Graphene Transparent Electrodes. *ACS Nano.* **4**, 43-48 (2010).

[3] Yu, Z., et al. Highly Flexible Silver Nanowire Electrodes for Shape-Memory Polymer Light-Emitting Diodes. *Adv. Matter.* **23**, 664-668 (2010).

[4] Verma, V. P., et al. Large-area graphene on polymer film for flexible and transparent anode in field emission device. *Appl. Phys. Lett.* **96**, 203108 (2010).

[5] Park, H. J., et al. Growth and properties of few-layer graphene prepared by chemical vapor deposition. *Carbon* **48**, 1088-1094 (2010).

[6] De, S., et al. Are there fundamental limitations on the sheet resistance and transmittance of thin graphene films? *ACS Nano* **4**, 2713 (2010).

[7] Bointon, T. H., et al. Approaching Magnetic Ordering in Graphene Materials by $FeCl_3$ Intercalation. *Nano Lett.* **14**, 1751-1755 (2014).

[8] Khrapach, I., et al. Novel Highly Conductive and Transparent Graphene?Based Conductors. *Func. Matter.*, **24**, 2844-2849 (2012).

[9] Gordon, R. G., et al. Criteria for choosing Transparent Conductors. *MRS Bulletin* **25**, 52-57 (2000).

Chapter 9

Conclusion

The overall aim of this thesis is to investigate the use of graphene for flexible and optoelectronic applications.

The first objective was to investigate alternative methods of large area graphene growth with the aim of reducing the manufacturing costs, while maintaining the quality required for graphene human interface devices. In Chapter 4, I described the growth of graphene in a cold walled furnace, then using Raman spectroscopy, SEM and AFM I optimised the growth process. I was able to produce high quality graphene devices with charge carrier mobilites of 3300 $cm^2/(Vs)$ which showed clear QHE features at relatively low magnetic fields of 5T. Finally, I demonstrated that the new process produces high quality graphene, while reducing the cost of producing CVD graphene as much as 99.89%.

The second objective was to develop new fabrication methods for the production of large area graphene devices, which are flexible and transparent. In Chapter 5, I presented a novel fabrication technique for large area graphene touch sensor, which can detect touch using both mutual- and self-capacitance. Furthermore, I demonstrated

that this novel fabrication technique could be used to create structures where other fabrication techniques were previously limiting the development of flexible graphene electronics, which is both flexible and durable. Finally, I demonstrated that graphene is indeed a suitable electrode material for flexible capacitive touch sensors, proved by a prototype device.

The third objective was to demonstrate that through functionalisation of graphene the electrical resistivity can be significantly reduced, while maintaining the high stability and optical transmission of graphene. In Chapter 6, I demonstrated the intercalation of $FeCl_3$ molecules between the layers of graphene which was confirmed using Raman spectroscopy and Hall effect transport measurements. The doping of the graphene reduces the resistivity by three orders of magnitude to $8\Omega/\square$, while maintaining the high optical transmission. Finally, I demonstrated the stability of the $FeCl_3$ intercalated graphene by measuring the Raman spectra and electrical transport properties over a range of high humidity and high temperature environments. In all cases, I found no change in the properties of the $FeCl_3$ intercalated graphene flakes.

The final objective was to investigate the upscaling of the $FeCl_3$ intercalation process of multilayer graphene over a large area, for the development of transparent electrodes that are flexible and low resistance. In Chapter 7, I demonstrated the intercalation of multilayer graphene grown on a 4H-SiC substrate using complementary Raman spectroscopy and electrical transport techniques. Furthermore, I conducted a systematic study of the magneto-resistance in Hall bar devices and I have estimated a larger dephasing length in pristine graphene at any temperature in the range 280 mk $<$ T $<$ 80 K, with $L_\phi \approx 1.2$ μm at 280 mK. In Chapter 8, I demonstrated the successful intercalation of large area multilayer graphene grown on a nickel substrate through Raman spectroscopy and large area electrical transport measurements. The lower resistivity

($20\Omega/\square$) and high optical transmission (>77%) were observed over a large area and are comparable to those of ITO as a transparent electrode.

As an extension, I also demonstrated a novel transfer technique to overcome the issue of producing $FeCl_3$ intercalated graphene on arbitrary substrate. Finally, I showed an example of the low resistivity and flexibility of $FeCl_3$ intercalated graphene transferred onto a plastic substrate by illuminating an LED.

In conclusion to this thesis, the work I performed has demonstrated that graphene is a viable and cost effective alternative to ITO for flexible electrode to be used in touch screens. Finally, I also showed that $FeCl_3$ functionalised graphene is a real contender as an electrode for the next generation of flexible photovoltaic and light-emitting devices.

Chapter 10

Appendix

10.1 Appendix A - Estimating the cost of producing CVD graphene

To compare the diverse range of CVD growth recipes I assume; all processes produce 1cm^2 of graphene; the cost of electricity in per kWH is £0.1352 and a MTI 1200X-5L hot walled furnace is used. I focus on three aspects of the process to provide my estimate. First, I consider the cost of copper foil used for growth. Taking the cost of 25 μm thick, 2.5 cm x 100 cm foil, with 99.999% pure copper from Alfa Aesar to be £88.20, I estimate the cost of the copper foil to be £0.3528 per square cm[1].

Secondly, I consider the total energy cost of graphene production. For an MTI 1200X-5L hot walled furnace, the power consumption is assumed to be at maximum during the ramping to the growth temperature (6kW) and that the power consumption scales linearly with temperature to a maximum of 6kW at 1200°C. For a growth temperature of 1000°C, the power consumption is estimated to be 5.175kW[2]. I included

Gas Type	Purity	Cost(£)	Volume(m^3)	Cost per Volume(£/m^3)
Hydrogen	N = 5.5	276.12[5]	8.8	31.37
Methane	N = 5.5	889.97[5]	10	88.99
Argon	N = 6	339.43[5]	10.6	32.02

Table 10.1: The estimation for cost of each different growth gas in £per cubic meter (m^3).

an article where the sample space is heated by a plasma, for which the power consumption is estimated to be 0.7kW[3]. The power consumption of a resistively heated cold walled furnace, in our work, is 0.3kW for the ramping to the growth temperature and assumed to scale linearly as a function of temperature to 0.3kW at 1200°C. To estimate the energy usage for each growth procedure, I multiplied the power draw with the length of time heating that was required, and then multiplied by the average electricity cost in the UK[4].

Finally, I estimated the cost of the gases used for CVD graphene growth. This was done by collating the time and rate of gas flows for each article. The volume of gas used was estimated in cubic meters (m^3) and the cost was then estimated (Table 4.3). The cost per m^3 of each growth gas was estimated using information available from BOC and presented in Table 10.1.

Bibliography

[1] The cost for 2.5cm x 100cm of 99.999% pure 25 μm thick copper from Alfa Aesar - http://www.alfa.com/en/catalog/10950

[2] Specifications taken from MTI website for MTI 1200X - 5L split tube furnace - http://www.mtixtl.com - Dec 2013

[3] Specifications taken from AXITRON website for Black magic II - http://www.aixtron.com/en/products/technologies/ - Dec 2013

[4] Energy saving trust estimation of average electricity cost in the uk - http://www.energysavingtrust.org.uk/Energy-Saving-Trust/Our-calculations - Dec 2013

[5] Costs and Volumes taken from BOC LTD website- http://www.Boconline.co.uk - Dec 2013

Acknowledgements

In order of appearance, I would first like to thank my father and step mum who always inspired me to achieve all that I can. Secondly, my warmest thanks to Monica Craciun and Saverio Russo my supervisors. I have never met two people so committed to a scientific cause and to always have time for me and my crazy ideas, some of which even became published works.

I would like to thank my housemates Tom Haworth, Alex Pearce and Dave Hudson, who always enjoyed a few too many beers and a great night out. I reserve special thanks to Dave who also worked tirelessly in the lab fabricating and measuring samples with me. I would like to thank the older generation of PhD students, (Freddie Withers, Ivan Khrapach and Tim Khodkov), who taught me all of the techniques and tricks required to make the best of samples. I would also like to thank the new generation of PhD students and post docs, Matt, Gareth, Adolfo, Domi and Moshin, who shared a passion for learning like I have. I reserve a special thanks to Laureline Mahe who over the time of the PhD became one of my best friends.

I would like to thank the Paul Wilkins, Adam Woodgate, Dave Gregory, Matt Wears and Nick Cole. Without their hard work in the mechanical workshop and advice for maintenance of equipment all of my tasks would have taken significantly longer.

While writing the last part of this thesis Freddie Withers and his loverly other half

Tanya Cistova, put me up in their house rent free and were like a second family, for this I cannot thank them enough. Finally I would like to thank my new bosses Jon Whitehead and Jon Edgeworth for providing me with a fantastic opportunity to learn a whole different set of skills at moorfield.

List of Publications

Withers, F. Bointon, T. H. Dubois, M. Russo, S. Craciun, M. F. Nano-patterning of fluorinated graphene by electron beam irradiation. *Nano Lett.*, **11**, 9, 3912-3916 (2011).

Contribution: Sample fabrication and Atomic force microscopy.

Khrapach, I. Withers, F. Bointon, T. H., Polyushkin, D. K. Barnes, W. L. Russo, S. Craciun, M. F. Novel Highly Conductive and Transparent Graphene?Based Conductors. *Adv. Mater.*, **24**, 21, 2844-2849 (2012).

Contribution: Sample fabrication, Raman spectroscopy, Transmission measurements, Transport measurements.

Withers, F. Bointon, T. H. Craciun, M. F. Russo, S. All-graphene photodetectors. *ACS nano*, **7**, 6, 5052-5057 (2013).

Contribution: Sample fabrication, Raman spectroscopy.

Bointon, T. H. Khrapach, I. Yakimova, R. Shytov, A. V. Craciun, M. F. Russo, S. Approaching magnetic ordering in graphene materials by FeCl3 intercalation. *Nano Lett.*, **14**, 4, 1751-1755 (2014).

Contribution: Sample fabrication, Raman spectroscopy, Transport measurements.

Withers, F. Bointon, T. H. Hudson, D. C. Craciun, M. F. Russo, S. Electron transport of WS2 transistors in a hexagonal boron nitride dielectric environment. *Sci. Rep.*, **4**, 4967 (2014).

Contribution: Raman spectroscopy, Transport measurements.

Wehenkel, D. J. Bointon, T. H. Booth, T. Boggild, P. Craciun, M. F. Russo, S. Unforeseen high temperature and humidity stability of FeCl3 intercalated few layer graphene. *Sci. Rep.*, **5**, 7609 (2014).

Contribution: Sample fabrication, Raman spectroscopy, Transport measurements.

Neves, A. Bointon, T. H. Melo, L. Russo, S. Schrijver, I. Craciun, M. F. Alves, H. Transparent conductive graphene textile fibers. *Accepted: Sci. Rep*, 2015.

Contribution: Sample fabrication.

Bointon, T. H. Jones, G. Sanctis, A. Pearce, R. Craciun, M. F. Russo, S. Large-area functionalized CVD graphene for work function matched transparent electrodes. *Submitted*, (2015).

Contribution: Sample fabrication, Raman spectroscopy, Transport measurements.

Bointon, T. H. Russo, S. Craciun, M. F. Is Graphene a good Transparent Electrode for Photovoltaics and Display Applications? *Submitted*, (2015).

Contribution: Review paper text.

Bointon, T. H. Barnes, M. Russo, S. Craciun, M. F. High quality monolayer graphene synthesized by resistive heating cold wall chemical vapour deposition. *Adv. Mater.* **Early Access**, (2015) doi:10.1002/adma.201501600.

Contribution: Sample fabrication, Scanning electron microscopy, Atomica force microscopy, Raman spectroscopy, Transport measurements.